Quantified Analysis of a Production Diesel Injector Using

X-Ray Radiography and Engine Diagnostics

BY

ANITA I. RAMÍREZ
B.S., University of Illinois at Chicago, Chicago, 2004

THESIS

Submitted as partial fulfillment of the requirements
for the degree of Doctor of Philosophy in Mechanical Engineering
in the Graduate College of the
University of Illinois at Chicago, 2015

Chicago, Illinois

Defense Committee:

Suresh K. Aggarwal, Chair and Advisor
Rodica Baranescu, Mechanical & Industrial Engineering
Kenneth Brezinsky, Mechanical & Industrial Engineering
Stephen Ciatti, Argonne National Laboratory
Douglas Longman, Argonne National Laboratory
Christopher Powell, Argonne National Laboratory

This thesis is dedicated to my love – Leonel Enrique Corado, my parents – Luis & Rosalinda Ramírez, my nieces – Natalia & Lucia Salazar, and my siblings – Guadalupe Ramírez, Jaime Salazar, & Mia Sánchez, without whom it would have not been accomplished.

A mis hijos, a quienes todavía no he conocido, esto es para ustedes …

ACKNOWLEDGEMENTS

I would like to take this opportunity to acknowledge and thank several people who have supported me in one way or another throughout this journey. I would like to thank my advisor, Professor Suresh K. Aggarwal, for his patience, guidance, and commitment through my doctoral work. His discerning questions and discussions have led me to a further appreciation and understanding of diesel engines.

Most of my time in graduate school has been spent at Argonne National Laboratory. During this time I was fortunate to interact with many excellent engine researchers. My sincerest gratitude is extended to Mr. Douglas Longman who encouraged and mentored me since the beginning of this project in my undergraduate years. His assistance and leadership along with his eternal optimism have made this work a possibility. His experience in engine research has proven to be a great boon to this research.

Dr. Stephen Ciatti has taught me a great deal regarding diesel engines, in-cylinder endoscopy, and research in general. Throughout the years we have engaged in several insightful discussions that have helped me to improve my work for which I am grateful. His aid in the engine optics was instrumental in the completion of this study. I would like to thank Dr. Christopher Powell who has aided me in the understanding of fuel spray through the work at Argonne's Advanced Photon Source (APS). His clear communication and continued assistance has been of great benefit to me in my efforts.

I am grateful to Dr. Kenneth Brezinsky and Dr. Rodica Baranescu for serving on my thesis committee and providing suggestions to improve my thesis. In addition, I have enjoyed being a student in their courses during my graduate studies which have helped to enrich my experience.

Throughout graduate school, one's lab-mates help in making the experience pleasant and memorable. I have had the fortune of working with many students at UIC who have improved my experience. Most notable of the blessings that have been brought to me throughout this journey has been

the camaraderie I have shared with Dr. Sibendu Som. He has shared struggles with me, pulled me out of difficult times, and played a significant role in my doctoral studies.

During the many hours in the lab, setting up experiments, troubleshooting problems, and analyzing data, Mr. Timothy Rutter has been a great source of support. His many hours of effort in making the engine experiments a possibility and additionally being an idea springboard made him an indispensable resource in this work. I would like to thank Dr. Essam El-Hannouny, Dr. Alan Kastengren, and Mr. Patrick McPartlin for many thoughtful discussions and for their effort in the x-ray portion of this research.

I would like to thank Mr. Gerald Smith and the staff of MERRP at UIC for their support throughout my graduate studies. I extend my gratitude to the Illinois Board of Higher Education who supported my graduate work through the Diversifying Higher Education Faculty in Illinois (DFI) fellowship.

My heartfelt thanks are given to my many students whom I have had the privilege of teaching throughout the years in PREP-M.E., Kaplan, S.I., E.S.P., U.B., and at R.J.D. They have provided a source of encouragement more powerful than they realize.

All of this work would not be possible without the support and belief of my family and friends. I would like to take this opportunity to thank them for all of their encouragement.

Quiero darle las gracias a mi familia, que han sido y siempre serán mis porristas inagotables en todas mis aventuras. ¡Lo hicimos! Extiendo las gracias a … Quique*: por ser mi fortaleza – él que me llena, me apoya, me ama, y me anima cuando me siento derrotada, y por ser los brazos abiertos después de un largo día de trabajo. ¡Ya hice el chabadi! ¡Qué cantankerous!* Mamasa y Papasa*: por siempre apoyarme y mantener ciegamente la fe en mí, por la vida de sacrificios que hicieron para que nosotras pudiéramos*

ACKNOWLEDGEMENTS (continued)

sobresalir. ¡Ya hay dos en la pared! Pita*: por enseñarme con gracia la definición de la perseverancia humana en la cara de dificultad.* Jaime*: por tu ejemplo y por la inspiración de nunca darme por vencida y siempre luchar con cada fibra de mi ser. I get up again! ¡Te extraño, Cuñinja!* Tali*: por enseñarme el amor incondicional a primera vista, y por volver a despertar a mi cerebrito interno.* Chuchi*: por mostrarme que no hay límite en el amor, y que vale la pena siempre buscar la felicidad.* Mia Mia*: por enseñarme a mantener una sonrisa a través de la lucha … todo lo que necesita es un poco de fe y confianza (y un poco de polvo de hada) ¡Wiiisiii Waaa, Baby!* Mis abuelitos (Manuel y Josefina Ramírez, Trinidad y Matilde Reyna)*: por darme la oportunidad de atreverme a soñar.* Mis primos (Tina, Yaya, y Manny)*: por ser mis camaradas en la vida y por ayudar a la calladita niña cerebrito a crecer a una calladita vieja cerebrito.* Mis tíos (Titi Chan, Tío Danny, Titi Ofin, Tío Meño, y Titi Tere)*: por consentirme, protegerme, y hacerme sentir amada.* Mis cuñadas (Vanesa y Melissa)*: por quererme, alegrarme, y proveer distracción cuando sea necesario. ¡I like daaat!* Mis suegros (El Sr. y La Sra.)*: por incluirme en su familia y creer en mis sueños.* Joel y Wendy*: por hacerme compañía desde lejos y por su apoyo invaluable durante esta jornada.*

¡Los amo hasta el cielo!

AIR

CONTRIBUTION OF AUTHORS

In the following thesis, portions of several publications are referenced where relevant. Below is a description of the contribution of the authors and the context in which content from each publication was used in the thesis. For brevity, the contribution of the authors for each publication is outlined initially, followed by a chapter-by-chapter description of the usage of the publications referred to by the number provided.

1. Ramírez, A.I., Som, S., Aggarwal, S.K., Kastengren, A.L., El-Hannouny, E.M., Longman, D.E., Powell, C.F.: Quantitative X-Ray Measurements of High-Pressure Fuel Sprays from a Production Heavy Duty Diesel Injector. Experiments in Fluids, 47(1):119-134, 2009.

   In this work, I performed the experiments alongside Dr. Sibendu Som, Dr. Alan Kastengren, Dr. Essam El-Hannouny, Mr. Douglas Longman, and Dr. Christopher Powell who were also a great assistance in data interpretation. I processed the data with the assistance of Dr. Alan Kastengren. Mr. Douglas Longman was the primary investigator for this research. Dr. Sibendu Som assisted in the acquisition of experimental data and performed all of the numerical simulation presented. Dr. Alan Kastengren and Dr. Christopher Powell were instrumental in the setup and execution of the x-ray radiography experimentation and developed the code used for data analysis. Dr. Essam El-Hannouny contributed greatly to the setup of injection system and all of its components. My graduate advisor, Dr. Suresh Aggarwal, contributed in the writing of the manuscript, analysis and interpretation of the data, and synthesis of the project.

CONTRIBUTION OF AUTHORS (continued)

2. Ramírez, A.I., Som, S., LaRocco, L.A., Rutter, T.P., and Longman, D.E.: Investigating the use of Heavy Alcohols as a Fuel Blending Agent for Compression Ignition Engine Applications. ASME 2012 Internal Combustion Engine Division Spring Technical Conference, Paper Number ICES2012-81169, 2012.

   This work represents a cursory "proof-of-concept" type study where an alternative fuel is blended with diesel in engine application. I performed the experiments alongside Ms. Lisa LaRocco and Mr. Timothy Rutter. Mr. Douglas Longman was the primary investigator for this research. Dr. Sibendu Som performed all numerical simulations presented and coordinated the chemical and physical property analysis of the fuels used. In addition, Dr. Sibendu Som presented this paper in my stead at the ASME conference in Torino, Italy. Ms. Lisa LaRocco was a great assistance in the design of the specialized fuel delivery system and performance of engine experiments. Mr. Timothy Rutter was an integral part of this study in experimental setup and execution of engine experiments as he held the "driver seat" while measurements were performed. I processed the performance, emissions, indicating, and image data acquired. All were a great assistance in interpretation of data.

3. Ramírez, A.I., Aggarwal, S.K., Som, S., Rutter, T.P., Longman, D.E.: Effects of Blending a Heavy Alcohol ($C_{20}H_{40}O$) with Diesel in a Heavy-Duty Compression-Ignition Engine. Fuel, 136:89-102, 2014.

   This work was an extension of the previous work outlined in reference (2) above. Contributions of the different authors are the same as discussed. Ms. Lisa LaRocco was

no longer on the project, therefore she was not involved in this publication. This work focused on a deeper analysis of the acquired data which helped to identify some behaviors that were not apparent when the initial study was performed. My graduate advisor, Dr. Suresh Aggarwal, contributed in the writing of the manuscript, analysis and interpretation of the data, and synthesis of the project.

CHAPTER 1: This chapter introduces my thesis project and includes a brief literature review to outline the significance of the research in a broader context. Portions of the publications listed above as (1), (2), and (3) are included.

CHAPTER 2: This chapter describes the equipment used in this research in detail. Portions of the publications listed above as (1), (2), and (3) are included.

CHAPTER 3: This chapter discusses the theory behind the various measurement techniques and outlines how governing equations for the data analysis performed. Portions of the publication listed above as (1) are included in regards to the operation principle of the x-ray radiography technique.

CHAPTER 4: This chapter presents the fuel spray work completed using x-ray radiography. Portions of the publication listed above as (1) are included.

CHAPTER 5: This chapter presents unpublished work that was performed to investigate the effect of

rate of injection on engine performance and emissions.

CHAPTER 6: This chapter presents work performed with the heavy alcohol, phytol, when blended with diesel in a single-cylinder engine. Portions of the publications listed above as (2) and (3) are included.

CHAPTER 7: The conclusions of the separate studies are listed in this chapter. Suggestions for future work are made based on the knowledge acquired in the research process.

TABLE OF CONTENTS

CHAPTER		PAGE
1.	INTRODUCTION	1
	1.1 Background	1
	1.2 Synopsis	3
	1.2.1 Compression Ignition Engine	3
	1.2.2 Fuel Injection and Spray	5
	1.2.3 Combustion and Emissions	6
	1.3 Literature Survey	8
	1.3.1 Fuel Spray Studies	8
	1.3.2 Fuel Injection Strategies	12
	1.3.3 Bio-Fuels in Compression Ignition Engine	14
	1.4 Objectives	18
2	EXPERIMENTAL SETUP	20
	2.1 Hydraulically Actuated Electronically Controlled Unit Injector and Injection System	20
	2.2 X-Ray Radiography	23
	2.3 Rate of Injection Meter	27
	2.4 Caterpillar Single Cylinder Engine and Support Equipment	29
	2.4.1 Cylinder Head Modifications	30
	2.4.2 Dynamometer	31
	2.4.3 Intake Air System	32
	2.4.4 Exhaust Air System	34
	2.4.5 Fuel Mass Flow	35
	2.4.6 Air Mass Flow	36
	2.4.7 Emissions Measuring Equipment	36
	2.4.8 Test Cell Control and Data Acquisition (Digalog)	39
	2.4.9 Cylinder Pressure	40
	2.4.10 Engine Crankshaft Angle Measurement	40
	2.4.11 High Speed Data Acquisition for Combustion Analysis	40
	2.5 In-Cylinder Combustion Imaging	41
3	THEORY AND CALCULATIONS	43

TABLE OF CONTENTS (continued)

CHAPTER		PAGE
3.1	X-Ray Radiography	43
3.2	Rate of Injection	44
3.3	Engine Cylinder Pressure	46
3.3.1	Engine Cylinder Pressure Data Analysis	46
3.3.2	Initial Procedures for Engine Cylinder Pressure	50
3.4	Engine Performance	51
3.5	Engine Emissions	54
3.6	In-Cylinder Combustion Imaging – 2-Color Optical Pyrometry	55
4	RESULTS – X-RAY FUEL SPRAY STUDY	62
4.1	Rate of Injection	62
4.2	Liquid Penetration	65
4.3	Fuel Distribution	72
4.4	Spray Isolation	78
4.5	Cone Angle	81
4.6	Summary	83
5	RESULTS – RATE OF INJECTION STUDY	85
5.1	Experimental Test Matrix	85
5.2	Constant Fuel Command	86
5.2.1	Rate of Injection	86
5.2.2	Combustion Behavior	90
5.2.3	In-Cylinder Imaging	95
5.3	Constant Fuel Delivery and Combustion Phasing	98
5.3.1	Rate of Injection	99
5.3.2	Combustion Analysis	102
5.3.3	Engine Performance and Emissions	109
5.4	Summary	111
6	RESULTS – ALTERNATIVE FUEL STUDY	113
6.1	Fuel Property Assessment	113
6.2	Experimental Test Matrix	115

TABLE OF CONTENTS (continued)

CHAPTER PAGE

6.3 Results and Discussion 116
6.3.1 Properties of Fuel Blends 116
6.3.2 Experimental Investigation 117
6.4 Summary 134
7 CONCLUSIONS 136
7.1 Synopsis 136
7.2 Concluding remarks 137
7.2.1 X-Ray Study 137
7.2.2 Rate of Injection Study 138
7.2.3 Alternative Fuel Study 139
7.3 Future Work 140
CITED LITERATURE 143
APPENDIX 151
VITA 159

LIST OF TABLES

TABLE PAGE

I. Engine Specifications 30
II. Experimental test matrix 86
III. Peak pressure values and locations for three ERS rate profiles. 91
IV. Locations of apparent SOI, mass fraction injected and burned for all rate shapes at 21 MPa oil rail pressure, 100mm^3/inj commanded fuel quantity, -8° aTDC SOI. Numbers in italics and parenthesis are the differences between that point and the apparent SOI for that condition. 94
V. Peak pressure values and locations for three ERS rate profiles at -8°CA aTDC SOI (Case A) and constant CA50 (case B). 103
VI. Locations of apparent SOI, mass fraction injected and burned for all rate shapes at 21 MPa oil rail pressure, constant fuel quantity, and -8° CA aTDC SOI. Numbers in italics and parentheses are the differences between that point and the apparent SOI for that condition 107
VII. Locations of apparent SOI, mass fraction injected and burned for all rate shapes at 21 MPa oil rail pressure, constant fuel quantity, and constant CA50. Numbers in italics and parentheses are the differences between that point and the apparent SOI for that condition 107
VIII. Comparison of physical and chemical properties of phytol and diesel fuels 114
IX. Comparison of the physical and chemical properties of phytol, diesel, and three blends 114
X. Experimental test matrix 115
XI. Peak cylinder pressure values and locations for each of the blends at various start of injection timings. NOTE: for 0 degree SOI timing case, peak cylinder pressure corresponds to compression pressure and not to combustion pressure. *indicates peak cylinder pressure from combustion. . 121
XII. Mass burn fraction (MBF) crank angle locations (shown in °BTDC) for each of the blends at the various start of injection timings. 122
XIII. Ignition delay (shown in °CA) as computed from SOI command to time taken to reach a heat release rate of 40 J/°CA for each of the SOI timings and fuel blends. 125

LIST OF FIGURES

FIGURE PAGE

1. Diagram of diesel engine combustion 3
2. Conceptual schematic of conventional diesel combustion [15] 7
3. Illustration of boot injection rate shape compared with standard rate shape. 12
4. Chemical Structure of Phytol 16
5. Schematic of injector nozzle 20
6. HEUI Injection System 21
7. Sample screenshot of CADetWIN software 23
8. (left) Top view image of experimental setup at APS (right) Schematic of experimental setup. 24
9. Measurement grid showing the position of the X-ray beam in the line-of-sight coordinate system of the spray 26
10. Angled spray chamber, isolation shield, and hole of interest 27
11. Schematic of Rate of Injection Test Setup 28
12. Modified cylinder head 31
13. Engine dynamometer setup 32
14. Intake air system 33
15. Exhaust air system 34
16. Specialized fueling system 35
17. Location of Emissions Sample Probe 37
18. Pierburg gaseous emissions sampling bench and analyzers 38
19. (top) Location of endoscope access in head, (middle) visualization of location of endoscope entry into the combustion chamber, (bottom) sample endoscope image with labeled injector tip and piston crown indicated with dashed line 42
20. Schematic of ROI measurement 44
21. Rate of injection profiles for 17 and 21 MPa oil rail pressures, 30 bar ambient pressure, 100 mm^3 per stroke fuel delivery. The transition period of rapid increase to quasi-steady injection is marked. .. 63
22. (a) Rate of injection calculated from x-ray radiography measurements (linear fits shown) for 17 and 21 MPa oil rail pressure. (b) Hybrid ROI profile of a single orifice used for input in numerical simulation. 64
23. STAR-CD model validation against x-ray radiography data. Spray penetration for 100 mm^3/injection fuel delivery, 30 bar ambient pressure, oil rail pressures of 17 and 21 MPa versus time. 65
24. Spray projected density versus axial position for 100 mm^3/injection fuel delivery, 30 bar ambient pressure, at 17 and 21 MPa oil rail pressures at 0.122 ms after SOI. 67
25. Comparison of x-ray data at 17 MPa oil rail pressure with penetration correlations by Payri [26] and Naber & Siebers [89] 69
26. Transverse mass distribution profile at axial position = 0.283 mm and 0.1 ms after SOI for the 21 MPa oil rail pressure case 72
27. (a) Transverse mass distributions at 0.15 ms after SOI for 17 and 21 MPa oil rail pressures plotted at axial positions of 0.183 mm, 2.083 mm, and 7.083 mm from the nozzle (b) Full field spray projected density contours at 0.15 ms after SOI for oil rail pressures of 17 and 21 MPa 73
28. (a) Transverse mass distribution as at 0.99 ms after SOI for 17 and 21 MPa oil rail pressures plotted at axial positions of 0.283 mm, 2.083 mm, and 7.083 mm from the nozzle (b) Full field spray projected density contours position at 0.99 ms after SOI for oil rail pressures of 17 and 21 MPa 74
29. (a) Transverse Integrated Mass (TIM) versus axial position at 0.15 and 0.99 ms after SOI for 17 and

LIST OF FIGURES (continued)

FIGURE PAGE

21 MPa oil rail pressures. (b) Trend in mass-averaged axial velocity versus axial position at 0.99 ms ASOI for 17 MPa oil rail pressure. 76

30. (a) Full field mass projected density at 0.7 ms after SOI for oil rail pressures of 17 and 21 MPa (b) Projected mass density contours in the near nozzle region at 1.15 ms after SOI for the 21 MPa rail pressure case (c) Transverse mass distribution at axial position of 0.283 mm from the nozzle at three different times after SOI for the 21 MPa rail pressure case. 79
31. Optical image of injection event for oil rail pressure of 17 MPa, chamber pressure of 2 bar and fuel delivery of 100 mm^3/stroke 80
32. Measured cone angle versus time for 17 and 21 MPa oil rail pressures (b) Zoomed cone angle versus time during the initial transition period. 82
33. Injector current signals and their corresponding fuel rate of injection profiles for (a) 100%, (b) 50%, and (c) 0% ERS 87
34. Reference image for aligning fuel injection rate profiles to engine experiments 88
35. (a) Injection rate profiles and (b) Fuel delivery quantities for 100%, 50%, and 0% ERS for 21 MPa oil rail pressure, 100mm^3/inj command, and -8° SOI. 89
36. Cylinder pressure for the three ERS rate profiles at 21 MPa oil rail pressure, 100 mm^3/injection commanded fuel quantity, -8° aTDC SOI. 90
37. Heat release rate and rate of injection profiles for the three ERS conditions at 21 MPa oil rail pressure, 100 mm^3/injection commanded fuel quantity, -8° aTDC SOI. 92
38. Locations of 5%, 10%, 50%, and 90% mass injected and mass fraction burned for all rate shapes at 21 MPa oil rail pressure, 100mm^3/inj commanded fuel quantity, -8° aTDC SOI. 94
39 . Images (top), temperature contours (middle), and soot volume fraction contours (bottom) for 100%, 50%, and 0% ERS. Temperature scales is on the left in Kelvin. Soot Volume fraction scale is on the right. Images are shown at (a) 2.5°, (b) 15°, and (c) 30°, and (d) 50° after TDC. 97
40. (a) Soot radiation temperature at the early stages of injection (b) Integral soot volume fraction towards the end of combustion. 98
41. Sample interpolated injection rate profile. 99
42. Fuel injection rate profiles for 21 MPa oil rail pressure, constant fuel delivery, at 100%, 50%, and 0% ERS (a) at -8°CA aTDC SOI and (b) constant CA50 (varied SOI). (c) Fuel delivery for all cases of rate shaping (error bars represent 1 standard deviation) 101
43. Cylinder pressure for the case of 21 MPa oil rail pressure, constant fuel delivery, and three rate profiles at (a) -8° CA aTDC SOI and (b) constant CA50. 102
44. Heat release rate and rate of injection profiles for the three ERS conditions at 21 MPa oil rail pressure, constant fuel delivery, and three rate profiles at (a) -8° CA aTDC SOI and (b) constant CA50. 104
45. Mass fraction burned and Mass fraction injected for the three ERS conditions at 21 MPa oil rail pressure, constant fuel delivery, and three rate profiles at (a) -8° CA aTDC SOI and (b) constant CA50. 105
46. Locations of 5%, 10%, 50%, and 90% mass fraction burned and mass fraction injected burned for all rate shapes at 21 MPa oil rail pressure, constant fuel quantity at (a) -8° CA aTDC SOI and (b) constant CA50. 106
47. Mean gas temperature for all rate shapes at 21 MPa oil rail pressure, constant fuel quantity at (a) -8° CA aTDC SOI and (b) constant CA50 108

LIST OF FIGURES (continued)

FIGURE PAGE

48. Brake Mean Effective Pressure for all rate shapes at 21 MPa oil rail pressure, constant fuel quantity at (a) -8° CA aTDC SOI and (b) constant CA50. 109
49. Brake specific fuel consumption for all rate shapes at 21 MPa oil rail pressure, constant fuel quantity at (a) -8° CA aTDC SOI and (b) constant CA50. 110
50. Relationship between CO and NO_x emissions for all rate shapes at 21 MPa oil rail pressure, constant fuel quantity at (a) -8° CA aTDC SOI and (b) constant CA50..... 110
51. Distillation curves for Diesel and Phytol..... 117
52. Actual amount of fuel injected per stroke when maintaining a constant injection quantity command. (Symbols represent the mean, error bars represent plus/minus one standard deviation, and the shaded regions show the range of maximum and minimum values. The dashed blue line represents the overall average with plus/minus one standard deviation indicated.) 118
53. Cylinder pressure plot of diesel and phytol blends for a case with the injection timing at (a) 8° (b) 4°, and (c) 0° BTDC. (Zoomed image of each on right, SOI command indicated with pink line, ROI profile shown in dashed line) 120
54. Heat Release Rate plot of diesel and phytol blends for a case with the injection timing at (a) 8°, (b) 4°, and (c) 0° BTDC. (Zoomed image of each on right, SOI command indicated with pink line, ROI profile shown in dashed line) 123
55. Cylinder temperature plot of diesel and phytol blends for a case with the injection timing at (a) 8°, (b) 4°, and (c) 0° BTDC. (Zoomed image of each on right, SOI command indicated with pink line, ROI profile shown in dashed line) 124
56. Peak cylinder pressure and brake mean effective pressure for diesel and phytol blends with respect to start of injection timing..... 126
57. Brake Specific Fuel Consumption of Diesel and the Phytol/Diesel blends at various SOI timings .. 128
58. Brake Thermal Efficiency of Diesel and the Phytol/Diesel blends at various SOI timings..... 129
59. (left) Combustion imaging and (right) temperature distribution of the 8° BTDC injection timing case for diesel and phytol blends shown at 4° ATDC; piston crown is indicated by dashed white line. . 131
60. Average soot radiation temperature for diesel and phytol blends for the 8° BTDC SOI condition. 132
61. NO_x and CO as a function of injection timing 133

LIST OF ABBREVIATIONS

ANL	Argonne National Laboratory
APD	Advanced Photodiode
APS	Advanced Photon Source
ATDC	After Top Dead Center
BMEP	Brake Mean Effective Pressure
BTE	Brake Thermal Efficiency
BSFC	Brake Specific Fuel Consumption
BTDC	Before Top Dead Center
CA	Crank Angle
CA50	Crank Angle location of 50% mass fraction burned
CAB	Cascade Atomization and droplet Breakup
CAT	Caterpillar
CFD	Computational Fluid Dynamics
CFR	Code of Federal Regulations
COV	Coefficient of Variation
CI	Compression Ignition
DPF	Diesel Particulate Filter
ECU	Electronic Control Unit
EGR	Exhaust Gas Recirculation
EOI	End of Injection
ERS	Electronic Rate Shaping (Shape)
EVO	Exhaust Valve Open
FID	Flame Ionization Detector
FWHM	Full Width Half Maximum

HCCI	Homogeneous Charge Compression Ignition
HEUI	Hydraulically Actuated Electronically Controlled Unit Injector
HVO	Hydro-treated Vegetable Oil
IR	Infrared
IVC	Intake Valve Closed
KH-ACT	Kelvin Helmholtz – Aerodynamic Cavitation Turbulence
MBF	Mass Burn Fraction
NO_x	Nitrogen Oxides
P5	5% Phytol / 95% Diesel fuel blend by volume
P10	10% Phytol / 90% Diesel fuel blend by volume
P20	20% Phytol / 80% Diesel fuel blend by volume
PCYLMAX	Peak Cylinder Pressure
PID	Proportional-Integral-Derivative
PM	Particulate Matter
PPM	Parts Per Million
ROI	Rate of Injection
SAE	Society of Automotive Engineers
SCR	Selective Catalytic Reduction
SOI	Start of Injection
TDC	Top Dead Center
TIM	Transverse Integrated Mass
VCO	Valve-Covered Orifice

SUMMARY

The work presented in this thesis pursues further the understanding of fuel spray, combustion, performance, and emissions in an internal combustion engine. Various experimental techniques including x-ray radiography, injection rate measurement, and in-cylinder endoscopy are employed in this work to characterize the effects of various upstream conditions such as injection rate profile and fuel physical properties.

Non-evaporating sprays are studied under engine-like ambient densities at the Advanced Photon Source (APS) of Argonne National Laboratory (ANL). The x-ray radiography technique is used to obtain detailed information regarding the fuel mass distribution in the spray with high temporal and spatial resolution. A single spray plume from a 6-hole full-production Hydraulically Actuated Electronically Controlled Unit Injector (HEUI) nozzle is isolated using a specialized shield. Two different injection pressures were investigated and parameters such as spray penetration, cone angle, and spray velocity were obtained. Differences are found between the initial rate of injection as calculated from x-ray data and that measured from a Bosch-type rate meter. The data acquired with x-ray radiography is used for the development and validation of improved Computational Fluid Dynamic (CFD) models.

Rate of injection is further studied using the same HEUI from the x-ray studies in a single cylinder Caterpillar test engine. The injection rate profile is altered to have three levels of initial injection pressure rise (100% ERS – fastest rise rate, 50% ERS – medium rise rate, 0% ERS – slowest rise rate). This concept seeks to decrease the amount of fuel initially injected into the cylinder, thus decreasing the pre-mix burn phase, lowering temperature, and thus decreasing NO_x emissions. Combustion behavior, engine performance, and emissions information was acquired for the three rate profile variations discussed above. For a constant delivery, the start of injection (SOI) timing is held constant and then adjusted to align the location of 50% mass fraction burned (CA50) for each rate shape. It is found that the NO_x emission

reduction is achieved when the SOI timing is constant at the penalty of lower power generated in the cycle. However, if CA50 is aligned amongst the three profiles, the NO_x emissions and power are constant with a slight penalty in CO emissions.

Finally, the influence of physical parameters of the fuel is examined in a study of the heavy alcohol, phytol ($C_{20}H_{40}O$), in internal combustion engine application. The physical and chemical properties of phytol and diesel are similar, excepting the lower vapor pressure and higher viscosity of phytol compared to diesel. Phytol is blended with diesel in 5% (P5), 10% (P10), and 20% (P20) by volume in order to achieve greater agreement in these values. Given the same injection commands to the engine's Electronic Control Unit (ECU), small differences are present in the total amount of fuel injected which may be caused by differences in physical properties of the fuel. Combustion behavior is similar between pure diesel and the phytol/diesel blends with small differences noted in peak cylinder pressure, ignition delay, and heat release rate in the premix burn phase. Diesel/phytol blends yield marginally lower power values due to the lower amount of energy in the phytol. In-cylinder soot radiation images show combustion instability at the start of the event for the 20% phytol/diesel blend. Overall, NO_x emissions are comparable across the different fuels used and no discernible trend is found in CO emissions.

1. INTRODUCTION

Parts of this chapter have been previously published as:

Ramírez, A.I., Som, S., Aggarwal, S.K., Kastengren, A.L., El-Hannouny, E.M., Longman, D.E., Powell, C.F.: Quantitative X-Ray Measurements of High-Pressure Fuel Sprays from a Production Heavy Duty Diesel Injector. *Experiments in Fluids*, 47(1):119-134, 2009.

Ramírez, A.I., Som, S., LaRocco, L.A., Rutter, T.P., and Longman, D.E.: Investigating the use of Heavy Alcohols as a Fuel Blending Agent for Compression Ignition Engine Applications. *ASME 2012 Internal Combustion Engine Division Spring Technical Conference*, Paper Number ICES2012-81169, 2012.

Ramírez, A.I., Aggarwal, S.K., Som, S., Rutter, T.P., Longman, D.E.: Effects of Blending a Heavy Alcohol ($C_{20}H_{40}O$) with Diesel in a Heavy-Duty Compression-Ignition Engine. *Fuel*, 136:89-102, 2014.

1.1 Background

Diesel engines continue to be the favored power source in heavy-duty use, primarily in truck engines, marine application, as well as a leader in the automotive sector in Europe, because of their high efficiency and power density. In spite of many advances in diesel technology, an ongoing quest for cleaner-burning, more efficient diesel engines continues. In addition, there is a desire for decreasing dependence on fossil fuels through the use of alternate sources such as biofuels. Because of their vast global use, further improvements in the capabilities of diesel engines would have significant impact.

Inherently, diesel engines produce high NO_x and soot emissions which must be reduced to meet clean air regulations. Many aftertreatment techniques such as particulate filters for soot, and catalysts for NO_x, are used to alleviate some of the high emissions problems [1]. Carcinogenic effects and other detrimental health consequences of inhaling diesel emissions motivate even further reduction in NO_x and soot. While aftertreatment methods are effective to meet current standards, reduction in raw emissions from the engine are necessary to further decrease the amount of harmful toxins released to the air. NO_x generation

and particulate formation in diesel engines are influenced by fuel injection characteristics, such as fuel penetration, liquid atomization, and mixing of fuel and air [2,3].

Improved fuel-air mixing can produce more efficient combustion and lower particulate emissions. The mixing process is governed by injection characteristics and spray processes. Therefore enhancements to the fuel injection process would aid in decreasing the amount of unburned fuel and reduce the level of harmful emissions. The injection characteristics depend on factors such as the needle lift dynamics and inner nozzle flow behavior, while the spray processes are influenced by aerodynamics outside the nozzle. Considerable research has focused on the characterization of the influence of several injection parameters, including ambient and injection pressures, nozzle orifice shape, etc. on fuel spray development [2,3,4,5,6,7]. Different fuel injection strategies such as varied injection timings, multiple injection events per cycle, and alternate rate of injection profiles have also been used to alter emission characteristics [8,9,10]. Establishing correlations between near nozzle flow behavior and fuel spray, and diesel engine performance and emissions will augment the capability of designing more efficient diesel engines.

The present work explores the effects of several parameters on fuel spray, combustion, performance, and emissions. The initial portion of the study, investigates fuel spray from a full-production, six-hole fuel injector is investigated using the x-ray radiography technique established by Powell et al. [11] at Argonne National Laboratory (ANL). This fuel injector is then studied in a single-cylinder Caterpillar engine where performance and emissions data are collected. In-cylinder endoscopy is used to record images of the combustion which can be used for temperature and soot production analysis. Fuel injection rate is varied to observe the effects on combustion and emissions. Finally, a heavy alcohol, phytol ($C_{20}H_{40}O$), is used as a blending agent with the diesel. Detailed experimental data such as that acquired in the present work

not only leads to further understanding of the spray behavior from the injector, but also provides valuable knowledge to enhance computational modeling capabilities.

1.2 Synopsis

The following section of this chapter serves to provide some background on the various aspects of this study. Relevant topics include fundamental engine, injection, combustion, and emissions processes.

1.2.1 Compression Ignition Engine

The compression ignition (CI) engine was created in the 1890s by Rudolf Diesel in Europe. The diesel engine has been a leader in the production of power worldwide. Although diesel engines yield higher efficiency than their spark-ignited counterparts, they are notorious for their poor emissions signature. The high production of soot and nitrogen oxides (NO_x) by diesel engines has driven much research in the field with the goal of reducing these pollutant emissions [12]. Diesel combustion relies on the efficient mixing of fuel and air under the appropriate pressure and temperature conditions.

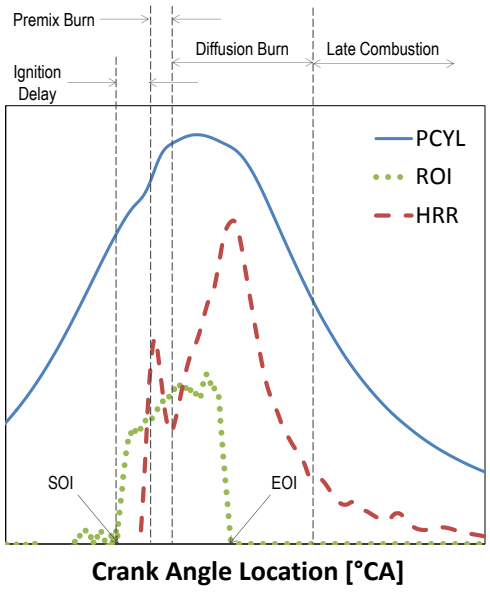

Figure 1. Diagram of diesel engine combustion

There are various stages of diesel combustion in the CI engine as can be seen in Figure 1. The fuel injector introduces liquid fuel into the combustion chamber which is filled with compressed fresh charge of air. The liquid fuel jet penetrates the combustion chamber where various parameters influence the atomization and vaporization of the resultant fuel spray. The first stage in the combustion process is the ignition delay, or the time between the start of fuel injection to the time of ignition. During this period, the fuel vaporizes and blends with the air in the cylinder. The duration of this delay is affected by many factors. For example, higher temperature and higher density of the surrounding gas will shorten the ignition delay. Meanwhile, lower amounts of oxygen in the charge will lengthen the ignition delay. This can be caused by adding diluents such as exhaust gas recirculation (EGR).

The piston is continually moving towards top dead center (TDC) which causes an increase of pressure and temperature. Once the cylinder conditions are appropriate, autoignition occurs. The fuel-air mixture developed in the ignition delay period will burn in the premix combustion phase. During this stage, heat release rates are high as the burning mixture joins fuel which is becoming burn-ready. The fuel becomes partially oxidized during the premix combustion.

After the fuel in the mixture generated in the ignition delay has completely burned in the premix phase, the diffusion or mixing-controlled burn phase begins. Pressure and temperature continue to rise through the start of this combustion phase. Injection is still taking place introducing new fuel droplets to the mixture of air and partially-burned products from the premix phase. These droplets are heated as they entrain ambient gas that is now at an elevated temperature from the premix burn. Throughout the diffusion burn, the high temperatures lead to rapid chemical kinetics and therefore combustion is governed by the rate at which the mixture of air and fuel grows suitable for burning.

The late combustion phase continues into the expansion stroke. The chemical kinetics slows down as the gas temperature decreases and the availability of oxygen becomes lower. Any unburned fuel along

with remaining energy in the combustion products are released. This process continues to slow down as the cylinder temperature drops [12].

1.2.2 Fuel Injection and Spray

Fuel enters the combustion chamber through a specialized injector that is appropriate for the application at hand. Understanding the fuel injection is important since proper atomization and spray of the fuel leads to more efficient burning and lower resultant emissions.

Inner Nozzle Flow

Inner nozzle flow is highly transient and has an impact on the resulting fuel spray. Turbulence and cavitation are generated during this stage. Cavitation is the generation of fuel vapor bubbles in the liquid flow caused when local pressure falls below the fuel's vapor pressure. Injection pressures and velocities are very high in the modern diesel engine causing shear stresses and high pressure gradients that create cavitation bubbles. Parameters such as nozzle geometry [mini-sac vs. valve-covered orifice (VCO), curvature, conicity, and length of the orifice, and number of holes], injector needle lift profile, imposed pressure gradient, and fuel properties (surface tension, viscosity, vapor pressure) can have effect on the inner nozzle flow.

Cavitation and turbulence generated at this stage can be both detrimental and beneficial to the injection process. In a positive way, they can lead to better break-up and atomization of the fuel during the initial part of spray yielding smaller droplets that burn more efficiently in the combustion process. On the contrary, cavitation bubbles can decrease the effective flow area of the fuel and cause additional wear on the injector nozzle.

Primary Spray Breakup

The movement of the injector needle controls fuel flow out of the nozzle. The fuel is at a high pressure and moves at a high speed out of the injector nozzle. Cavitation produced within the inner nozzle is advected into the fuel spray. This initial part of the fuel spray is called the primary breakup region and occupies a small length away from the nozzle exit. Continuous effort is given to characterize this part of the spray. It is believed that there are multiple phenomena affecting the breakup in this regime including aerodynamics between the liquid and gas phases, implosion of cavitation bubbles from the inner nozzle flow, and turbulence-induced breakup of the liquid jet [13].

Secondary Spray Breakup

The secondary spray breakup region refers to the further breakup of the droplets formed in the primary breakup regime to those with smaller diameter [14]. The spray entrains the surrounding gas and turbulence continues to affect the breakup. As inertial forces overcome surface tension forces, the aerodynamic forces cause the droplets to deform and eventually breakup into those of smaller diameter.

1.2.3 Combustion and Emissions

The fuel is injected into hot combustion chamber, where it entrains sufficient air for reaction. As has been discussed in the previous section, fuel vaporizes and mixes with air during the ignition delay before autoignition occurs and the premix burn phase begins. Fuel that has not had adequate time for mixing with the ambient air in the ignition delay along with new fuel being injected, burns as it is mixing in the diffusion burn phase. The conceptual model of direct-injected diesel combustion of Dec [15] is based on experimentally-acquired laser images and gives further insight into the process (shown in Figure 2).

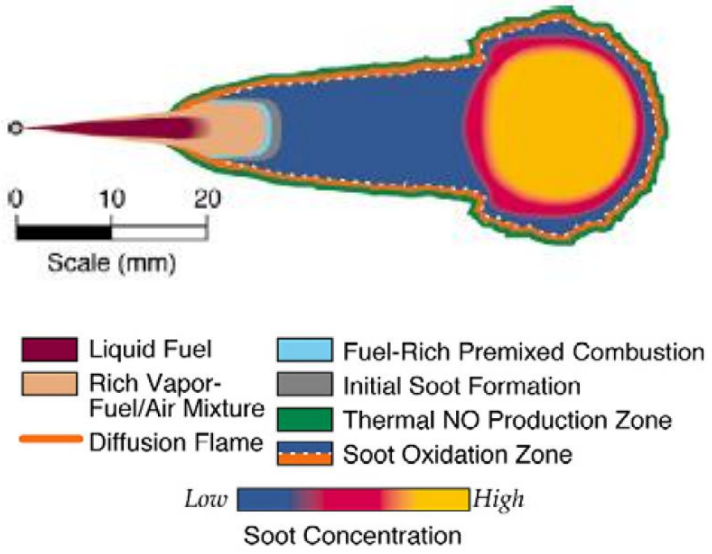

Figure2. Conceptual schematic of conventional diesel combustion [15]

Much of the combustion in a CI engine involves a lifted flame [12] as can be seen in the diagram where the combustion takes place some distance away from the nozzle exit. This distance along the axis of the fuel plume between the injector tip and where reaction first occurs is called the lift-off length. In this case, reaction indicates the presence of OH radical in an excited state [16].

During the premixed combustion phase, there is a lack of fresh air which results in a fuel-rich environment. The fuel begins to break down and form poly-aromatic hydrocarbons that are precursors of soot. Throughout the mixing-controlled (diffusion burn) stage of combustion, the fuel passes through the fuel-rich premixed combustion zone to the turbulent diffusion flame on the external rim of the plume. Fuel that is oxidized partially from rich premixed reaction produces partially burned products that lead to the formation of soot. Most of this soot is burned off during the late combustion phase and what remains

is emitted in the engine exhaust. While high temperatures at the peripheral diffusion flame lead to the reduction of particulates, they also lead to the generation of NO_x emissions.

Much effort has been put into the reduction of harmful emissions from the diesel engine. Exhaust Gas Recirculation (EGR) has been employed to reduce NO_x emissions. This technique uses a portion of the exhaust gas in the intake stroke to displace fresh air thus reducing the amount of available oxygen and lowering the effective air-fuel ratio. The addition of exhaust gas increases the specific heat of the intake mixture and consequently lowers flame temperature. This decrease in temperature brings about a reduction in NO_x emissions at the cost of increased PM emissions and harmful soot deposits on engine components, which can reduce the life of the engine. Diesel Particulate Filters (DPF) are effective in trapping and removing PM in exhaust, while Selective Catalytic Reduction (SCR) systems convert NO_x emissions to nitrogen and water.

1.3 Literature Survey

The literature review covers topics relevant to the present study. The information is divided into sections so that it can be more easily followed.

1.3.1 Fuel Spray Studies

Diesel sprays have been investigated through an extensive use of optical diagnostic techniques. Siebers [17] used Mie-scattered light imaging to perform extensive studies of diesel sprays with varied injection pressure, nozzle geometry and ambient conditions. It was observed that the liquid length of the spray is more sensitive to ambient conditions (gas density and temperature) rather than the nozzle geometry and injection pressure. Arcoumanis et al. [18] used laser techniques to investigate diesel sprays from multi-hole injectors, and observed spray tip penetration and velocity to be dependent on the frequency of injection. However, optical methods, while providing valuable information have intrinsic

limitations. Because of the high density of the droplets near the nozzle, most optical methods are ineffective in this region. The dense area close to the nozzle exit scatters visible light, making optical measurements ineffectual until further downstream in the spray. Consequently, for typical high-speed sprays resulting from a diesel fuel injector, it is difficult to obtain quantitative information with sufficient temporal and spatial resolutions, since high spray density near the nozzle prevents the acquisition of such data.

X-ray radiography has been used extensively for many applications including the study of fuel sprays. Fuel droplets in the spray cause much scatter in light which limits the capability of optical techniques, however, x-rays are absorbed by the fuel which make this technique appealing for investigating fuel sprays, particularly in the near-nozzle area where the density is high. Comprehensive spray characteristics such as the cone angle and spray penetration can be obtained by both optical and x-ray methods. However, x-ray radiography yields quantitative data with fine temporal and spatial resolution. In addition, this absorption of x-rays permits the measurement of the mass distribution of the fuel in the spray which is not attainable using optical methods.

The x-ray radiography technique has been used extensively to study single-hole research nozzles at pressure conditions lower than those of characteristic diesel engines [19,20,21,22]. Measurements at higher ambient pressures are challenging because of limitations in the design of the specialized narrow-slit windows and the high level of x-ray extinction that would result from the additional fill gas in the spray chamber [22,23].

Multi-hole nozzles are commonly used to improve the mixing in the engine cylinder. Spray from a multi-hole nozzle differs from that of a single-hole nozzle due to internal flow differences inside the nozzle. A study of large-scale and standard-sized nozzled by Soteriou et al. [24] showed that cavitation is asymmetric as it develops and propagates through the orifice. In addition, multi-hole nozzles will have

increased turbulence in comparison to single-hole nozzles. Chaves et al. [25] performed studies of fuel spray using a real-scale transparent nozzle using optical techniques. Payri et al. [26] used optical techniques to examine the global spray behavior in the first 15 mm of the spray from a non-isolated 6-hole common rail injector. The spray tip penetration in the transient region was observed to behave differently than in the steady state region. Application of x-ray radiography to multi-hole nozzles is quite challenging due to the difficulty of obtaining adequate spray isolation. It is desired that only a single plume of interest sprays freely in the direction normal to the x-ray beam without interference from neighboring spray plumes. This requires significant design considerations. Leick et al. [27] used a multi-hole, common rail, single fluid injection system where a single plume was isolated and investigated spray behavior using x-ray radiography under ambient density conditions corresponding to those in a typical automobile engine. They used a near production nozzle to investigate the spray from three orifices at two different gas densities, and observed that the ambient density has a relatively minor effect on the mass distribution. In addition, the mass distributions obtained in this study indicated the absence of a pure liquid core in the spray, suggesting rapid mixing of gas and liquid near the nozzle.

In the present work, non-evaporating spray from a multi-hole production diesel injector is studied at engine-like ambient density using the x-ray radiography technique. A single spray plume from the six-hole tip is isolated using a special shield that deflects the additional plumes so as not to interrupt the internal nozzle dynamics. The plume of interest is studied throughout the entire injection event from the initial transient stage where flow is highly affected by the needle dynamics through to the steady state fully developed spray. The injector used is a full-production nozzle that includes any geometry flaws, surface irregularities, etc. that are present in the injectors in practical engine application. Since the aforementioned manufacturing characteristics will have an effect on injector operation and resultant fuel spray, this study allows for analysis more representative fuel spray. In addition, the same nozzle that is

used in x-ray experiments is used in engine experiments where performance and emissions are also measured.

As mentioned earlier, the x-ray radiography possesses the unique capability of obtaining fuel mass measurements in the dense near-nozzle region. This comprehensive experimental data can be used for validation and improvement of existing spray models. Also in regards to modeling, non-evaporating sprays offer a more rigorous evaluation for liquid breakup and atomization models in the near nozzle region, since the uncertainties related to reacting flow models (such as evaporation, ignition, combustion etc.) can be isolated. Some recent studies have attempted to use x-ray data for spray model validation. Tanner et al. [28,29] employed a Cascade atomization and droplet breakup (CAB) model and compared the liquid penetration and transverse mass distribution with x-ray measurements. However the rate of injection (ROI) profile was not known for injection conditions and injection velocities were determined by an iterative process to match the spray penetration. In the present study, the ROI was determined from a Bosch rate meter coupled with x-ray measurements, thus reducing the uncertainty associated with injection velocities.

With a primary objective of improving emissions, the study of the diesel spray is performed with intentions of expanding knowledge regarding its performance in actual engine-like conditions. Although diesel sprays have been extensively studied, there is still much to be learned about fuel sprays, especially near the nozzle exit where optical techniques are not very effective. The use of a production diesel injector allows for engine testing using the same equipment as was used with x-ray radiography.

1.3.2 Fuel Injection Strategies

Varied fuel injection strategies have been used in efforts to improve emissions without compromising power and performance [30,31,32,33,34]. Some of these such strategies include altered start of injection timings, multiple injections, and varied rate of injection profile.

Injection rate shaping is a technique which aims to lower NO_x emissions with little penalty in soot production and brake specific fuel consumption (BSFC). In this approach, less fuel is injected in the initial stages of injection, forming what is called a "boot shape" profile. The initial rise of heat release can lead to high local temperatures and the production of NO_x [12]. Injection rate modulation is designed to decrease the availability of fuel in the ignition delay period and limit the initial heat release rate. The injection pressure rises later in the event and enhances mixing [35]. An exaggerated sample profile is presented in Figure 3 with the lower quantity of fuel injected at the start of the event.

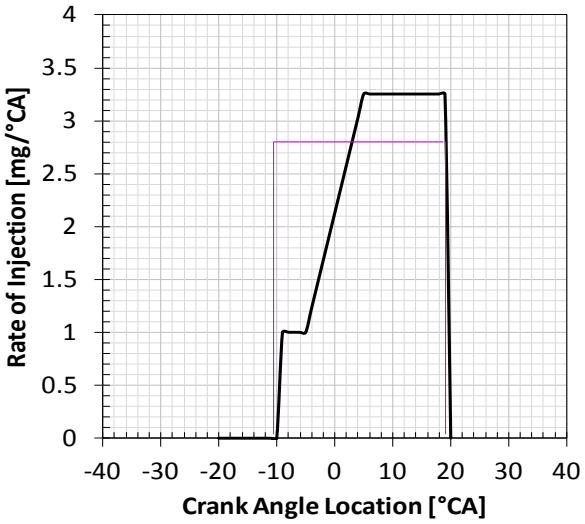

Figure 3. Illustration of boot injection rate shape compared with standard rate shape.

Fisher and Mueller performed a study with non-reacting sprays on liquid length comparing a common rail injection system with a HEUI in a single cylinder optical engine [36]. These two systems have different injection rate profiles, with the common rail having more of a top-hat shape, while the HEUI possesses a more gradual initial rise in fuel injection rate. Injection conditions were matched as closely as possible between the two injection systems. Engine speed was maintained constant while SOI timing, injection pressure, and duration were varied for the two different fuels. It was found that difference in injection pressure had little influence on in-cylinder liquid length for both the common rail and HEUI systems at their test conditions. In addition, the difference of rate shape between the two systems did not have a significant impact on the liquid length observed in the engine cylinder. While the ratio between the ROI of the two systems reached as high as 3, the ratio between the liquid lengths generated by the two systems at the varied conditions remained near unity (~1.2).

Desantes et al. performed an extensive study on the effects of rate variation on combustion and engine emissions [35,37]. In this work, a single-cylinder engine was used with a controlled unit pump injection system. The injection rate was controlled using a modified solenoid valve. Three different boot shape profiles, in addition to the standard baseline, were used at three speed-load conditions. They found that NO_x emissions were reduced with the boot profiles, especially as the boot injection pressure is decreased and boot duration is lengthened. The use of boot profiles lengthens the injection time, and thus, BSFC and soot emissions increase. However, in their studies of combustion, they found that their main objective of reducing the premix burn phase was not achieved when using the boot profiles. Conversely, effects on the diffusion burn were more evident. Longer boot duration yielded less efficient mixing, producing increased soot emissions. Greater injection pressure during boot portion improved mixing, giving quicker burning rates and increased NO_x emissions with decreased soot. They concluded that with their particular setup, boot injection profiles were most useful in high load condition where the NO_x reduction compensates for the increased soot.

Beck and Chen used an electronic unit injector to generate boot injection profile and observed 50% reduction in NO_x while increasing BSFC by 1% [38]. Herzog et al. made suggestions on specific conditions for the optimum characteristics of the boot profile [39]. At higher engine speeds Herzog recommends longer boot duration with a reduced main injection pressure. In conjunction with the conditional benefits of the boot profile, Ghaffarpour and Baranescu performed a numerical study showing that at low load and medium speed, boot injection is not beneficial [31].

1.3.3 Bio-Fuels in Compression Ignition Engine

With the ever-growing need to reduce dependence on fossil fuels, bio-derived fuels are of global interest. It is projected that the fossil fuel demand will triple during the 30 year span from 1990-2020 [40]. With the increased use of fossil fuel by the transportation sector, comes an increase in harmful pollutant byproducts. Alternative fuels are being pursued worldwide, but each must be evaluated on an individual basis, analyzing each fuel's advantages and disadvantages. According to Agarwal [40], there are four major factors affecting the usage of biodiesel. The first being any necessary changes in current hardware if the biofuel were used. If extensive modification is necessary to use a certain biofuel, it is not likely to be implemented. The second factor is an expansive infrastructure for processing of the fuel. The third factor involves the environmental impact of the alternative fuel. If it proves to be more polluting to the current fossil fuel, it is not an acceptable alternative. Lastly, cost to the end user impacts the feasibility of a fuel's implementation. Excessive cost to the consumer that is associated with the use, maintenance, equipment wear, and hardware life as a result of using the alternative fuel will impede the use of the alternative fuel.

Biofuels can be made from both edible and non-edible feedstock and differ in origin based on what is in demand in a specific locale. For example, fuels generated from wheat and sugar beet are popular in Europe [41], Karanja and Jatropha are popular in south Asian countries, while corn and soy based biofuel is popular in North America. Alternative fuels can help improve the well-being of energy usage in the

transportation sector by developing renewable fuel sources while concurrently reducing transportation-based emissions. A major challenge is to identify fuels that are compatible with the existing compression ignition engine infrastructure.

Second-generation biofuels play an integral role in the global objective of cultivating various sources of clean renewable energy. Using such biofuels for blending could extend the duration of petrodiesel use in CI applications. An integrated effort to develop second-generation biofuels while maintaining engine operation concepts would be timely. Such an approach could expedite the incorporation of second-generation biofuels as blending agents for CI engine applications.

Biodiesels from different feedstocks, such as edible and non-edible land plants, waste oils, animal fats and algae, have been extensively investigated as blending agents for CI operation [42,43,44,45,46,47]. The United States Department of Agriculture has identified cuphea-methyl ester as a feasible blending fuel because of the similarity between its physical properties to those of diesel [48,49]. Hydro-treated vegetable oil (HVO), possesses promising CI engine qualities and is compatible with the current diesel infrastructure which has attracted the consideration of countries in Europe [50,51]. Bio-derived alcohols, like butanol and ethanol, have been investigated in the past decade as blending agents for diesel fuel. Hansen et al. [52] performed research on ethanol-diesel blends and concluded that further studies are needed to ensure long-term engine durability when these fuel blends are used. Rakopoulos et al. [53,54] blended butanol and diesel at 8% and 16% by volume and analyzed the combustion performance of a multi-cylinder, direct-injected engine. They found a lengthened ignition delay and decrease in the maximum cylinder pressure and temperature. Iso-pentanol was also recently found to be suitable as a blending agent with gasoline for homogenous charge compression ignition (HCCI) engines [55]. The above literature search reveals that there has been a significant amount of research on incorporating first-generation biofuels in the CI engine infrastructure.

The primary motivation for the present research is to evaluate second-generation biofuels as blending agents for CI engines. Long-chain alcohols, because they have higher energy content than ethanol, butanol, and iso-pentanol, are particularly lucrative alternatives. In metabolic engineering efforts, Argonne researchers have designed strains that are produced by photosynthetic bacteria and eventually produce a heavy alcohol called phytol (C20H40O), shown in Figure 4.

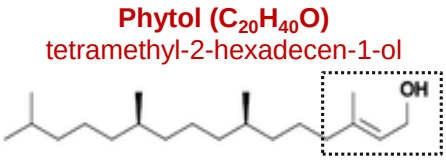

Figure 4. Chemical Structure of Phytol

However, the process is still at a laboratory scale and unable to generate quantities large enough for full-scale engine experiments. Therefore, the phytol fuel samples for this research were obtained from an outside source [56]. Because of its oxygen content, phytol is predicted to be have lower particulate matter (PM) emissions in comparison to diesel [42,57]. Phytol's physical and chemical properties (cetane number, heat of combustion, density, surface tension, etc.) correspond in magnitude to those of diesel fuel, suggesting that it might be a good blending agent. Its viscosity, however, is about 20 times higher and vapor pressure is significantly lower than that of diesel fuel, which further encourages studying blends of diesel and phytol, rather than testing pure phytol as a CI engine fuel.

The present study takes a multi-step approach to perform a preliminary assessment of the feasibility of using phytol as a blending agent with diesel fuel under CI engine conditions. Three different blends of phytol (5%, 10%, and 20% by volume) with diesel (i.e. P5, P10, and P20) were studied. The first step involved assessing the physical and chemical properties of the blends. In general, the heat of combustion, density, and cetane number of all five samples were close to each other. Differences in vapor pressure and viscosity were quite significant, however, note that the vapor pressures of the phytol blends were not measured, but rather were calculated using simple mixing rules. It can be seen that blending the phytol and diesel yielded viscosities closer to that of pure diesel. Since there are significant differences in the viscosities and vapor pressures of neat diesel, neat phytol, and phytol/diesel blends the injection characteristics can be expected to differ. For instance, Som et al. [58] observed that cavitation and turbulence behavior inside the injector differed notably in soy-based biodiesel compared to diesel fuels as a result of variations in physical characteristics of the fuel such as surface tension, viscosity, and vapor pressure. Boundary conditions at the exit of the injector orifice are determined by the injector flow qualities. Turbulence and cavitation levels, and rate of injection profile affect fuel atomization and spray and thus impact the engine performance. Som et al. [13] used an integrated model method employing the recently created Kelvin Helmholtz – Aerodynamic Cavitation Turbulence (KH-ACT) primary breakup model [59]. The impact of cavitation and turbulence [60] as an artifact of nozzle flow is regarded in the spray/combustion modeling using this approach. In comparison of the soy-based biodiesel and diesel studied, it was found that differences in nozzle-flow characteristics lead to variations in spray. Specifically, the lower cavitation and turbulence in the nozzle produced slower breakup for the biodiesel yielding higher spray penetration with a smaller cone angle.

Thus, the second part of this investigation was to perform robust in-nozzle flow simulations characterizing the cavitation, turbulence, and flow characteristics of phytol and comparing them to those of diesel fuel. This exercise helps clarify the influence of viscosity and vapor pressure differences on in-

nozzle flow development. However, comprehensive computational fluid dynamics (CFD) modeling of phytol/diesel blends for a CI engine simulation are not currently possible. The differences in the physical and chemical properties between phytol and diesel may necessitate the development of new spray and combustion models, including new kinetic mechanisms, before this can be done. Nevertheless, the nozzle flow simulations are useful to help characterize the effects of fuel's physical properties, especially due to the challenges associated with the experimental investigation of nozzle flow processes.

The final step of this work is to study the phytol/diesel blends in a single cylinder engine where performance and emissions information is collected. In-cylinder endoscopy was also used to visualize the combustion of the phytol/diesel blends. Since the viscosity differences between pure phytol and diesel were so large, running neat phytol in the engine was not attempted. Further details of this work are provided in the following sections. Engine and injection system durability tests were not possible because of the small amount of fuel available.

1.4 Objectives

In this work, various techniques are used to further the understanding of fuel injection and its effects on performance and combustion in an engine. This works seeks to develop the capability to study a six-hole production injector under high ambient pressures using x-ray radiography technique. Through investigation by x-ray the effects of several parameters such as nozzle geometry, injection system architecture, injection pressure, and number of orifices on the spray are studied. Near-nozzle spray information obtained in this work will supplement and fill gaps in the current data available. In addition, engine experimentation incorporating performance analysis, emissions measurements, and in-cylinder endoscopy will bolster the knowledge of injection effects. Variation of injection rate profile and usage of multiple fuels furthers the understanding of upstream conditions on fuel spray, performance, and emissions. This work seeks to improve understanding specifically in the following approaches:

Task 1: X-Ray Radiography

- Use monochromatic high intensity X-Ray source at APS to perform radiography experiments on production HEUI at test conditions that are similar to part-load engine conditions.
- Vary oil rail pressure to study the effect of injection pressure on the near nozzle spray behavior.
- Provide a high resolution data set for use in improvement of Computational Fluid Dynamic models.

Task 2: Perform a study of the variation of the rate of injection

- Use various rate injection profiles in the single cylinder engine to study effects of the boot profile on combustion and emissions.
- Make adjustments to start of injection timing to identify areas of large influence of injection rate profile.

Task 3: Study the use of alternate fuel in the engine

- Repeat engine conditions that were studied with diesel using blends of diesel and the alternative fuel, i.e., phytol.
- Use the information obtained in experiments to observe the effects of fuel properties such as viscosity and vapor pressure.

2 EXPERIMENTAL SETUP

Parts of this chapter have been previously published as:

Ramírez, A.I., Som, S., Aggarwal, S.K., Kastengren, A.L., El-Hannouny, E.M., Longman, D.E., Powell, C.F.: Quantitative X-Ray Measurements of High-Pressure Fuel Sprays from a Production Heavy Duty Diesel Injector. *Experiments in Fluids*, 47(1):119-134, 2009.

Ramírez, A.I., Som, S., LaRocco, L.A., Rutter, T.P., and Longman, D.E.: Investigating the use of Heavy Alcohols as a Fuel Blending Agent for Compression Ignition Engine Applications. *ASME 2012 Internal Combustion Engine Division Spring Technical Conference*, Paper Number ICES2012-81169, 2012.

Ramírez, A.I., Aggarwal, S.K., Som, S., Rutter, T.P., Longman, D.E.: Effects of Blending a Heavy Alcohol ($C_{20}H_{40}O$) with Diesel in a Heavy-Duty Compression-Ignition Engine. *Fuel*, 136:89-102, 2014.

The work performed in this study was performed on various test equipment. Explanations of each of the systems are included below.

2.1 Hydraulically Actuated Electronically Controlled Unit Injector and Injection System

All of the studies presented in this work were performed using a hydraulically actuated, electronically controlled unit injector (HEUI) model 315B mini-sac with six holes. The full-production, mini-sac nozzle investigated is shown schematically in Figure 5. It has six cylindrical holes with diameter of 169 μm at a 126° angle as shown.

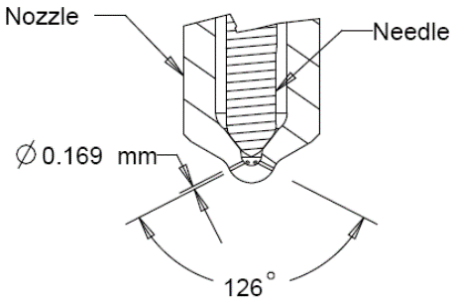

Figure 5. Schematic of injector nozzle

The main components of the HEUI injection system include: the high-pressure oil system, the fuel system, the injector control interface, and the HEUI injector itself. A schematic of the HEUI injection system is shown in Figure 6.

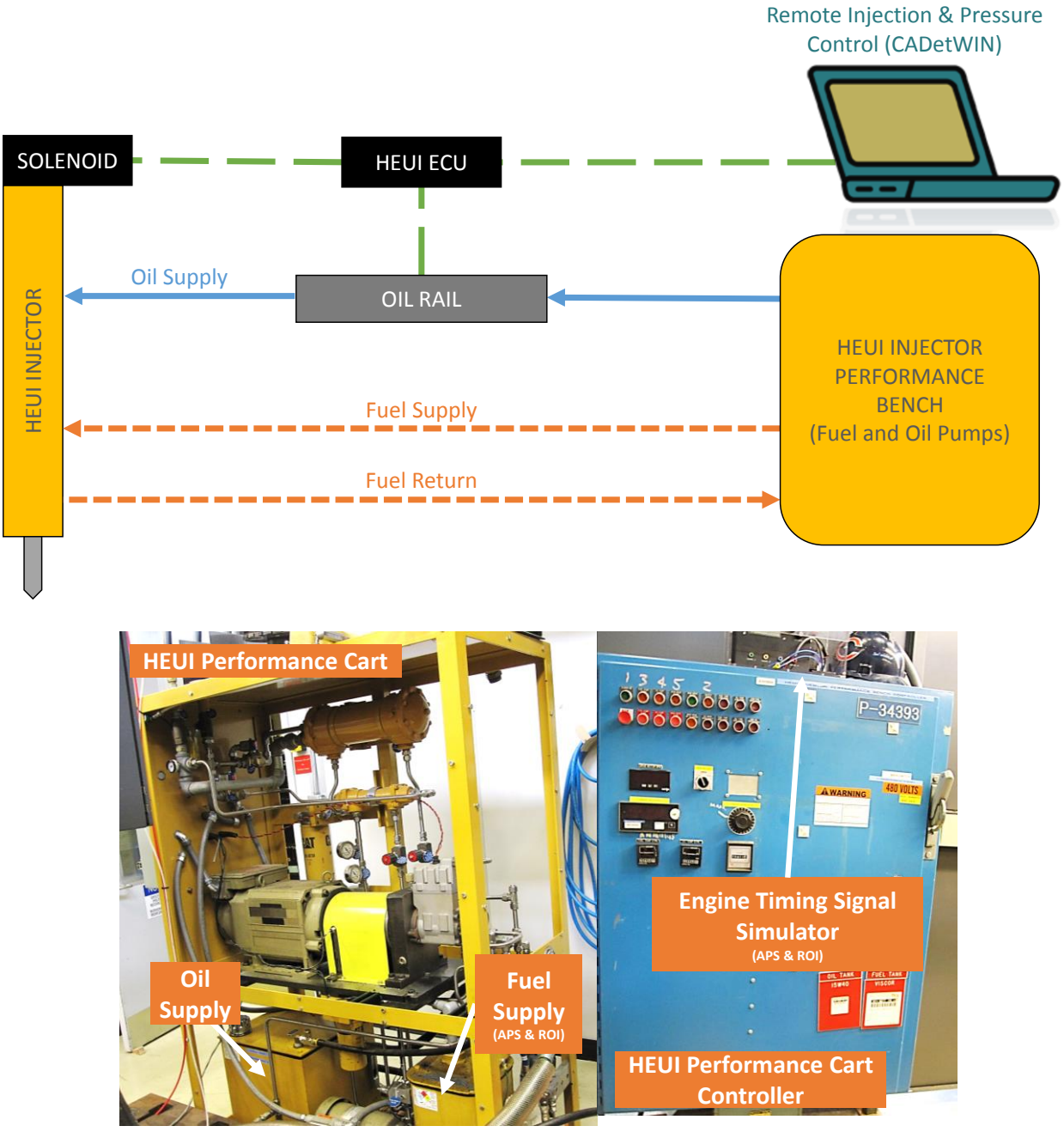

Figure 6. HEUI Injection System

The HEUI performance bench provides the injector with both fuel and oil and also collects the return fluids. The temperatures and pressures of the supply fuel and oil are monitored and controlled in the bench. High pressure oil is supplied from the bench to the oil rail via a Caterpillar variable delivery high-pressure oil pump. A pressure sensor and thermocouple are attached to the rail as a check of the oil conditions, along with an additional pressure sensor which communicates with the Electronic Control Unit (ECU). The oil is then supplied to the injector where it builds fuel pressure for injection. The oil is then vented through the top of the injector and is cycled back to the bench (not shown).

The HEUI applies hydraulic pressure from the oil to raise the fuel pressure to the set value for direct injection. This is done by an internal differential piston, which multiplies the relatively modest oil rail pressure to a high fuel injection pressure. This injector uses a pressure intensification ratio of approximately 6.6 between the oil rail pressure and injection pressure. When injection pressure is greater than the pressure needed to open the needle, the fuel injection starts. Parameters such as the injection timing, duration, and quantity are controlled by a solenoid that is connected to the engine's ECU [61]. A key feature of the HEUI injection system is the capability to modify the injection rate profile by altering the oil rail pressure. This feature is referred to Electronic Rate Shaping (ERS) and is discussed in other sections. CADetWIN software is used to control and monitor parameters such as oil rail pressure, engine speed, and injection quantity. A sample screenshot of the CADetWIN software is shown in Figure 7. Through this software the oil rail pressure (Channel 7), ERS profile (Channel 9), fuel injection quantity (Channel 16), and start of injection (SOI) timing (Channel 24) can be controlled. More detailed analysis of the HEUI injection system can be found in [62,63,64].

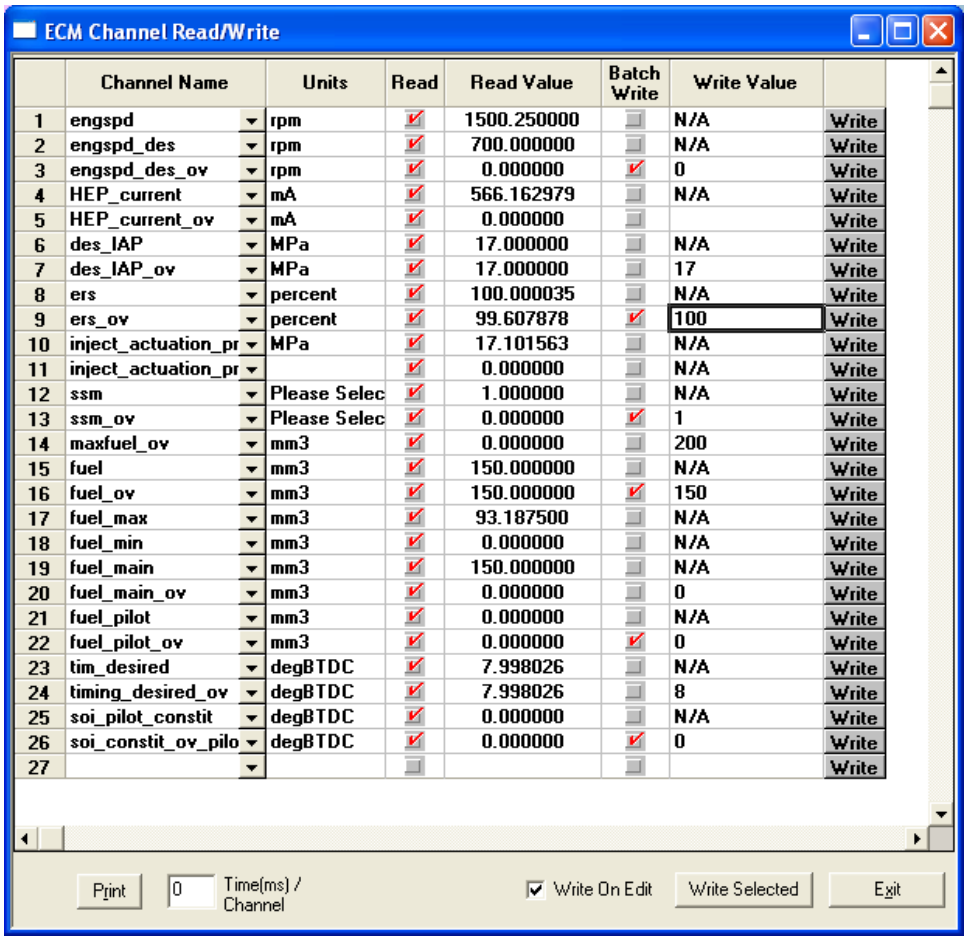

Figure 7. Sample screenshot of CADetWIN software

2.2 X-Ray Radiography

The X-ray measurements were performed at Argonne National Laboratory using the Advanced Photon Source (APS) facility, which generates a highly intense x-ray beam. The x-ray radiography technique is based on the linear absorption of the monochromatic x-ray beam passing through the spray. Because the x-ray is monochromatic, the Beer-Lambert Law can be used to relate the x-ray intensities measured before and during the spray event to the mass of fuel in the beam path.

A schematic and a top-view image of the experimental setup are shown in Figure 8. The x-ray energy of 8 keV with a narrow range (2% bandwidth) of x-ray wavelengths was selected using a monochromator. This energy provides a good compromise between absorption and penetrating power, allowing significant absorption due to the spray while maintaining sufficient intensity through the spray chamber. Vertical and horizontal x-ray slits were used to limit the beam size. Full width half maximum (FWHM) values of the beam size were 260 µm in the axial direction and 50 µm in the transverse direction.

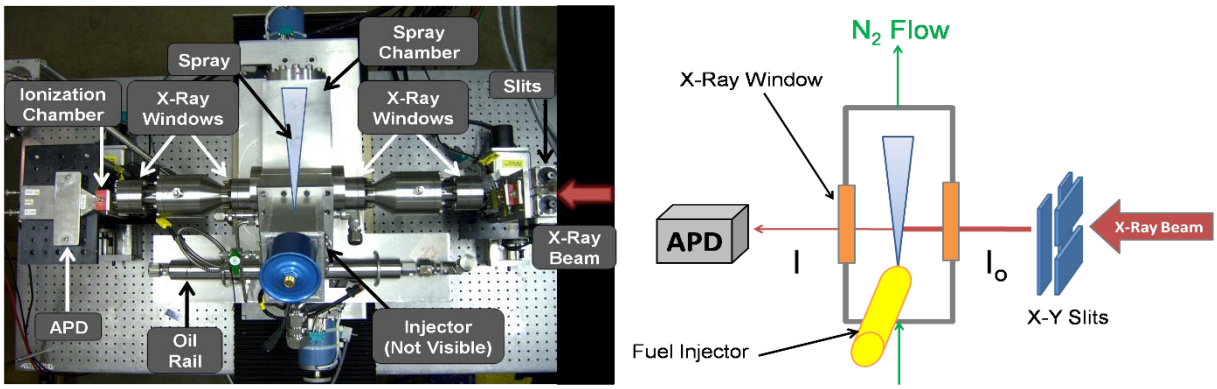

Figure 8. (left) Top view image of experimental setup at APS (right) Schematic of experimental setup.

An avalanche photodiode (APD) with a time response faster than 5 ns is used to monitor the x-ray intensity. The APD output, which is proportional to the x-ray intensity, was recorded using a fast digitizing oscilloscope every 1 ns for a duration of 4 ms, which encompasses the entire spray event. To increase the signal-to-noise ratio, the average x-ray intensity from 128 consecutive spray occurrences is

taken at each position white maintaining time-resolved characteristics. The three-dimensional fuel density is projected into two dimensions along the x-ray beam path. Thus, the x-ray intensity is converted to projected density with units of mass per unit area as is discussed in section 3.1, with a standard deviation around 1.1 $\mu g/mm^2$ (slightly increased in the higher density areas of the spray). In the vertical direction, the position of the nozzle is accurate within 3-5 microns and 10-20 microns in the horizontal direction. Other works provide a discussion of the setup and technique in greater detail [20,65,66].

The spray chamber was mounted on high precision translation stages that moved it in two dimensions in the plane perpendicular to the x-ray beam. For each measurement condition, measurements were made at approximately 980 different coordinates. Figure 9 shows the measurement grid used in these experiments. The spatial resolution of the measurement is a function of both the size of the X-ray beam and the spacing between successive measurement points. The size of the X-ray beam is 260 μm × 50 μm. The spacing between measurement points varies across the measurement domain. Closest to the nozzle, measurements were taken each 0.2 mm in the axial direction and 0.03 mm in the transverse direction eventually progressing to the 1 mm axial and 0.07 transverse separation further downstream. It should be noted that these measurements are composite data from many different spray events. Thus, the radiography data show the persistent, ensemble average features of the spray, rather than the details of any particular spray event.

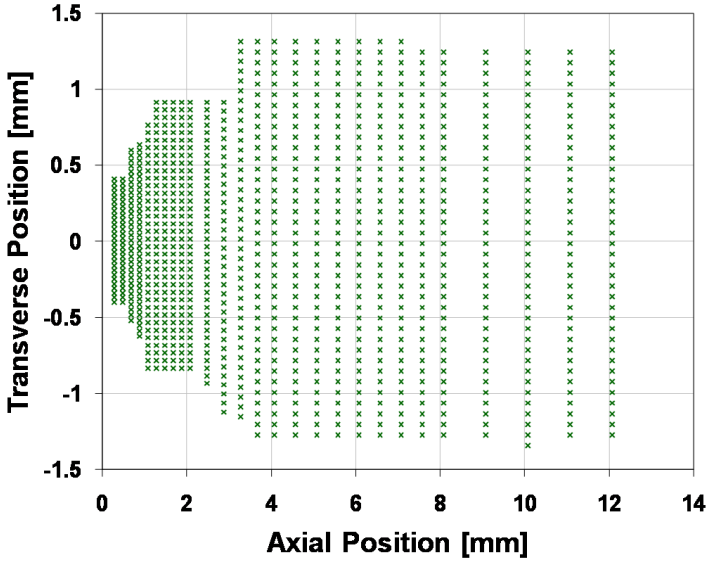

Figure 9. Measurement grid showing the position of the X-ray beam in the line-of-sight coordinate system of the spray

The x-ray radiography technique uses line-of-sight measurements normal to the spray. For this reason, the injector mounts at an angle, and a single plume of the six on the injector nozzle is isolated during x-ray work. This was done using an angled spray chamber and a specially-designed isolation shield shown in Figure 10. Angling the spray chamber ensures that the spray is normal to the x-ray beam. The intricately designed and manufactured shield allowed the plume of interest to spray freely through the spray chamber in the direction indicated, while deflecting the remaining plumes. The shield was designed in such a way that it does not block the remaining plumes, rather it deflects them without restriction keeping the fuel dynamics inside the injector nozzle unaltered. However, the introduction of this isolation shield may change the aerodynamics slightly or interact with the spray. In other work, this injector is used

to perform engine testing, and therefore it is desirable not to alter the nozzle when performing x-ray testing.

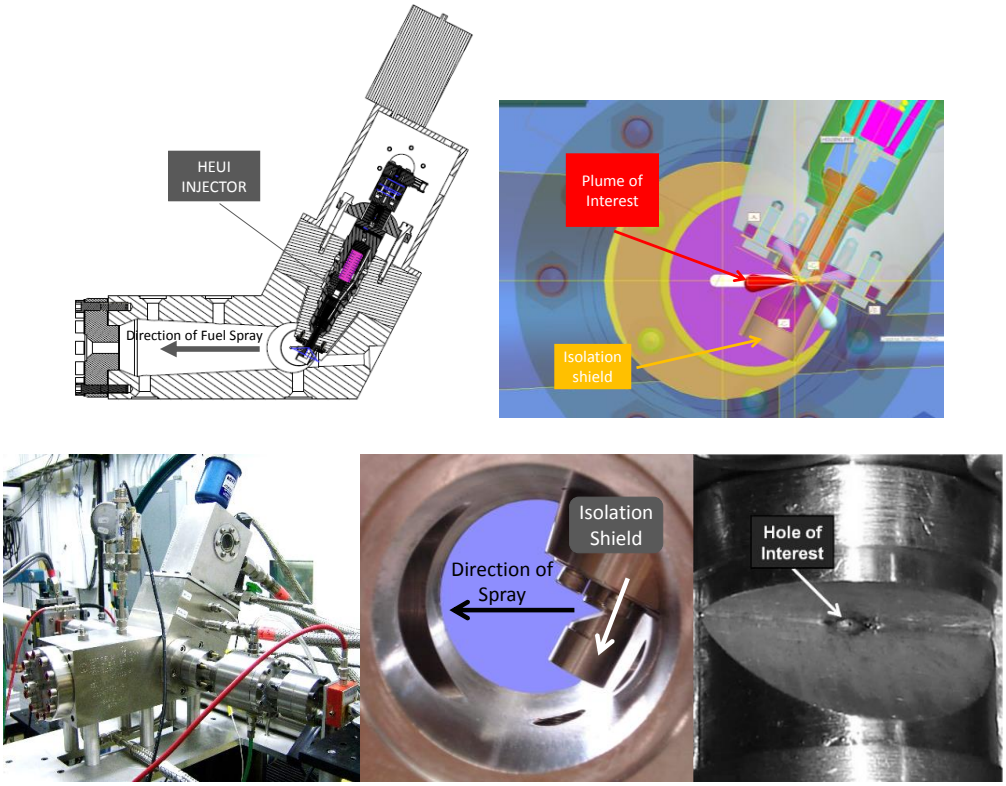

Figure 10. Angled spray chamber, isolation shield, and hole of interest

2.3 Rate of Injection Meter

To further understand the initial dynamics of the fuel spray, rate of injection studies were conducted using a Bosch rate of injection indicator [67]. The ROI is not only important in understanding

the spray dynamics, but is also essential for CFD modeling as it provides boundary conditions for fuel injection into the combustion chamber.

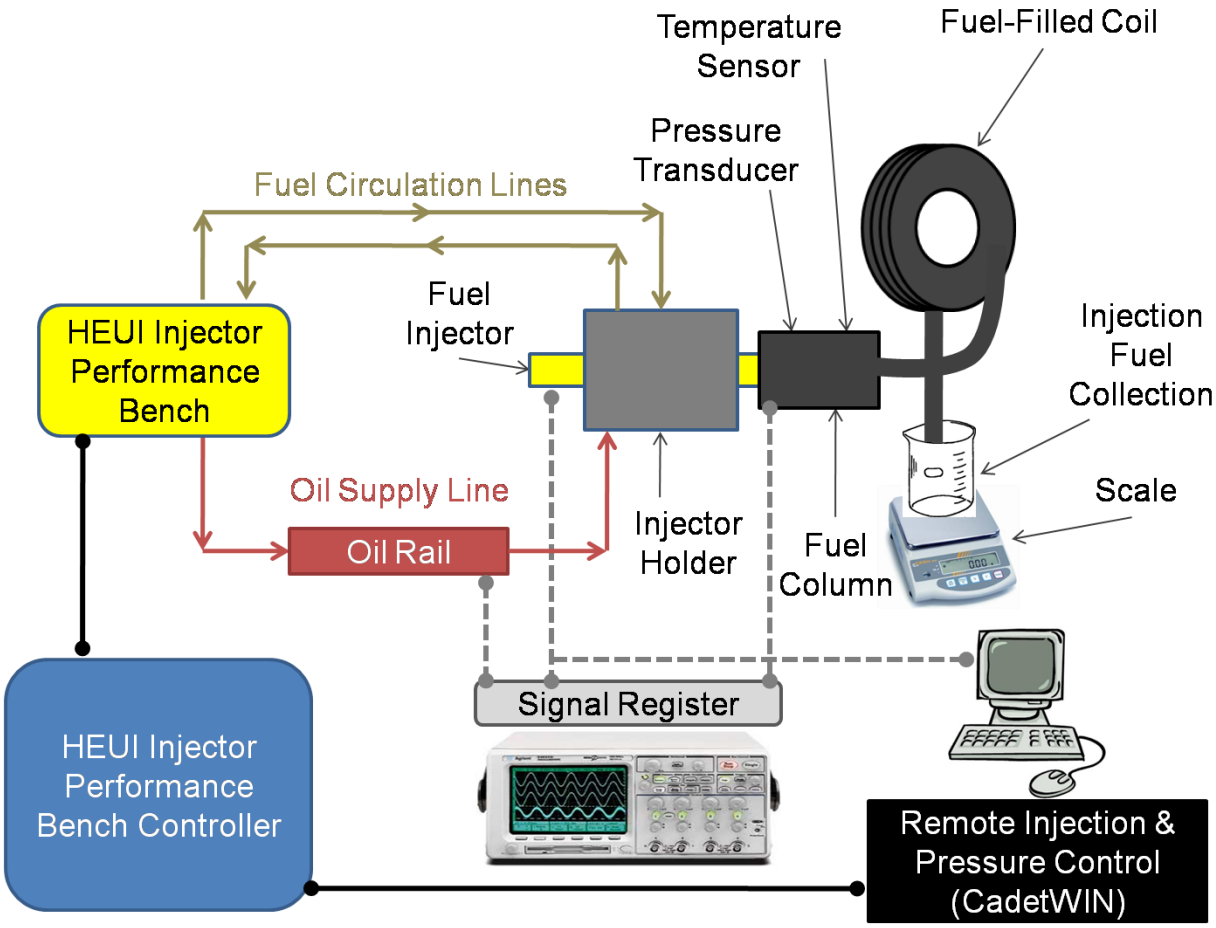

Figure 11. Schematic of Rate of Injection Test Setup

Figure 11 shows a schematic of the ROI test rig used in the present study. Signals from the pressure transducer on the rate meter, the high-frequency pressure sensor on the oil rail, and a meter monitoring the current supplied to the injector solenoid were registered on a digitizing oscilloscope. In

the present experiments, simulation of the x-ray experiment was achieved by maintaining the injection ambient pressure at 30 bar. The ensemble average of 512 signal traces was obtained from the low-pass filtered (30 kHz) ROI meter pressure signal. The total injection quantity was obtained 3750 injections at each condition. This total amount of fuel is used to scale the ROI plots obtained. Rate profiles were obtained for a range of oil rail pressures and injection deliveries. It is important to note that all 6 spray plumes were measured in the ROI experiments. When making comparisons of measured ROI profiles with x-ray data, it is assumed that an average of one-sixth the total fuel quantity is injected per orifice since a single spray was isolated in the x-ray work. However, total fuel injected from all 6 holes is used when comparing the measured ROI profiles to engine data.

2.4 Caterpillar Single Cylinder Engine and Support Equipment

A single-cylinder, simulated turbocharged research engine is used to perform these experiments. The Caterpillar 3401E, as it is commonly called, is a single-cylinder form of the 3406E truck engine which is turbocharged, and has direct injection and air-to-air aftercooling. The 3401E engine has been retrofitted to use the Caterpillar HEUI injection system and injector discussed previously. The HEUI is centrally mounted in the cylinder head and employs the use of a support cart to provide the oil necessary for actuation. Crankshaft position information is acquired from sensors on the crankshaft (used in cylinder pressure data acquisition) and also on the camshaft (used for injection control). Engine specifications are listed in Table I. Details regarding the test equipment are to be found in the subsequent sections.

Table I. Engine Specifications

Description	Value
Engine Model	Caterpillar 3401E
Bore	137.2 mm
Stroke	165.1 mm
Displacement	2.44 L
Compression Ratio	16.278:1 (measured on modified cylinder head)
Combustion Air System	Simulated turbocharger and air-to-air aftercooler
Fuel Injection System	HEUI 315B, six-hole tip
Injector Hole Size	169 micron (mini-sac), 126° Angle

2.4.1 Cylinder Head Modifications

A previously modified cylinder head was used for this work in order to accommodate the cylinder pressure transducer and the endoscope that are discussed in subsequent sections. The cylinder head can be viewed in Figure 12. Two intake and two exhaust valves are shown in the photograph along with the center-mounted HEUI injector. The cylinder pressure transducer entry to the combustion chamber is labeled on both photographs. Additional ports were created for endoscope access into the combustion chamber.

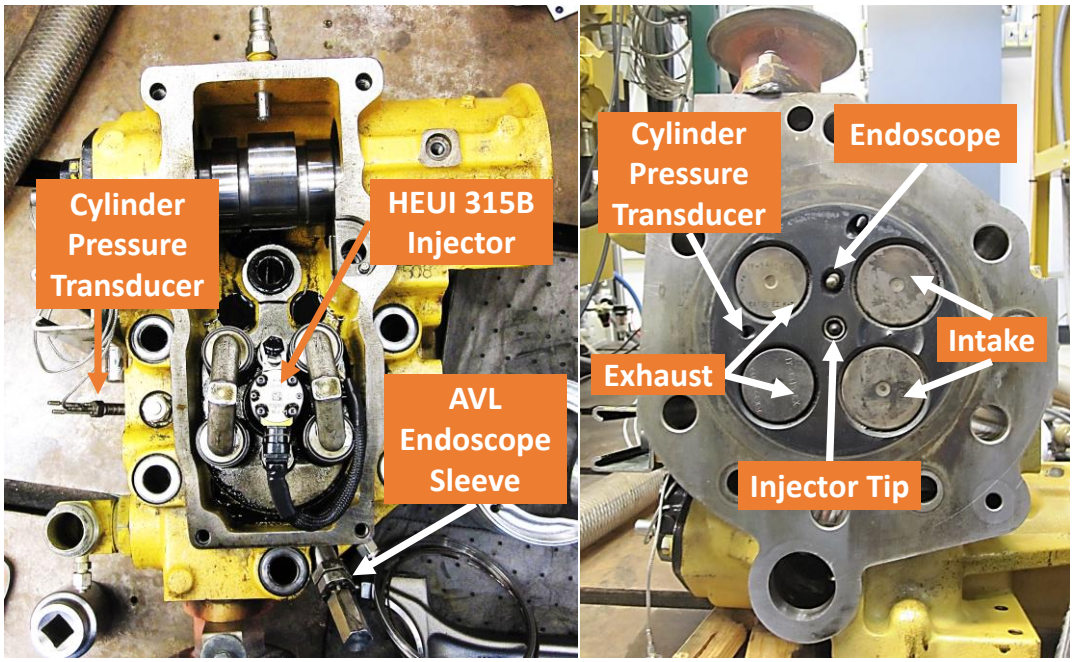

Figure 12. Modified cylinder head

2.4.2 Dynamometer

A General Electric model TG 1F 257 eddy current type dynamometer provides the load to the single cylinder engine. The measurements from the dynamometer are made using a reaction arm load cell which provides a feedback control signal. The dynamometer is controlled using a Digalog TestMate system in an absorb mode. For example, a constant speed set point is dictated in the Digalog controller. If fuel quantity is increased using CADetWIN, the engine speed will increase. The Digalog dynamometer controller will detect this increase and respond by increasing the load to maintain the engine speed at the desired set point. A flywheel and compressed air starter are located on the rear of the dynamometer rotor shaft. See Figure 13 for a view of the dynamometer setup used in this work.

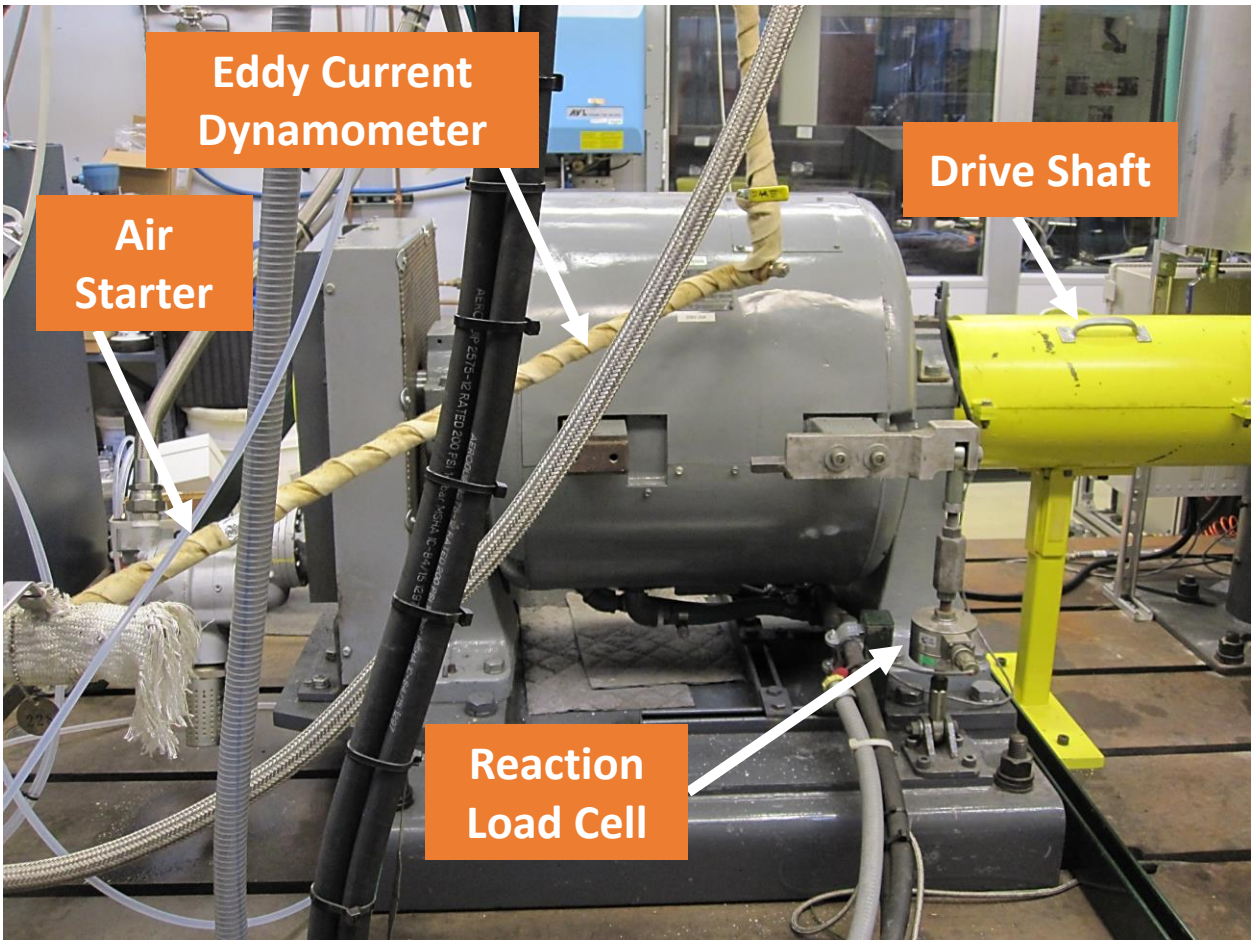

Figure 13. Engine dynamometer setup

2.4.3 Intake Air System

Intake air is acquired from a large air compressor in the test facility. The temperature and pressure of the air are regulated with Proportional-Integral-Derivative (PID) closed loop controllers in the Digalog system. These conditions are designed to simulate those of a turbocharger and aftercooler system of a typical multi-cylinder version of the Caterpillar (CAT) 3400 series engine. While the humidity of the air was not controlled, it was measured and recorded using a Vaisala metering device in order to make corrections in the exhaust emissions.

The CAT 3401 requires the use of a surge tank (Caterpillar part number 1Y3978) for dampening the unsteady airflow caused by a single-cylinder engine. The volume of the tank is 240 L which is approximately 100 times the displacement of the engine. The air in the tank is heated and controlled by the Digalog as mentioned previously. The intake air system can be viewed in Figure 14.

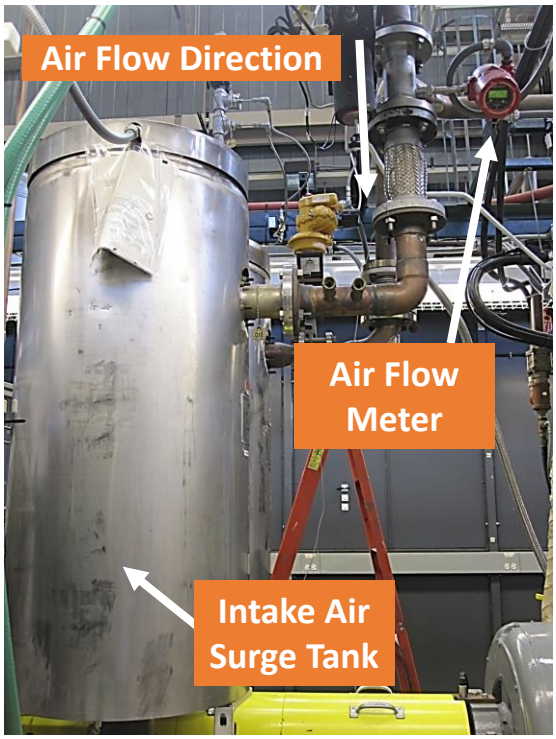

Figure 14. Intake air system

2.4.4 Exhaust Air System

A surge tank (Caterpillar part number 1Y3976) with identical geometry and volume as the intake surge tank was used for the engine exhaust. In order to simulate the back pressure normally created by a turbocharger system, a butterfly type restriction valve was located on the surge tank outlet. A PID loop in the Digalog system was used to control this valve and reach desired set points. The emissions measurements were taken after the restriction valve. The exhaust air system can be viewed in Figure 15.

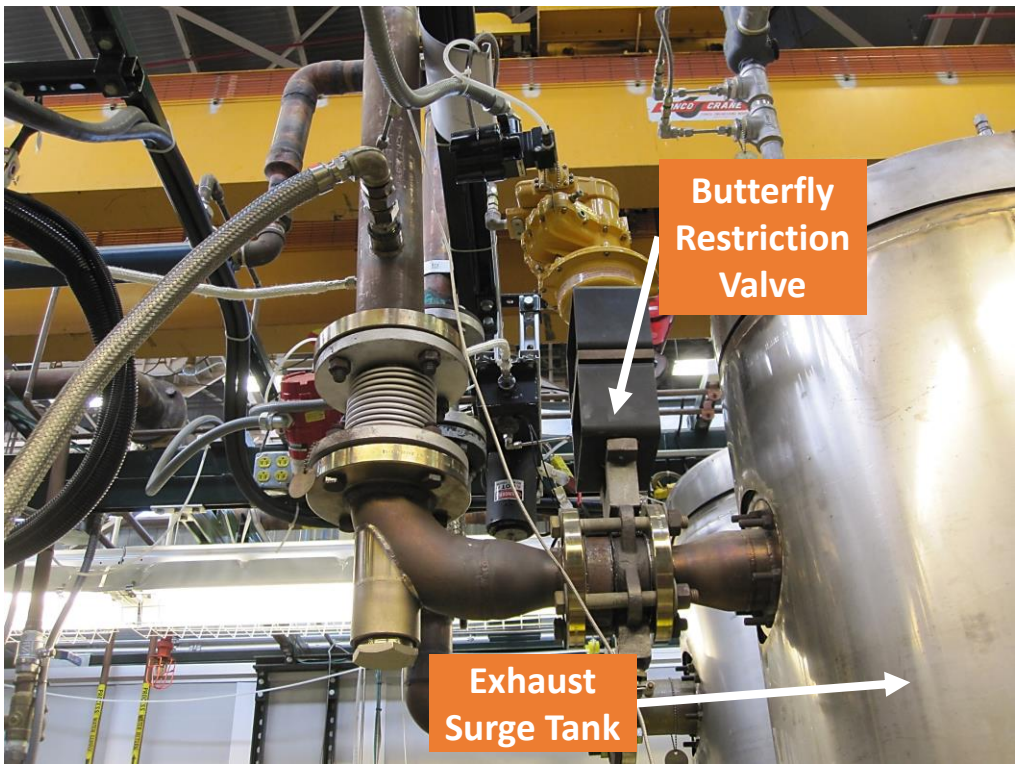

Figure 15. Exhaust air system

2.4.5 Fuel Mass Flow

A specific fueling cart was constructed so that small amounts of specialized fuel could be used in engine running. This design brought the fuel supply close to the engine so that minimal fuel was needed to fill the supply lines and thus enabled running the engine with quantities as low as 3 liters of fuel. On-board systems control temperature and pressure of the engine inlet fuel. When running on diesel, a 10-gallon reserve tank was used to supply the injector with fuel. If specialized fuel is used (i.e. Phytol blends in this work) the engine is warmed on diesel and then shut down, lines are flushed and quickly swapped to run out of a small reservoir of the precious fuel. The fueling system can be seen in Figure 16.

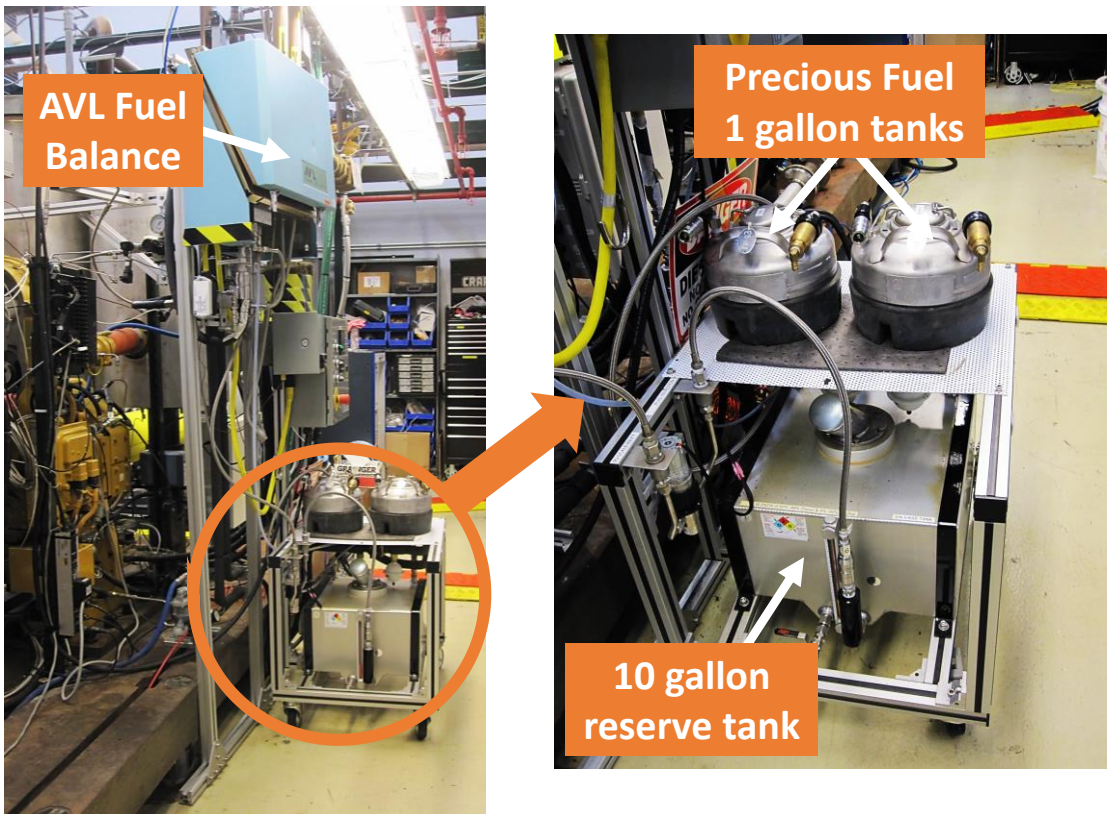

Figure 16. Specialized fueling system

Measurements of fuel flow are performed with an AVL 733S fueling scale balance system. This fuel balance works on a gravimetric measuring principle. A small measuring vessel is filled with a quantity of fuel from the desired fueling source (large reserve tank or smaller reservoirs). Fuel is supplied to the engine according to operator specifications while the system continuously measures the weight of the small measuring vessel [68]. This measurement is recorded into the Digalog logging system at a rate of 1 Hz. In the event that a fuel refill takes place during a data point recording, the fuel rate information is discarded and repeated.

2.4.6 Air Mass Flow

A Sierra Instruments model 780S mass flow meter is used to measure the engine combustion air flow. The flow meter is located upstream of the intake air surge tank and can be seen in Figure 14. This instrument is a hot-wire anemometer type flow sensor, thus a velocity sensor is heated to a temperature above the ambient gas temperature. The air cools the sensor as it passes, the constant temperature differential is maintained by electrical power that is directly proportional to the gas mass flow rate [69].

2.4.7 Emissions Measuring Equipment

Gaseous emissions were measured after exiting the exhaust surge tank, downstream of the butterfly restriction valve as can be seen in Figure 17. A multi-hole emissions probe was designed in accordance with the Code of Federal Regulations (CFR) title 40 part 86 specifications for heavy-duty engines.

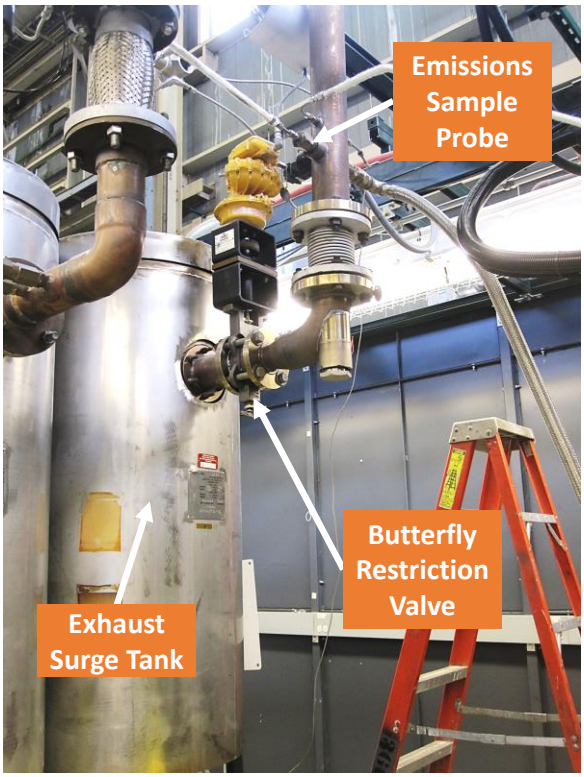

Figure 17. Location of Emissions Sample Probe

Emissions measurements were made using several pieces of equipment, including a Pierburg AMA 2000 bench with analyzers and sampling systems in accordance with CFR regulations. An image of the emissions sampling bench and analyzers can be seen in Figure 18.

Figure 18. Pierburg gaseous emissions sampling bench and analyzers

NO_x measurements were made with a chemiluminescent analyzer which is based on the reaction of NO with O_3 to produce NO_2 and O_2. As NO mixes with ozone, it produces excited NO_2 molecules and oxygen. As the excited NO_2 reverts to its ground state it emits photons which are measured by a photodiode and is proportional to the NO concentration [70].

Hydrocarbon volumetric measurements are made using a flame ionization detector (FID). The sample gas is drawn into a hydrogen flame in the interior of the FID. A metal collector detects ions that are produced as the hydrocarbons in the sample burn. The rate of ionization is proportional to the current across the detector, and hence also to the concentration of HC in the sample gas [71].

CO and CO_2 measurements are made with infrared (IR) analyzers. The gas sample is collected into the apparatus where it is exposed to IR radiation. The wavelength range of radiation absorption is dependent on the type of gas being evaluated. The radiation then passes through a sample column and a reference column and then reaches a detector which evaluates the reference and measurement beams and converts them into voltage signals proportional to intensity [72].

Paramagnetic measurement is performed for O_2 analysis. Within the analysis chamber a magnet creates a magnetic field of high inhomogeneity. Because of their paramagnetism, oxygen molecules entering the chamber are drawn towards the area of the highest magnetic field strength. A specially shaped apparatus in the analysis cell will experience torque caused by the forces of the O_2 molecules and thus begin rotating. A mirror on this apparatus will deflect an incident light onto a photodetector producing an electric voltage. This electric signal is amplified and fed back until it forces the apparatus to return to equilibrium position. This current needed to produce the restoring torque directly measures the concentration of O_2 in the sample gas [72].

2.4.8 Test Cell Control and Data Acquisition (Digalog)

A Digalog testmate system is used for controlling various temperatures and pressures and for logging general engine and test cell data. Closed PID loops are used for the control of intake air pressure and temperature, exhaust back pressure, engine coolant temperature, and engine oil temperature. General data such as torque, engine speed, air mass flow, as well as data from the emissions bench and fuel scale balance are harvested by the Digalog. At each data point measurement, the Digalog records one minute of data at a rate of 1 Hz.

2.4.9 Cylinder Pressure

A piezoelectric, water-cooled pressure transducer (Kistler 6043) with a charge amplifier (Kistler 5010B) was used to acquire data on the cylinder pressure. The cylinder pressure transducer is calibrated on a regular basis and values are entered into the data acquisition system converting the voltage signal into a pressure reading. Cylinder pressure data was acquired using a high speed data acquisition system (either WIN600 or AVL INDICOM) and post-processed for combustion analysis.

2.4.10 Engine Crankshaft Angle Measurement

The crankshaft position was measured using an AVL 364X crank angle encoder disc with 720 slits and a pulse pickup (AVL part number 364G.03). The infrared light sensor creates a square wave signal depicting crank angle position with a resolution is 0.5 °CA and is brought to 0.1 °CA using a signal multiplier. The crank angle position data was used in the acquisition of cylinder pressure data and to synchronize optical imaging data. Depending on availability, two different cylinder pressure data acquisition systems were used: Hi-Techniques WIN600 or AVL IndiCOM.

2.4.11 High Speed Data Acquisition for Combustion Analysis

The crankshaft position signal received from the encoder and the cylinder pressure signals were recorded and processed using two different systems (depending on availability). For combustion analysis, the Hi-Techniques WIN600 system used the program REVelation, while the AVL IndiCOM system used the program Concerto. Both systems acquired multiple (100) combustion events in sequence. The signals were then processed for analysis along with statistical data.

2.5 In-Cylinder Combustion Imaging

Combustion visualization was performed by using a commercial endoscope system (AVL Visioscope). This system consists of a 12-bit resolution 640 × 480 pixel VGA digital color camera, and a 4-mm-diameter endoscope. A 60° endoscopic window angle was used to acquire the images presented in this work. Figure 19 shows the locations of endoscope access and a sample view of the combustion. More details regarding the endoscope system used can be found in other work [73,74].

Images can be obtained due to the luminosity of the soot during combustion. The combustion in the cylinder produces luminous flames with light intensity dependent on the number density of soot particles. It is important to note that the combustion images are obtained in a 2-dimensional line-of-sight integrated fashion. For example, the camera will capture luminosity at all x-y pixel locations by integrating in the z-direction so that combustion happening in the foreground blends with that occurring in the background at any specific pixel location. Also, each set of data comes from the ensemble average of many individual combustion events. The AVL Visioscope system receives crank angle information from the angle encoder. It takes the first image at the designated crank angle (i.e. 4 °BTDC), in the next cycle it moves over one time step (i.e. 3.5 °BTDC) and takes the next image with ½ crank angle degree resolution. These images are stitched together to create a complete combustion event at a certain engine condition. Each engine condition is repeated multiple times to provide statistical data regarding repeatability. Once the images are obtained, 2-color optical pyrometry coupling the phenomena of soot luminosity and radiation can be employed to find temperature and soot volume fraction distribution in an integrated line-of-sight fashion. AVL ThermoVision software was used to post-process the acquired images [74,75,76,77,78].

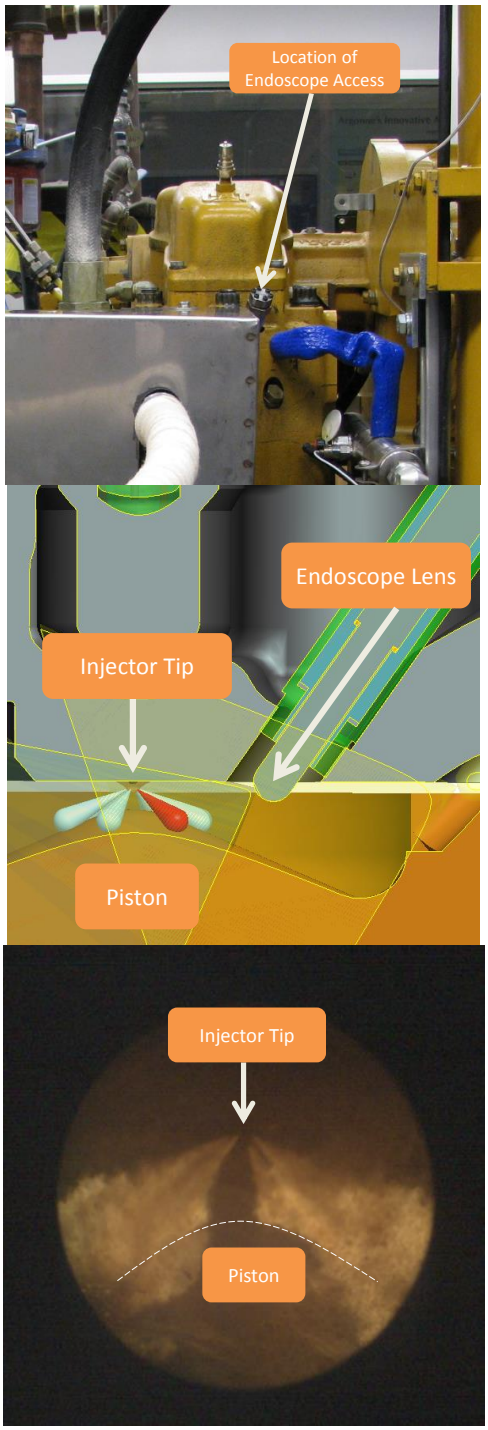

Figure 19. (top) Location of endoscope access in head, (middle) visualization of location of endoscope entry into the combustion chamber, (bottom) sample endoscope image with labeled injector tip and piston crown indicated with dashed line

3 THEORY AND CALCULATIONS

Parts of this chapter have been previously published as:

Ramírez, A.I., Som, S., Aggarwal, S.K., Kastengren, A.L., El-Hannouny, E.M., Longman, D.E., Powell, C.F.: Quantitative X-Ray Measurements of High-Pressure Fuel Sprays from a Production Heavy Duty Diesel Injector. *Experiments in Fluids*, 47(1):119-134, 2009.

This chapter will outline the theory behind the various techniques used in this work. It will explain governing equations and how calculations were made.

3.1 X-Ray Radiography

X-ray radiography technique is used in this work for studying the near-nozzle portion of the spray. Scattering that is seen in optical techniques is negligible in x-ray radiography because of the x-ray beam's small cross-section and short wavelength. The x-ray intensities before and during the spray event relate to the mass of fuel in the beam path using an application of the Beer-Lambert Law as seen in equation (1).

$$\frac{I}{I_0} = e^{-\mu M} \tag{1}$$

μ = absorption coefficient of the fuel, [$mm^2/\mu g$]

M = projected density of the fuel in the beam path, [$\mu g/mm^2$]

I = x-ray intensity during the spray event, [keV]

I_0 = x-ray intensity before the spray event, [keV]

The synchrotron x-ray produced at the Advanced Photon Source (APS) at Argonne National Laboratory (ANL) produces monochromatic x-ray beams. This monochromaticity of the x-ray beam allows for this direct relationship with only one mass attenuation coefficient. For safety reasons, instead of using diesel

in the fuel injection system, Viscor, a diesel calibration fluid, with cerium additive was used in x-ray radiography experiments. In order to find the mass attenuation coefficient, a calibration is performed at the start of the x-ray experiments. Capillary tubes filled with water, air, and the doped fuel are put in the beam. Since the mass attenuation of water and air are well known, they are used to determine the attenuation of the capillary tube and its inner diameter. The beam size and the density of the fuel are known, therefore the mass of the fuel illuminated by the x-ray beam is determined by the path length.

An in-house code called ViewScopeData8 created by Powell and Kastengren was used for post-processing data.

3.2 Rate of Injection

A Bosch-type ROI meter is used to measure the ROI profiles at specific injection conditions. A simplified schematic of the rate meter can be found in Figure 20. The injector mount holds the injector with the tip at the start of the measurement tube where fuel temperature and pressure are measured.

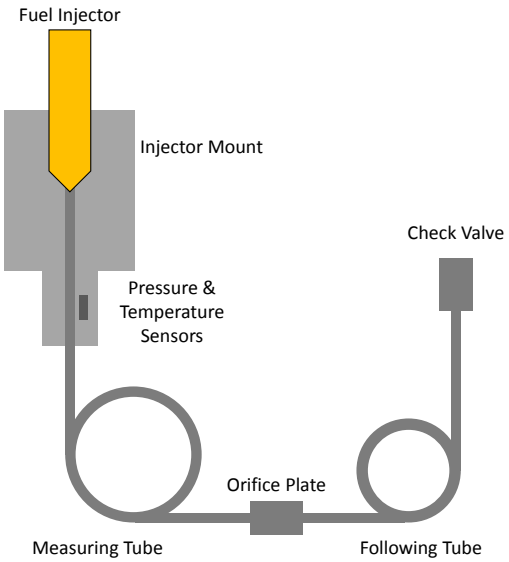

Figure 20. Schematic of ROI measurement

The injector introduces fuel into the device until the column and coil are completely full of diesel (or the fuel of choice). A pressure wave is produced as fuel is injected into the column of compressible fluid. The size of an orifice between the measuring and following tubes determines the portion of the pressure wave that is reflected and that which enters the following tube. There is a check valve at the end of the following tube which is used to adjust the back pressure.

The principle behind the injection rate measurements involves the pressure-velocity equation for a single wave in non-stationary flow. Assuming one-dimensional motion, this is given in equation (2).

$$P = \rho \cdot a \cdot u \tag{2}$$

P = pressure, [N/m^2]

ρ = density of fluid, [kg/m^3]

a = speed of sound in fluid, [m/s]

u = flow velocity, [m/s]

Combining with the continuity equation, the governing equation for the rate profile calculations is shown in equation (3).

$$\frac{dq}{dt} = \frac{P \cdot A}{\rho \cdot a} \tag{3}$$

q = injected volume of fuel, [m^3]

t = time, [s]

P = pressure, [N/m^2]

A = flow area, [m^2]

ρ = density of fluid, [kg/m^3]

a = speed of sound in fluid [m/s]

Integrating the volumetric flow rate ($\frac{dq}{dt}$) from this equation will produce the injected volume. More details regarding the Bosch-type rate meter can be found in other work [67,79].

3.3 Engine Cylinder Pressure

Cylinder pressure high speed data was acquired using a piezo-electric cylinder pressure transducer as discussed in previous sections. The data was obtained at each half crank angle and a signal multiplier was used to bring the data to one-tenth crank angle resolution. Once obtained, the data were analyzed using the AVL Concerto software [80].

3.3.1 Engine Cylinder Pressure Data Analysis

Analysis of the cylinder pressure data begins with the first law of thermodynamics for an open system at quasi-static conditions (uniform temperature and pressure). This can be expressed as shown in equation (4).

$$\frac{dQ}{dt} - p\frac{dV}{dt} + \sum_i \dot{m}_i h_i = \frac{dU}{dt} \tag{4}$$

$\frac{dQ}{dt}$ = heat transfer rate across the system boundary into the system, [J/s]

$p\frac{dV}{dt}$ = rate of work transfer done by the system due to system boundary displacement, [J/s]

$\dot{m}_i$ =mass flow rate into the system across the system boundary at location *i*, [kg/s]

h_i =enthalpy of flux, *i*, entering or leaving the system, [J/kg]

U = energy of the material contained in the system boundary, [J]

As is discussed in Heywood [12], there are several complications to this approach. Included in these is the gas in the crevice regions which would have an effect on the heat transfer and the density in the cylinder. However, for facility, this crevice volume is omitted for all calculations while the system is studied in the time interval when all the intake and exhaust valves are closed. An additional assumption is that there is uniform temperature in the system at each instant in time during the analysis. For a direct-injected engine as the one in this study, the only mass transfer into the cylinder during this time is the fuel being introduced through the injector. Incorporating all of the aforementioned conditions, equation (4) becomes equation (5)

$$\frac{dQ}{dt} - p\frac{dV}{dt} + \dot{m}_f h_f = \frac{dU}{dt} \tag{5}$$

$\frac{dQ}{dt}$ = heat transfer rate across the system boundary into the system, [J/s]

$p\frac{dV}{dt}$ = rate of work transfer done by the system due to system boundary displacement, [J/s]

$\dot{m}_f$ =mass flow rate of fuel into the system across the system boundary [kg/s]

h_f =enthalpy of flux of fuel entering the system, [J/kg]

U = energy of the material contained in the system boundary, [J]

Since the sensible enthalpy of the fuel is very low, the term $\dot{m}_f h_f$ is assumed to be negligible. The apparent heat release is then expressed as shown in equation (6).

$$\frac{dQ_n}{dt} = p\frac{dV}{dt} + \frac{dU_s}{dt} \tag{6}$$

$\frac{dQ_n}{dt}$ = Apparent heat transfer rate across the system boundary into the system, [J/s]

$p\frac{dV}{dt}$ = rate of work transfer done by the system due to system boundary displacement, [J/s]

$\frac{dU_s}{dt}$ = Rate of change of the sensible energy of the cylinder contents, [J/s]

Further assumption that the contents of the cylinder can be modeled as an ideal gas yields the final equation that is used for the apparent heat release rate shown in equation

$$\frac{dQ_n}{dt} = \left(\frac{\gamma}{\gamma - 1}\right)p\frac{dV}{dt} + \left(\frac{1}{\gamma - 1}\right)V\frac{dp}{dt} \tag{7}$$

$\frac{dQ_n}{dt}$ = Apparent heat transfer rate across the system boundary into the system, [J/s]

$p\frac{dV}{dt}$ = rate of work transfer done by the system due to system boundary displacement, [J/s]

V = Cylinder volume, [m^3]

$\frac{dp}{dt}$ = Rate of change of cylinder pressure, [Pa/s]

γ = polytropic coefficient (ratio of specific heats $\frac{c_p}{c_v}$)

The AVL Concerto software [80] is used for post-processing the cylinder pressure data. The Thermodynamics2 function is used which computes heat release rate using variable polytropic coefficients. Because of the combustion process, the cylinder gas composition and temperature will be different during the compression and expansion strokes. The Thermodynamics2 function uses a different γ value for the compression and expansion strokes, yielding higher accuracy in the expansion. Integrating equation (7) with respect to time will give the net heat release. Mass fraction burned locations can then be calculated from this curve.

Bulk gas temperature is calculated from the measured cylinder pressure in addition to the geometry input. Assuming a uniform gas temperature within the cylinder this calculation can be performed on the gas trapped in the combustion chamber between intake valve close (IVC) and exhaust valve open (EVO) time. Starting with an adaptation of the ideal gas law, mean gas temperature at any location can be found with equation (8).

$$T_i = \frac{P_i V_i}{\ell m_{th} R} \tag{8}$$

T_i = Mean gas temperature at crank angle location, *i*, [K]

P_i = Pressure inside the cylinder (measured) at crank angle location, *i*, [N/m^2]

V_i = Cylinder volume (based on engine geometry and encoder position) at crank angle location, *i*, [m^3]

V_i = Cylinder volume (based on engine geometry and encoder position) at crank angle location, *i*, [m^3]

ℓ = Volumetric efficiency

m_{th} = Theoretical air mass, [kg]

R = Gas constant for air, 287.12 [kJ/kg-K]

Where the theoretical mass is found using equation (9).

$$m_{th} = \frac{V_H P_{IVC}}{R T_{IVC}} \tag{9}$$

V_H = Swept volume, [m^3]

P_{IVC} = Air pressure at IVC (measured at air intake), [N/m^2]

T_{IVC} = Air temperature at IVC (measured at air intake), [K]

3.3.2 Initial Procedures for Engine Cylinder Pressure

Pegging of the cylinder pressure signal is done using the INDICOM software by means of a thermodynamic zero-level correction subroutine. Here the calibration factor for the signal is given based on the pressure transducer which converts the voltage signal to pressure. The subroutine uses a typical polytropic coefficient for DI diesel engines is used (1.37) for cylinder pressure between two points in the compression portion of the cycle. Assuming adiabatic compression between the two crank angle locations, the pressure signal is adjusted to yield an appropriate value as shown in equation (10)

$$P_1 = \frac{\Delta P}{\left(\frac{V_1}{V_2}\right)^{\gamma} - 1} \tag{10}$$

P_1 = Cylinder pressure at crank angle location 1, [bar]

ΔP = Cylinder pressure difference between crank angle location 2 and 1, [bar]

V_i = Cylinder volume at location *i*, [m^3]

γ = Polytropic coefficient

The location of top dead center (TDC) in the engine cycle must be located dynamically. The INDICOM software is used for doing this. The angle encoder properties are inputted (model number, number of markings) into the software. Since a motoring dynamometer is not available, a different approach is used to achieve a motored engine. The engine is run until it is sufficiently warm, then fuel injection is stopped. The engine continues to turn over at a reasonable speed. The TDC determination subroutine is started and returns a value. This process is repeated multiple times until repeatability is visible. The value is stored in the software, and all of the data is adjusted by this amount. Since there were several engine disassemblies and encoder adjustments throughout the course of this research a single value is not available. Rather, a TDC determination was performed each time the engine or encoder was adjusted.

3.4 Engine Performance

For better understanding of the performance and the efficiency of the engine at certain conditions the following parameters are analyzed in accordance with the Society of Automotive Engineers (SAE) standard J1349 [81]. Because of changes in barometric pressure and ambient temperature that can be experienced on different test times, corrections must be made to the calculations.

Engine brake power is the usable power delivered by the engine to the load source [12]. Corrected brake power multiplies the observed brake power by an ambient pressure and temperature correction factor and is calculated as shown in equation (11). For ease, in the results and discussion corrected brake power, P_b^*, will be referred to simply as brake power.

$$P_b^* = P_{b\_observed} \cdot \left[\left(\frac{99}{P_{inlet\_air}} \right)^{0.7} \left(\frac{T_{inlet\_air}}{298} \right)^{1.5} \right]^{0.3} \quad (11)$$

P_b^* = Corrected brake power, [kW]

$P_{b\_observed}$ = Observed brake power (measured), [kW]

P_{inlet_air} = Pressure of inlet air (measured), [kPaA]

T_{inlet_air} = Temperature of inlet air (measured), [K]

Brake specific fuel consumption (BSFC) shows how efficiently the fuel is being used to supply work by the engine. It can be expressed as in equation (12).

$$BSFC = \frac{\dot{m}_f}{P_b^*}(60) \quad (12)$$

BSFC = Brake specific fuel consumption, $\left[\frac{g}{kW \cdot h} \right]$

$\dot{m}_f$ = Fuel flow into the cylinder (measured), [g/min]

P_b^* = Brake power, [kW]

(60 is a unit conversion coefficient)

A similar value is the brake thermal efficiency (BTE), however, BTE takes into account the energy of the particular fuel that is being used. It is a measure of how well the engine is able to convert the energy from the fuel into usable energy as shown in equation (13). This parameter is particularly useful when comparing different fuels at similar engine conditions.

$$BTE = \frac{P_b^*}{Q_{LHV}\dot{m}_f}(6 \cdot 10^9) \tag{13}$$

BTE = Brake thermal efficiency, [%]

P_b^* = Brake power, [kW]

Q_{LHV} = Lower heating value of fuel (measured), [J/kg]

$\dot{m}_f$ = Fuel flow into the cylinder (measured), [g/min]

($6 \cdot 10^9$ is a unit conversion coefficient)

Brake mean effective pressure (BMEP) measures an engine's ability to do work. By dividing brake power by the engine displacement allows this parameter to be useful when comparing outputs from engines of different size. BMEP is calculated as shown in equation (14).

$$BMEP = \frac{P_b^* n_R}{V_d N}(0.6) \tag{14}$$

BMEP = Brake mean effective pressure, [bar]

P_b^* = Brake power, [kW]

n_R = Number of crank revolutions per power stroke, per cylinder (2 in a 4-stroke engine)

V_d = Engine displacement (measured), [m^3]

N = Crankshaft rotational speed (measured), [rpm]

(0.6 is a unit conversion coefficient)

3.5 Engine Emissions

Gaseous emissions were measured using the equipment described in section 2.4.7. The equipment is calibrated on a yearly basis by a qualified professional. In addition, daily passes of span and zero gases are performed before data is collected to correct any possible drift. The emissions bench reports carbon monoxide (CO), nitrogen oxides (NO_x), and hydrocarbons in parts per million (ppm) and carbon dioxide (CO_2) and oxygen (O_2) in percent volume values. These raw numbers are processed in accordance with the Code of Federal Regulations (CFR) Title 40, Chapter 1, Part 86, Subpart D for gaseous emissions from heavy duty diesel engines [82]. Brake specific emissions values are reported throughout this work by dividing the processed raw emission flow rate by the brake power.

3.6 In-Cylinder Combustion Imaging – 2-Color Optical Pyrometry

Two-color optical pyrometry is a well-established technique for measuring temperature. This technique has been used in engine applications for understanding temperatures and soot volume fraction in the cylinder [74].Detailed explanations of the technique can be found in the aforementioned references. For the present work, all in-cylinder endoscopy was performed using the AVL Visioscope system as discussed in Section 2.5. The accompanying AVL Thermovision software was used for analysis of the data collected [73].

The basis of two-color optical pyrometry couples radiation theory with the luminosity of the soot in the combustion. A perfect emitter of radiation in a continuous spectrum is referred to as a black body and has an emissivity of 1. Anything differing from this is a non-black body or gray body radiator. Soot particles, or a dense soot cloud behave in a manner that is very close to black body radiation. Thinner soot clouds behave more like gray body emitters, deviating from black body radiation by the factor ε_λ, the spectral emissivity ($\varepsilon_\lambda<1$) [83].

The monochromatic intensity of a black body is given in Planck's equation (15) and shows that the intensity of radiation from a blackbody depends on temperature and varies with wavelength.

$$I_{b,\lambda}(T) = \frac{C_1}{\lambda^5\left[e^{\left(\frac{C_2}{\lambda T}\right)} - 1\right]} \quad (15)$$

$I_{b\lambda}$ = Spectral intensity of black body, [W/m^3]

λ = Wavelength, [μm]

T = Absolute temperature, [K]

C_1 = 3.7418 × 10^{-16} (Planck constant), [Wm^2]

C_2 = 1.4388 × 10^{-2} (Planck constant), [mK]

The monochromatic intensity of a non-black body is a fraction of the black body radiation emitted at the wavelength as shown in equation (16).

$$\varepsilon_\lambda = \frac{I_\lambda(T)}{I_{b,\lambda}(T)} \quad (16)$$

ε_λ = Monochromatic emissivity

$I_\lambda(T)$ = monochromatic emissive power of a non-black body at temperature, T and wavelength, λ, [W/m^3]

$I_{b,\lambda}(T)$ = monochromatic emissive power of a black body at temperature, T and wavelength, λ, [W/m^3]

λ = Wavelength, [μm]

T = Absolute temperature, [K]

The apparent temperature is that at which a blackbody will emit the same radiation intensity of a non-black body at a temperature.

$$I_{b,\lambda}(T_a) = I_{\lambda}(T) \tag{17}$$

$I_{b,\lambda}(T_a)$ = monochromatic emissive power of a black body at the apparent temperature, T_a, [W/m^3]

$I_{\lambda}(T)$ = monochromatic emissive power of a non-black body at temperature, T, [W/m^2].

T_a = Apparent temperature, [K]

λ = Wavelength, [μm]

T = Absolute temperature, [K]

Combining equations (16) and (17):

$$\varepsilon_{\lambda} = \frac{I_{b,\lambda}(T_a)}{I_{b,\lambda}(T)} \tag{18}$$

ε_{λ} = Monochromatic emissivity

$I_{b,\lambda}(T_a)$ = monochromatic emissive power of a black body at the apparent temperature, T_a and wavelength, λ, [W/m^3]

$I_{b,\lambda}(T)$ = monochromatic emissive power of a black body at temperature, T and wavelength, λ, [W/m^3]

λ = Wavelength, [μm]

T = Absolute temperature, [K]

T_a = Apparent temperature, [K]

Introducing Planck's equation [see equation (15)] into equation (18):

$$\varepsilon_\lambda = \frac{e^{\left(\frac{C_2}{\lambda T}\right)} - 1}{e^{\left(\frac{C_2}{\lambda T_a}\right)} - 1} \tag{19}$$

ε_λ = Monochromatic emissivity

C_2 = 1.4388 × 10^{-2} (Planck constant), [mK]

λ = Wavelength, [μm]

T = Absolute temperature, [K]

T_a = Apparent temperature, [K]

Monochromatic emissivity of a soot particle was modeled by Hottel and Broughton [84] for a luminous flame as shown in equation (20). The soot absorption coefficient (K) is proportional to the number density of soot particles and the parameter (α) depends on the optical and physical properties of the soot in the flame. This correlation was validated by Matsui et. al. in diesel engine studies using three wavelengths [85].

$$\varepsilon_\lambda = 1 - e^{\left(\frac{-KL}{\lambda^\alpha}\right)} \tag{20}$$

ε_λ=Spectral emissivity

λ = Wavelength, [μm]

K = Soot absorption coefficient, [1/cm]

L = line of sight path length through flame [cm]

α = parameter

Combining equations (19) and (20) and solving for the KL factor:

$$KL = -\lambda^{\alpha} \ln\left[1 - \left(\frac{e^{\left(\frac{C_2}{\lambda T}\right)} - 1}{e^{\left(\frac{C_2}{\lambda T_a}\right)} - 1}\right)\right] \tag{21}$$

K = Soot absorption coefficient, [1/cm]

L = line of sight path length through flame [cm]

λ = Wavelength, [μm]

α = parameter

$C_2 = 1.4388 \times 10^{-2}$ (Planck constant), [mK]

T = Absolute temperature, [K]

T_a = Apparent temperature, [K]

Rewrite this equation for two different, specific wavelengths, λ_1 and λ_2 and set them equal to each other. Note, the actual flame temperature (T) is wavelength independent while the apparent temperature (T_a) and the parameter (α) are wavelength dependent.

(22)

$$\left[1-\left(\frac{e^{\left(\frac{C_2}{\lambda_1 T}\right)}-1}{e^{\left(\frac{C_2}{\lambda_1 T_{a_1}}\right)}-1}\right)\right]^{\lambda_1^{\alpha_1}}=\left[1-\left(\frac{e^{\left(\frac{C_2}{\lambda_2 T}\right)}-1}{e^{\left(\frac{C_2}{\lambda_2 T_{a_2}}\right)}-1}\right)\right]^{\lambda_2^{\alpha_2}}$$

λ_i = Specific wavelength i, [μm]

α_i = parameter at specific wavelength λ_i

$C_2 = 1.4388 \times 10^{-2}$ (Planck constant), [mK]

T = Absolute temperature, [K]

T_{ai} = Apparent temperature at specific wavelength λ_i, [K]

The two wavelengths λ_1 and λ_2 are selected, while the apparent temperatures T_{a1} and T_{a2} are measured using a calibrated 2-color pyrometer. With this information known, equation (22) can be solved for absolute temperature (T).

The KL factor can be used as a measure of the soot concentration as in equation [86]. This emissivity model was verified by Flynn et. al. in a direct injected diesel engine using different wavelengths [87].

(23)

$$KL = C_0 \frac{f_V}{\lambda} L$$

K = Soot absorption coefficient, [1/cm]

L = line of sight path length through flame [cm]

λ = Wavelength, [μm]

C_0 = Empirical constant

F_V = Soot volume fraction [cm^3-soot/cm^3]

Before taking engine combustion images, a zero image of the combustion chamber must be taken. This is done by inserting the endoscope while the engine is not running and taking an image of the dark combustion chamber. This serves as a calibration image for the ThermoVision software in order to derive the optical thickness. Temperature distribution and soot volume fraction are then calculated.

4 RESULTS – X-RAY FUEL SPRAY STUDY

Parts of this chapter have been previously published as:

Ramírez, A.I., Som, S., Aggarwal, S.K., Kastengren, A.L., El-Hannouny, E.M., Longman, D.E., Powell, C.F.: Quantitative X-Ray Measurements of High-Pressure Fuel Sprays from a Production Heavy Duty Diesel Injector. Experiments in Fluids, 47(1):119-134, 2009.

The initial portion of this work sought better understanding of the fuel spray from the HEUI 315 B injector. This was accomplished by studying the rate of injection and the initial portion of the fuel spray using x-ray radiography. Data obtained was used for validations of numerical simulations performed by Dr. Sibendu Som [13,88]. As it will be shown in the subsequent text, the rate of injection profile is of particular interest in the behavior of the resulting spray.

4.1 Rate of Injection

Rate measurements were performed by the technique described in Sections 2.3 and 3.2. The ROI profiles for the oil rail pressures of 17 and 21 MPa are shown in Figure 21. The zero time in this plot is the time at which the current to the injector solenoid begins. Both cases show similar delay between commanded start of injection (SOI) and apparent SOI, and have comparable rate shapes. As expected, the higher rail pressure yields a higher peak value of ROI with a slightly quicker initial rise than the 17 MPa case. A notable feature of both rate profiles is the slower rise to the “steady state” injection period than that with single-fluid, single-hole common rail injection systems [89]. This slower rate during the SOI is characteristic of HEUI systems and is caused by the internal fluid dynamics. It should be mentioned that the ROI profiles shown are for a combination of all six orifices.

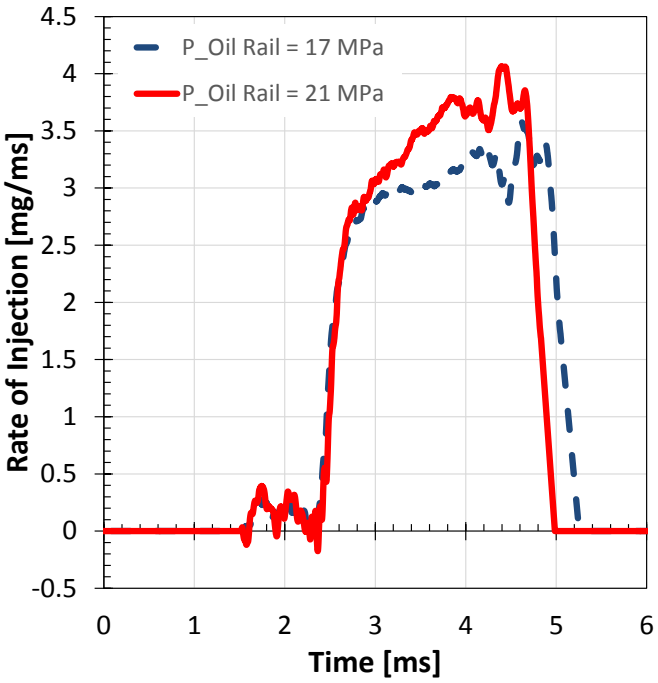

Figure 21. Rate of injection profiles for 17 and 21 MPa oil rail pressures, 30 bar ambient pressure, 100 mm^3 per stroke fuel delivery. The transition period of rapid increase to quasi-steady injection is marked.

Using the ROI profile for the early transition region ($t < 0.2$ ms), as shown in Figure 22, as an input to the numerical model yields gross underprediction of penetration lengths (cf. Figure 23). Further investigation revealed that directly scaling the injection rate from six-sprays to a single spray in the transition region might cause this underprediction. According to the control volume analysis by Kastengren et al. [65], x-ray radiography can be used to compute the total spray mass, and hence ROI, until the spray has reached the downstream end of the measurement domain. Figure 2122(a) presents the ROI obtained from the x-ray data up to 0.2 ms at the first measurement location (0.283 mm). The lines represent a linear fit to the data.

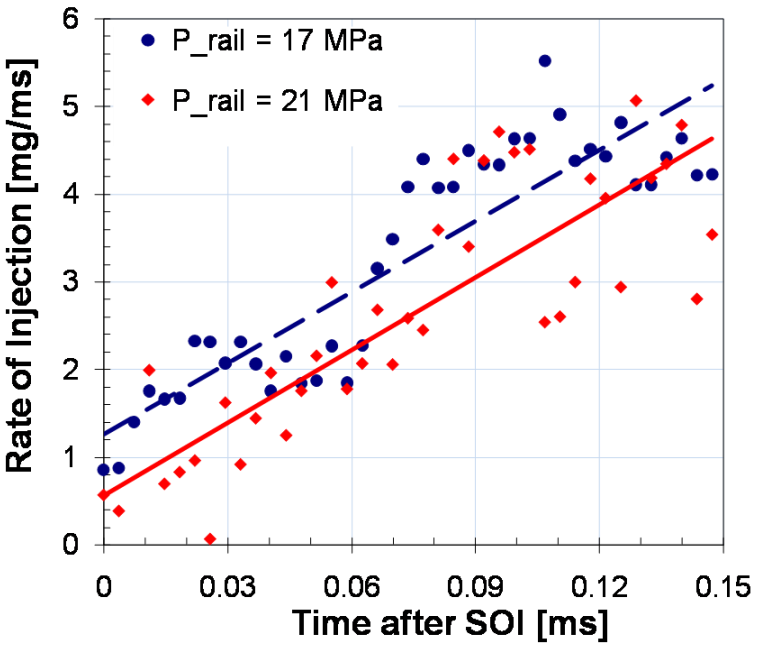

(a)

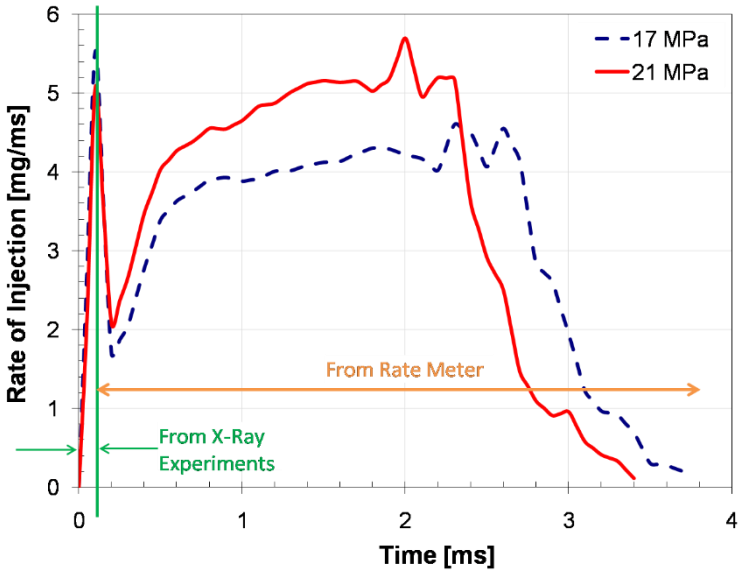

(b)

Figure 22. (a) Rate of injection calculated from x-ray radiography measurements (linear fits shown) for 17 and 21 MPa oil rail pressure. (b) Hybrid ROI profile of a single orifice used for input in numerical simulation.

For the STAR-CD simulations, the early transient portion of the rate profile was joined with the later steady-state portion obtained from the meter. Since one spray plume is simulated, the total fuel injected was kept to one-sixth the total fuel injected from the nozzle. This newly constructed profile is shown in Figure 22(b). The plot is marked noting the area extracted from x-ray data and that taken from the rate meter.

4.2 Liquid Penetration

Comprehensive data analysis was performed to investigate the near-nozzle spray characteristics using the x-ray radiography measurements. Liquid penetration was obtained by determining the time at which the leading edge of the fuel arrives at each axial location. This was done by recording the time at which the x-ray intensity decreases by a threshold value of 25%, indicating absorption by the fuel at each axial location in the experimental domain.

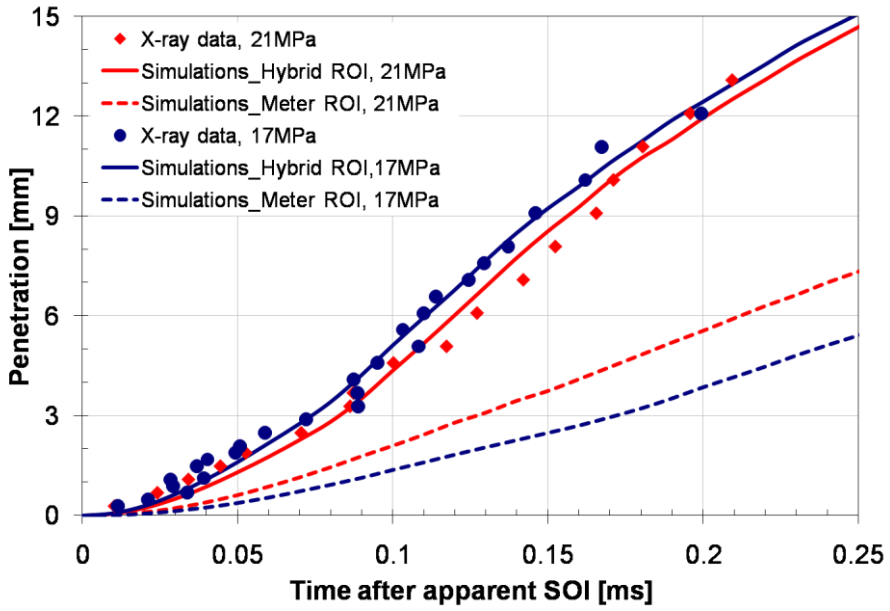

Figure 23. STAR-CD model validation against x-ray radiography data. Spray penetration for 100 mm^3/injection fuel delivery, 30 bar ambient pressure, oil rail pressures of 17 and 21 MPa versus time.

Figure 23 presents the measured and predicted liquid penetration lengths plotted versus time for oil rail pressures of 17 and 21 MPa. The scale is adjusted so that zero is the instant when the first amount of fuel is visible for each spray. There are several observations from this figure. Up to 0.1 ms, penetration is slow for both oil rail pressures. After this region, penetration becomes faster up to 0.2 ms and scales linearly with time. The last measured point for the 17 MPa case suggests that the spray may be entering a region where penetration scales as square root of time; however, more measurements would be necessary to verify this trend. These spray penetration characteristics are consistent with the observations of previous researchers [89].

Validation of STAR-CD simulations against penetration data is also presented in Figure 23. The differences in penetration lengths resulting from the various ROI profiles can be clearly observed. When the profile from the rate meter is used in the simulations, the predicted penetration lengths are significantly smaller than those measured in x-ray experiments. Better agreement is observed when the ROI profile from x-ray data is mated with that from the rate meter (cf. Figure 22(b)). In general there is an excellent match for both injection pressures, except for small differences observed earlier (< 0.1 ms).

For the higher rail pressure case, the penetration speed increases more gradually and continues increasing throughout the measurements. For both pressures, the maximum speeds achieved are notably lower than those achieved at similar conditions with a single-hole injector [19]. Further examination indicated that the single-hole injector with the single-fluid common rail injection system used in the cited study shows a much steeper rise in mass flow rate during the initial stage of injection than the HEUI system. This slower ramp in ROI for the HEUI system may account for the slower penetration speeds observed in the present experiments.

Another notable observation from Figure 23 is that the lower oil rail pressure has faster penetration speed than the higher oil rail pressure case. Other studies have shown opposite behavior under analogous

conditions where the lower injection pressure penetrates slower than higher injection pressure [19,90]. Causes for this may be interference from the isolation shield at higher injection pressures. Cavitation simulations performed by Som [13] showed differences in cavitation for the higher injection pressure that may lead to lower penetration for the 21 MPa case. Moreover, correlations in the literature show that the penetration scales with the square root of the difference in the injection and ambient pressures [26,89]. The ROI profiles measured with the Bosch rate meter also indicate a faster rise in mass flow for the higher oil rail pressure. Figure 24 presents the projected liquid fuel density distributions at 0.122 ms after apparent SOI for the two pressure cases. As indicated, the penetration for the 21 MPa rail pressure case is smaller than for the lower pressure case during this transient period.

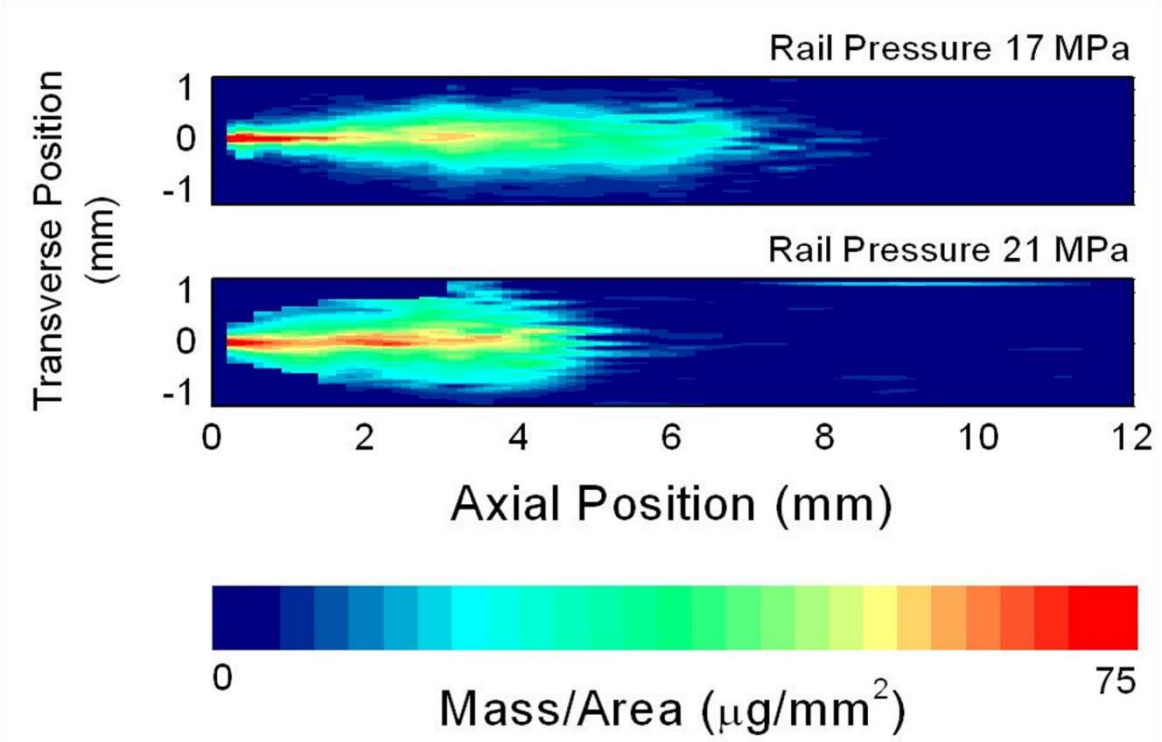

Figure 24. Spray projected density versus axial position for 100 mm^3/injection fuel delivery, 30 bar ambient pressure, at 17 and 21 MPa oil rail pressures at 0.122 ms after SOI.

A similar trend of higher penetration for the 17 MPa case than for the 21 MPa case is seen in the simulations. When only the data acquired from the rate meter is used for the ROI input, the simulations indicate that the higher oil rail pressure case yields a higher penetration. It must be recalled that the early portion of the rate profile input to the model is calculated from the x-ray data. During the early portion of the spray, the upstream conditions (such as ROI) would have effect on the results rather than the spray models themselves. Figure 22 shows higher injection rates for the 17 MPa rail pressure condition which would produce higher injection velocities. This is the reason for the faster penetration for the 17 MPa condition for both experiments and simulations.

Previous researchers have measured diesel spray penetration, and provided correlations for penetration behavior. Payri et al. [26] reported the following correlation in the transition region:

$$S = (0.018)(\rho_a)^{-0.256}(\Delta P)^{0.516}(t)^{1.044} \tag{24}$$

S = spray penetration [mm]

ρ_a = ambient density, [μg/mm^2]

Δ P = pressure difference, [μg/ μs^2 mm]

t = time, [μs]

The coefficients were obtained through curve fitting to match penetration length in the first 15 mm region of the spray. In the short-time limit, Naber and Siebers [89] reported the following correlation:

$$S = C_v(t)\sqrt{\frac{2*(P_f - P_a)}{\rho_f}} \tag{25}$$

S = spray penetration, [mm]

$C_v(t)$ = velocity coefficient

P_f = fuel pressure, [µg/ µs^2 mm]

P_a = ambient pressure, [µg/ µs^2 mm]

ρ_f = fuel density, [µg/mm^2]

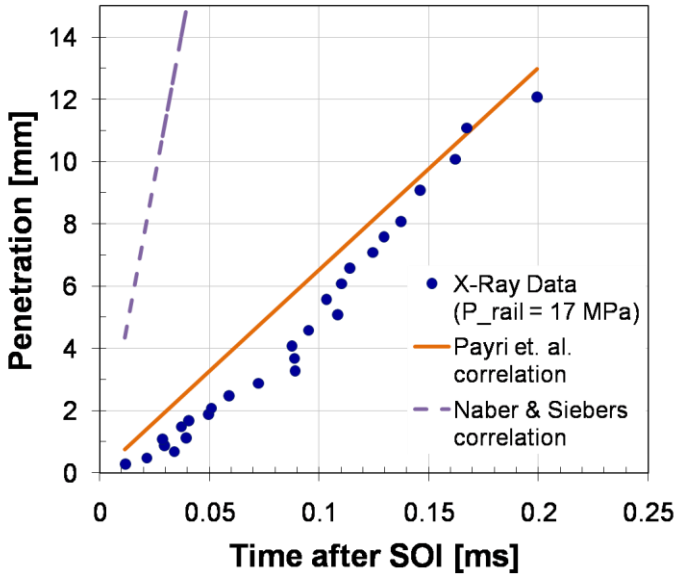

Figure 25. Comparison of x-ray data at 17 MPa oil rail pressure with penetration correlations by Payri [26] and Naber & Siebers [89]

Figure 25 presents the x-ray data for rail pressure of 17 MPa and the above penetration correlations. For our case C_v was not measured. Extensive cavitation simulations [13] yielded C_v=0.85, which is comparable to typical values for diesel injection nozzles. Even if a smaller value of C_v were used, Figure 25 indicates that the Naber and Siebers correlation predicts much higher penetration than the current data. This can be attributed to the fact that the initial gradient in the measured injection rate upon which the Naber and Siebers correlation is based is much higher than that in the current experiments. This yields high injection velocities earlier in the spray event, and hence faster penetration. The penetration based on the Payri et al. [26] correlation is much closer to that obtained from the present x-ray data. It is important to note that this correlation was derived using a multi-hole nozzle, while Naber and Siebers used a single-hole nozzle. A closer comparison of the injection rates used by Payri et. al. [26] and those used in the present study (cf. Figure 21) shows that the injection rates are close to each other. However, the gradient in the rate of injection in Payri et. al. experiments was higher than that in the current experiments, resulting in a slight overprediction by the Payri et. al. correlation.

For the 17 MPa case (cf. Figure 23), downstream of x = 12 mm, simulations exhibit the long-time limit behavior [89] with the penetration length scaling with the square root of time. However, for the 21 MPa case this transition occurs at x ≈ 14mm. Naber and Siebers [89] used a characteristic length (x^+) for this transition region, such that the penetration varies linearly with time upstream of this point (x^+), and as square root of time downstream of this point. They used the following equation for the characteristic length:

$$x^{+} = \frac{d}{\alpha \tan\left(\theta/2\right)}\sqrt{\frac{\rho_f}{\rho_a}} \tag{26}$$

x^+ = characteristic length, [mm]

d = effective nozzle diameter, [mm]

α = experimentally-derived constant (0.66)

θ = dispersion angle

ρ_f = fuel density, [μg/mm^2]

ρ_a = ambient density, [μg/mm^2]

An effective nozzle diameter of 160 μm was assumed for the current 169 μm orifice, based on about a 0.4% reduction in exit fluid flow area due to cavitation structures [13], and α was assumed to be 0.66 [89]. Optical cone angle was calculated as:

$$\tan\left(\theta/2\right) = 0.31\left(\frac{\rho_a}{\rho_f}\right)^{0.19} \tag{27}$$

θ = dispersion angle

ρ_a = ambient density, [μg/mm^2]

ρ_f = fuel density, [μg/mm^2]

A value of about 13 mm was obtained for both the rail pressures, which is in good agreement with the value predicted by present simulations.

4.3 Fuel Distribution

A unique capability of x-ray radiography is the ability to obtain the liquid mass distribution in the spray. Figure 26 presents a typical projected mass density profile in the transverse direction, obtained from x-ray measurements, at an axial position of 0.283 mm from the nozzle and 0.1 ms after SOI for the 21 MPa rail pressure case. The black rectangle at the bottom of the figure is provided to indicate the injector nozzle size (169 µm diameter). The mass density profile shows a Gaussian distribution even very near the nozzle. Studies using single-hole common rail injectors have observed that close to the nozzle, the mass distribution has a more square shape and develops to Gaussian distributions at further downstream locations [65].

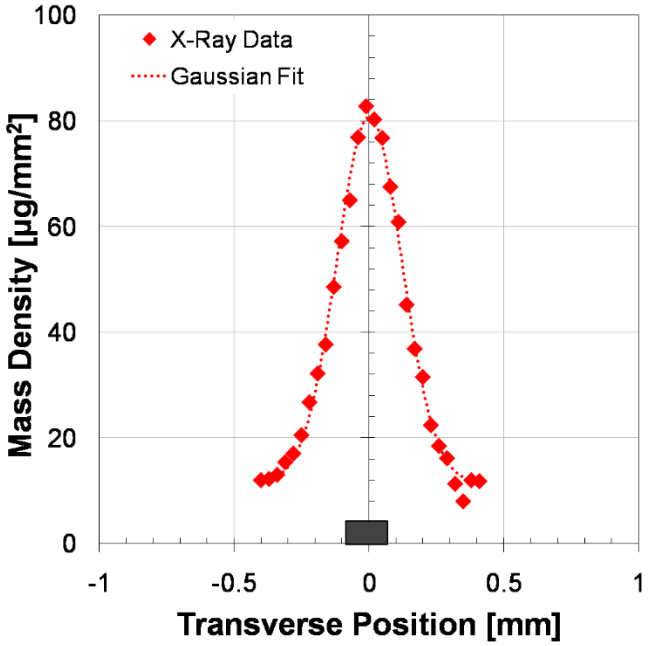

Figure 26. Transverse mass distribution profile at axial position = 0.283 mm and 0.1 ms after SOI for the 21 MPa oil rail pressure case.

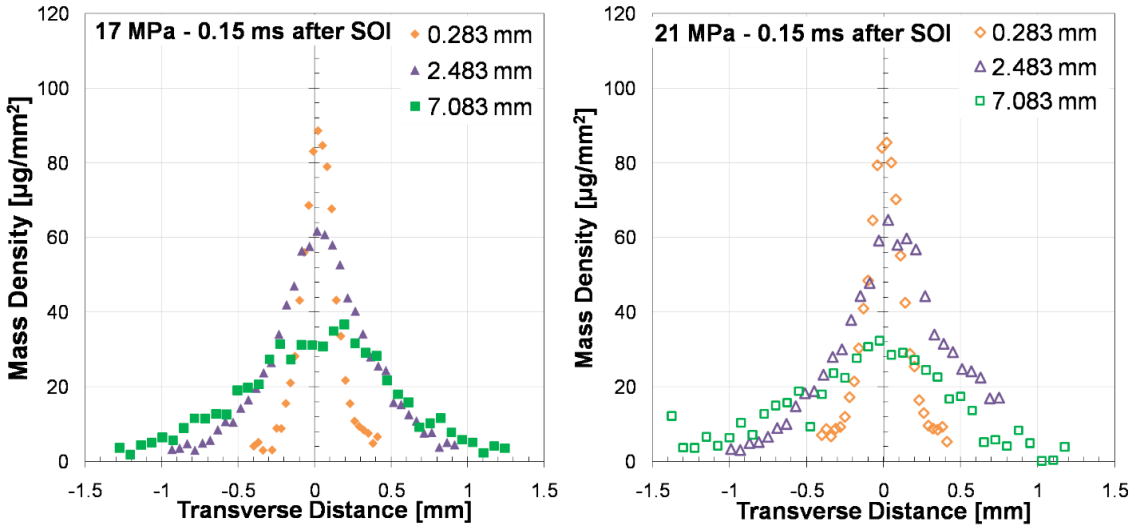

(a)

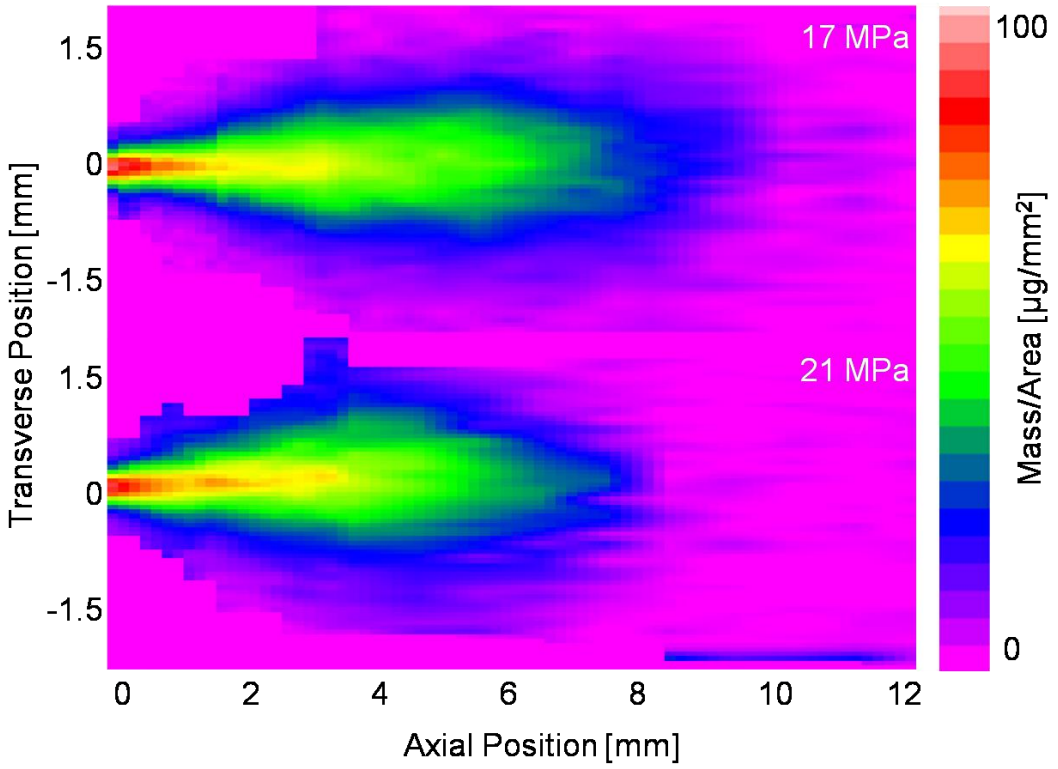

(b)

Figure 27. (a) Transverse mass distributions at 0.15 ms after SOI for 17 and 21 MPa oil rail pressures plotted at axial positions of 0.183 mm, 2.083 mm, and 7.083 mm from the nozzle (b) Full field spray projected density contours at 0.15 ms after SOI for oil rail pressures of 17 and 21 MPa

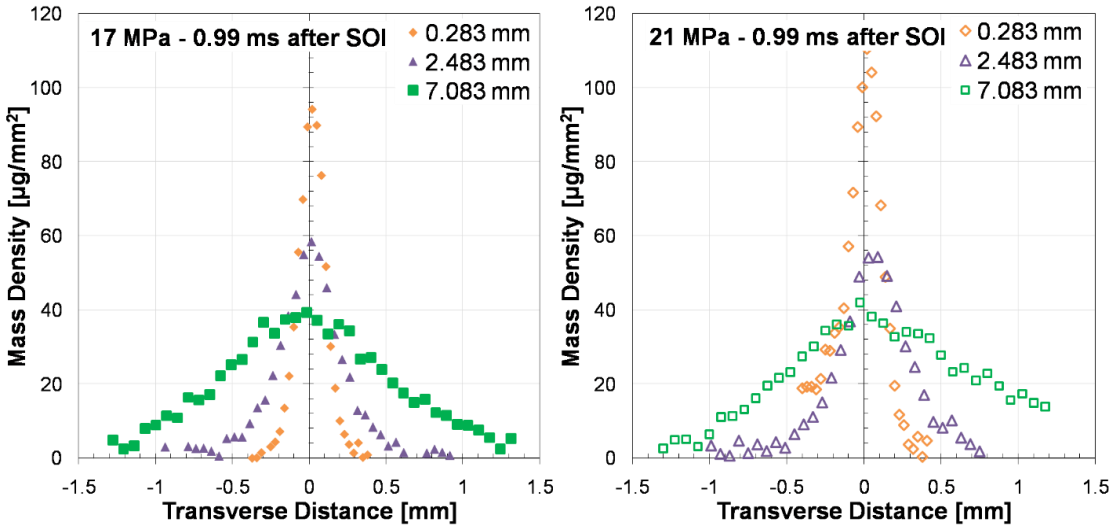

(a)

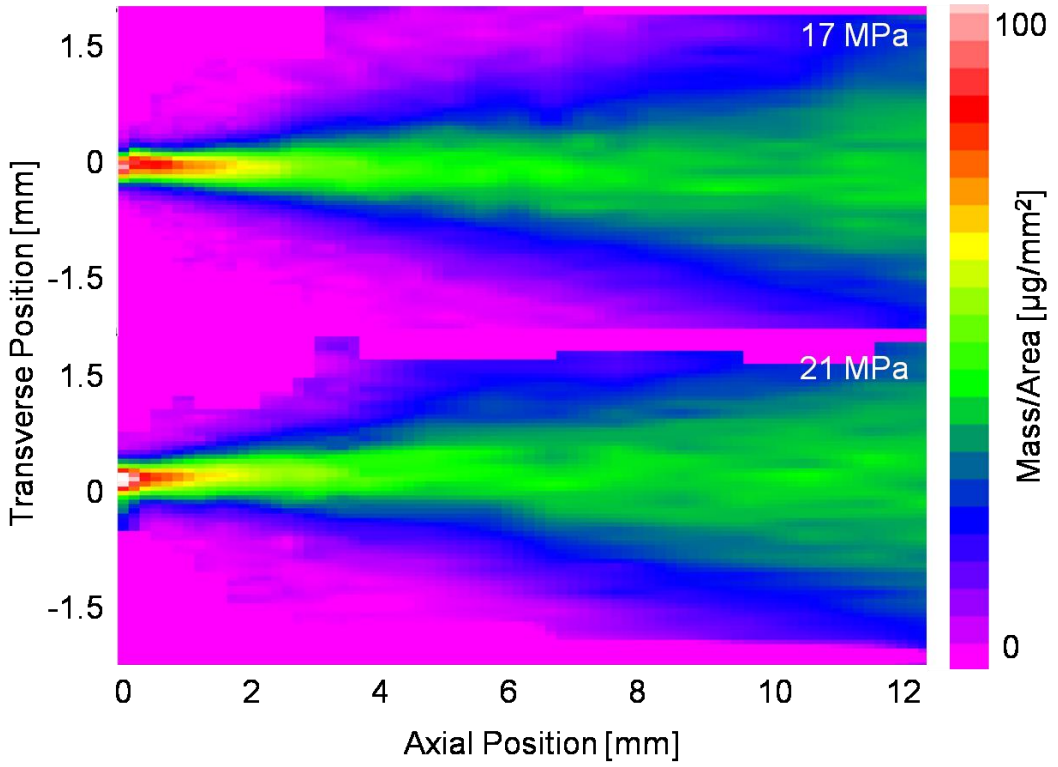

(b)

Figure 28. (a) Transverse mass distribution as at 0.99 ms after SOI for 17 and 21 MPa oil rail pressures plotted at axial positions of 0.283 mm, 2.083 mm, and 7.083 mm from the nozzle (b) Full field spray projected density contours position at 0.99 ms after SOI for oil rail pressures of 17 and 21 MPa

Figures 27 and 28 present mass distributions for the two pressure cases at 0.15 and 0.99 ms after SOI at various axial locations along the spray. Projected mass density contour plots are also shown for visualizing the spray at these times. At 0.15 ms after SOI, the two pressure cases exhibit similar mass distributions at the various axial locations. As can be expected, closer to the nozzle the projected density is significantly higher near the center of the spray, and then spreads out at downstream locations. Both the peak values and the width of the distributions at 0.15 ms after SOI are quite similar, with mass density peaks around 90 $\mu g/mm^2$ at the farthest upstream axial location. Later in the spray event, i.e., at 0.99 ms after SOI (cf. Figure 28), there are more noticeable differences between the two pressure cases at 0.283mm from the nozzle. However, further downstream, 2.483 mm and 7.083 mm from the nozzle, the distributions appear to be similar for the two rail pressures. Overall, for both times after SOI, the 17 MPa rail pressure spray exhibits a nearly symmetric distribution, while some asymmetry is observed for the 21 MPa rail pressure case. Also, the peak mass density for the 21 MPa spray is approximately 15% higher than that of the 17 MPa spray.

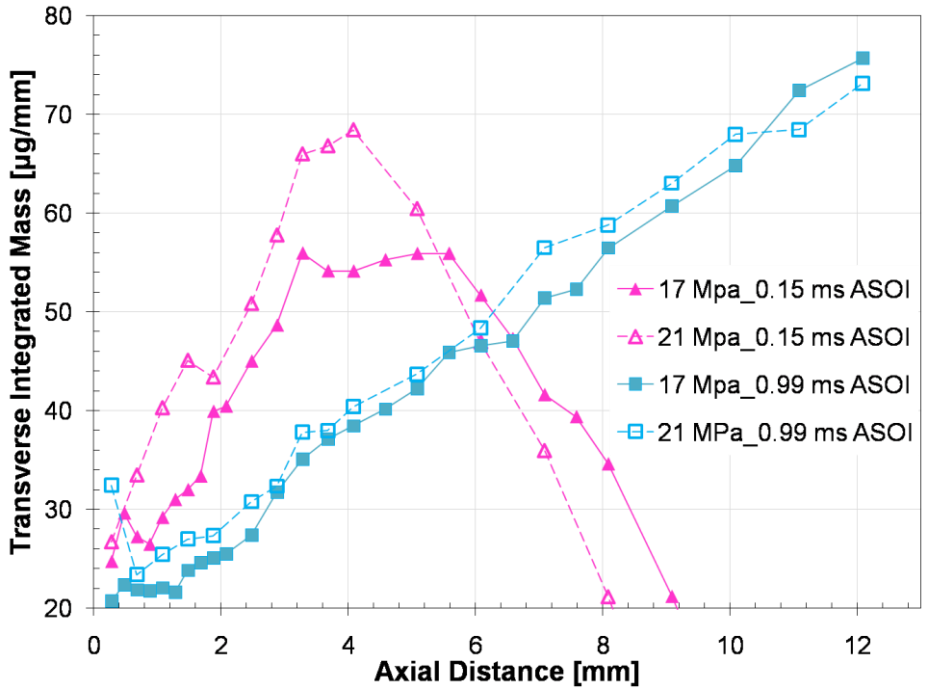

(a)

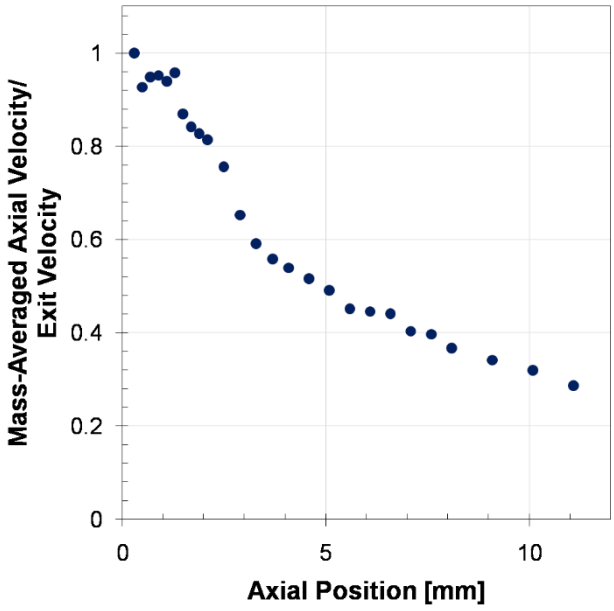

(b)

Figure 29. (a) Transverse Integrated Mass (TIM) versus axial position at 0.15 and 0.99 ms after SOI for 17 and 21 MPa oil rail pressures. (b) Trend in mass-averaged axial velocity versus axial position at 0.99 ms ASOI for 17 MPa oil rail pressure.

Integrating the mass distribution in the transverse direction results in a quantity called the transverse integrated mass (TIM) at any axial location and time and axial location. The calculated TIM from the x-ray data is shown in Figure 29 along the axial location at 0.15 ms and 0.99 ms after SOI for 17 and 21 MPa oil rail pressures. At 0.15 ms after SOI, the injection event is still in a transient stage and has not reached the end of the measurement domain, which is also indicated in Figure 28(b). Consequently, TIM increases with distance from the nozzle and then returns to zero. At 0.99 ms after SOI, TIM continuously increases with axial position along the axial location. This can be explained using the control volume analysis reported in previous work [19,65], which obtained the mass-averaged axial velocity of the spray at any axial location using the following equation:

$$V_{ma}(x_o,t) = \frac{\dot{m}_{cv}(x > x_o, t)}{TIM(x_o,t)} \tag{28}$$

V_{ma} = mass-average axial velocity, [mm/ms]

$\dot{m}_{cv}$ = mass flow rate across a cross-section, [µg/ms]

TIM = transverse integrated mass, [µg/mm]

x_0 = axial location of cross section, [mm]

t = time, [ms]

Using this information, the mass-averaged axial velocity at any location normalized by the corresponding value at x_o can be determined using the equation:

$$\frac{V_{ma}(x = x_0, t)}{V_{ma}(x = 0.283mm, t)} = \frac{TIM(x = 0.283mm, t)}{TIM(x = x_0, t)} \quad (29)$$

V_{ma} = mass-average axial velocity, [mm/ms]

TIM = transverse integrated mass, [µg/mm]

x_0 = axial location of cross section, [mm]

t = time, [ms]

Figure 29(b) presents the normalized axial velocity versus axial position obtained using the above equation for the 17 MPa rail pressure case at 0.99 ms after SOI. The spray velocity decays quite rapidly in the downstream direction, decreasing to half its initial value in the first 5 mm of spray.

4.4 Spray Isolation

Figure 30 presents the variation of projected spray density with respect to the axial position. As seen in Figure 30(a), the two sprays exhibit similar structures initially (i.e., 0.7 ms after SOI). The 21 MPa rail pressure case shows interesting behavior near the nozzle starting around 0.9 ms after SOI. A broadened region of the spray appears during this time lasting approximately 0.73 ms (cf. Figure 30(b)). Taking a closer look at the transverse mass distribution at the first measurement location (0.283 mm from the nozzle) at various times after SOI, a shift in mass distribution is observed as shown in Figure 30(c). At 0.7 ms after SOI (before the broadening is observed) the mass distribution is fairly symmetric. It then increases at the negative transverse locations at 0.9 ms after SOI, and increases near the positive values at 1.64 ms before it vanishes, and then the mass distribution is again even about the spray axis. This behavior suggests some hardware interference of the isolation shield with the spray of interest close to the nozzle tip.

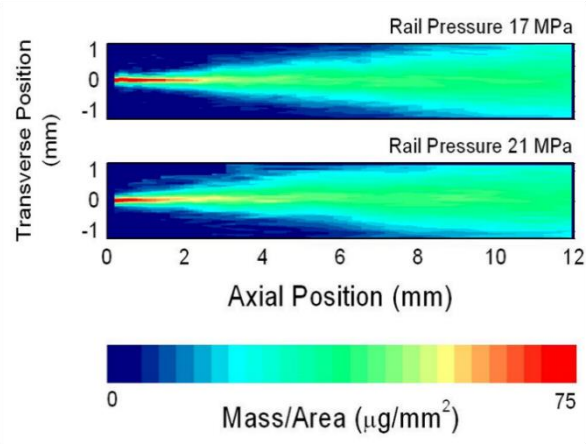

(a)

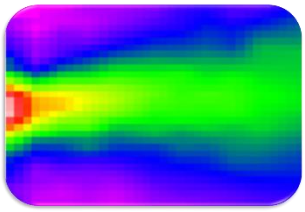

(b)

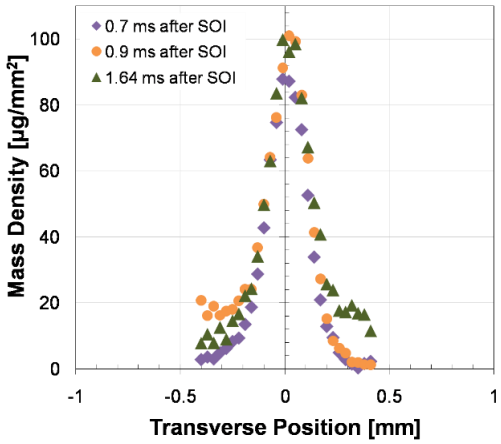

(c)

Figure 30. (a) Full field mass projected density at 0.7 ms after SOI for oil rail pressures of 17 and 21 MPa (b) Projected mass density contours in the near nozzle region at 1.15 ms after SOI for the 21 MPa rail pressure case (c) Transverse mass distribution at axial position of 0.283 mm from the nozzle at three different times after SOI for the 21 MPa rail pressure case.

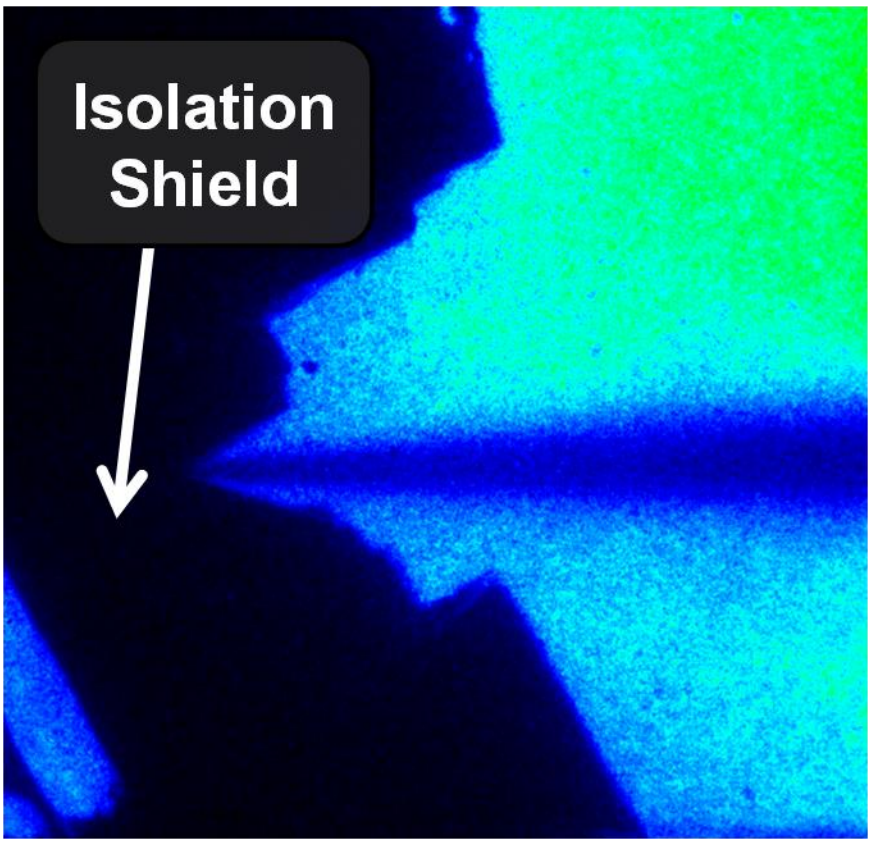

Figure 31. Optical image of injection event for oil rail pressure of 17 MPa, chamber pressure of 2 bar and fuel delivery of 100 mm^3/stroke.

Optical imaging was used to evaluate the effectiveness of the isolation shield. Visual inspection of the shield indicated that the hole-of-interest was unobstructed as seen in Figure 10 of section 2.2. Nevertheless, it was desired to see if there was any interaction between the spray and the shield itself that may explain this anomalous penetration behavior and other interference observed in the x-ray experiments. Both oil rail pressures were tested, however due to limitations imposed by the windows used for optical access, lower ambient pressure in the spray chamber was necessary. Figure 31 presents an image of an injection event for 17 MPa oil rail pressure, 2 bar chamber pressure, and a fuel delivery of

100 mm^3/stroke. Although some accumulation of mass was observed on the slanted surface of the shield below the spray, no errant interference with the spray was observed. However, future improvements to the shield design would include a more drastic slope on the angled surface.

4.5 Cone Angle

The spray cone angle is computed from x-ray measurements by measuring the FWHM of Gaussian fits to the transverse mass distributions at each axial location and time step in the measurements. The cone angle is then calculated from a linear fit to the FWHM locations, and plotted as a function of time in Figure 32(a). If the transverse mass distribution were perfectly axisymmetric and Gaussian, this cone angle value would define a volume containing half the total mass in the spray. By definition, using the FWHM to compute cone angle, x-ray radiography focuses on the core of the spray, while optical techniques focus on the spray periphery. Thus, the x-ray cone angle is expected to be smaller than the optical cone angle [23].

Although there is not a noticeable difference in the cone angle values between the two rail pressures, the cone angle tends to be higher for the 21 MPa rail pressure case than that for the 17 MPa case, with average quasi-steady state values of 10.5° and 9.9° respectively. Figure 32(b) presents the cone angle versus time in the initial transient part of the spray along with a polynomial fit to the data. The spray cone angle for the 21 MPa rail pressure case is consistently larger compared to that of the lower pressure case in this transient region as well. This is consistent with the projected density results discussed earlier in the context of Figure 24, which presented the projected density for both sprays during the transient period of injection. These cone angle values are higher than those observed for single-hole common rail injectors under similar conditions [65].

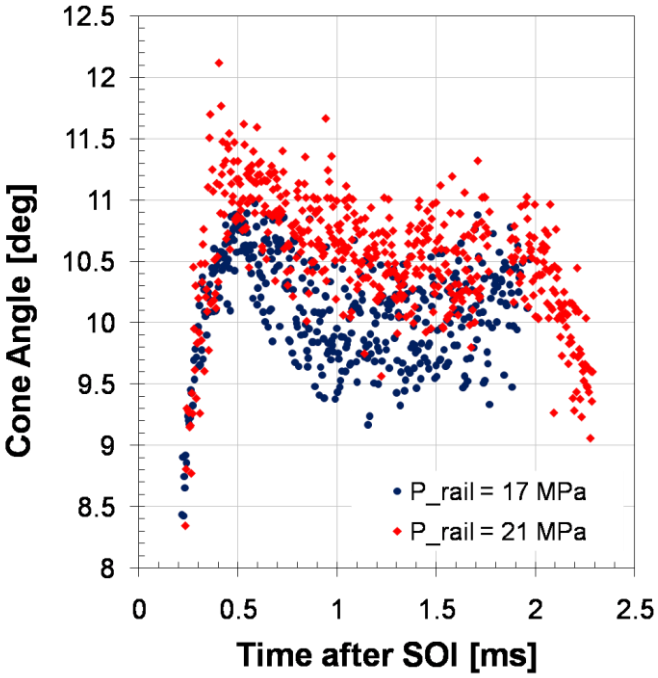

(a)

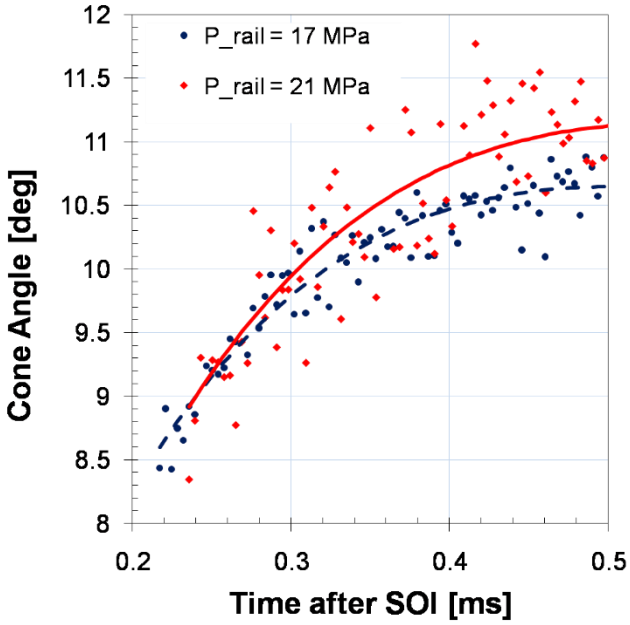

(b)

Figure 32. Measured cone angle versus time for 17 and 21 MPa oil rail pressures (b) Zoomed cone angle versus time during the initial transition period.

4.6 Summary

In this portion of the study, x-ray radiography was used to study fuel spray from a full-production diesel HEUI at engine-like ambient density for two injection pressures. Fuel penetration, spray mass distribution, mass-averaged axial velocity, and cone angle were reported.

Rate of injection studies were completed on a Bosch-type rate meter to further understand the characteristics of the injection system. The ROI profile obtained with the rate meter (all 6 sprays combined) is compared to that of the x-ray measurements (one of six sprays) during the first stages of injection. A significantly slower rise is seen in the rate meter measurements than that calculated from the x-ray measurements. This slower transient ROI yielded underpredictions in the simulations while a hybrid profile generated using the x-ray-generated ROI in the initial portion produced good agreement between the simulations and experimental measurements for spray penetration. Thus, the ROI from the x-ray measurements is considered more accurate for inclusion in numerical simulations.

Several differences between the HEUI and previously-used research nozzles are noted in this work. The slow initial rise that is generated from a HEUI is notably different from the traditional top-hat type profile seen in previous studies on single-hole common rail injector. Fluid dynamics would differ greatly between a multi-hole versus single-hole nozzle which would yield differences in spray. Mass distribution at the initial portion of spray for the HEUI has a more Gaussian shape than single-hole nozzles produce.

Numerical simulations were performed using STAR-CD with validation from the x-ray data obtained in these experiments. When using the hybrid ROI profile as input to the model, simulations showed good agreement with the experimental data. Trends in mass distribution were obtained, however underprediction in the transverse mass density profiles show the need for development of more sophisticated models.

Unexpected differences occurred when comparing the sprays of different injection pressures. It would be predicted that higher injection pressure would yield higher spray penetration, however that was not the behavior observed in this study. Closer observation showed some strange expansion of the spray near the nozzle for the case of higher injection pressure. This suggests that there may have been interference from adjacent spray plumes, intimating need to improve the isolation shield. In addition, possible differences in cavitation at the higher injection pressure could lead to the lower penetration seen in experiments.

5 RESULTS – RATE OF INJECTION STUDY

In the x-ray portion of the study, details of the initial portion of the spray were explored. Through the modeling effort, it was emphasized that the initial period of the rate of injection plays a significant role on the resultant fuel spray. This chapter explores the effects of the rate of injection profile on the engine performance and emissions.

5.1 Experimental Test Matrix

For the first portion of this study, engine conditions were selected to match those used in the x-ray experiments. Therefore, the oil rail pressure was set to 21 MPa with an injection command of 100 mm^3/injection. A command of 8° BTDC is given for the start of injection in the engine experiments. The rate of injection profile was varied among the three available conditions (100%, 50%, and 0% ERS).

Building upon the knowledge obtained in the first part of the study, further experiments were performed to investigate the influences of the fuel injection rate profile. It was noted that while the commanded fuel quantity sent to the ECU was maintained constant, the fuel delivery between the three rate profiles was not consistent due to the alternate experimental setup (i.e. different equipment than intended). Therefore, a subsequent exploration of the conditions was performed while maintaining a constant fuel delivery with the same conditions otherwise (21 MPa oil rail pressure, 8° BTDC SOI) for the three injection rate shapes (100%, 50%, and 0% ERS).

In addition, studies were performed where the combustion phasing between the different rate profiles was coordinated by maintaining a constant location of 50% mass fraction burned (CA50) for constant fuel delivery and injection pressure while varying rate profile (100%, 50%, and 0% ERS). Table II outlines the test conditions used in the three phases of this study.

Table II. Experimental test matrix

	Constant Fuel Command	Constant Fuel Delivery, -8° CA ATDC SOI (Case A)	Constant Fuel Delivery and CA50 (Case B)
Engine Speed [rpm]	1500	1500	1500
Intake Pressure [bar]	1.54	1.54	1.54
Exhaust Pressure [bar]	1.39	1.39	1.39
Fuel [type]	Diesel	Diesel	Diesel
Injection ECU Command [mm^3/inj]	100	Varies	Varies
Fuel Delivery [mg/inj]	Varies	82	82
Oil Rail Pressure [bar]	210	210	210
(Commanded Injection Pressure [bar])	*(1386)*	*(1386)*	*(1386)*
Rate of Injection Profile [%]	100	100	100
	50	50	50
	0	0	0
Injection Timing [°CA ATDC]	8	8	Varies

5.2 Constant Fuel Command

5.2.1 Rate of Injection

As discussed in section 2.1, the HEUI system allows for variation of the rate of injection profile without hardware modification. Three rate shape profiles are obtainable through the CADeTWIN software and are labeled as 100%, 50%, and 0% ERS. Each of these conditions have a corresponding solenoid current that yields the different rate profiles. These rate of injection profiles were measured for specific conditions using the Bosch-type rate meter as described in section 2.3.

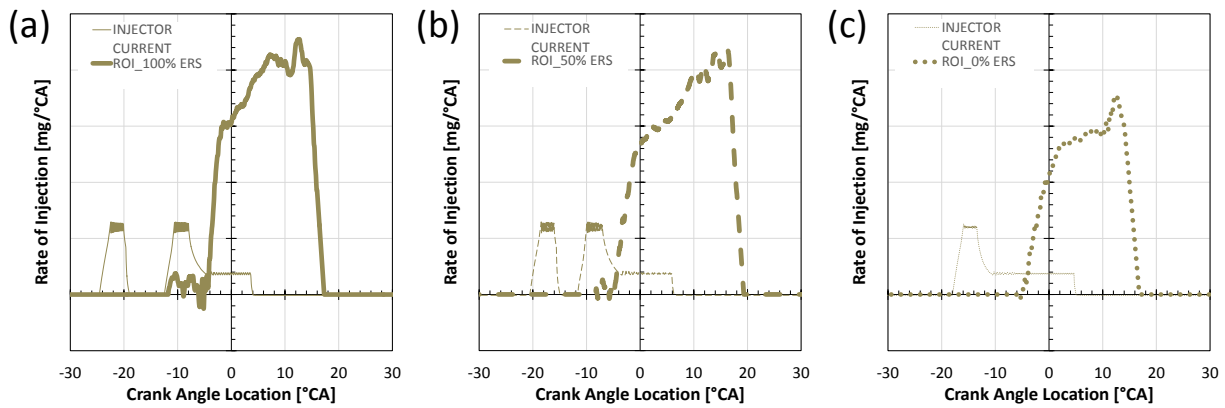

Figure 33. Injector current signals and their corresponding fuel rate of injection profiles for (a) 100%, (b) 50%, and (c) 0% ERS

General differences in structure of the three ERS profiles used in this study are shown in Figure 33. It is important to note that although there are two pulses in the injector current signal for the 100 and 50 ERS cases, this results in a single injection event. The major differences can be noted in the initial portion of injection. The 100% ERS profile shows the most rapid increase, followed by the 50% ERS, then the 0% ERS profiles. In relation to the "boot" shape profile (c.f. Figure 3) the 50% ERS profile shows the characteristics of the higher boot pressure/shorter boot duration, while the 0% ERS shows those of the lower boot pressure/longer boot duration.

Figure 34 illustrates the method that is used for aligning the fuel injection rate profile obtained from the rate meter with the engine experiment. The injector current is recorded on the high speed data acquisition system along with the cylinder pressure signal while the engine experiments are performed. It is also obtained on the same time scale as the fuel rate profile during the rate meter experiments. This injector current is used as a reference for the location of fuel ROI profile. The timing from the rate

experiments is adjusted until the injector solenoid current is coincident with that obtained during engine experiments. When selecting injection timing on the CADetWIN software, an internal map on the engine ECU is followed. Therefore using this method of coordinating the injector current signals provided a better understanding of when fuel injection actually occurred.

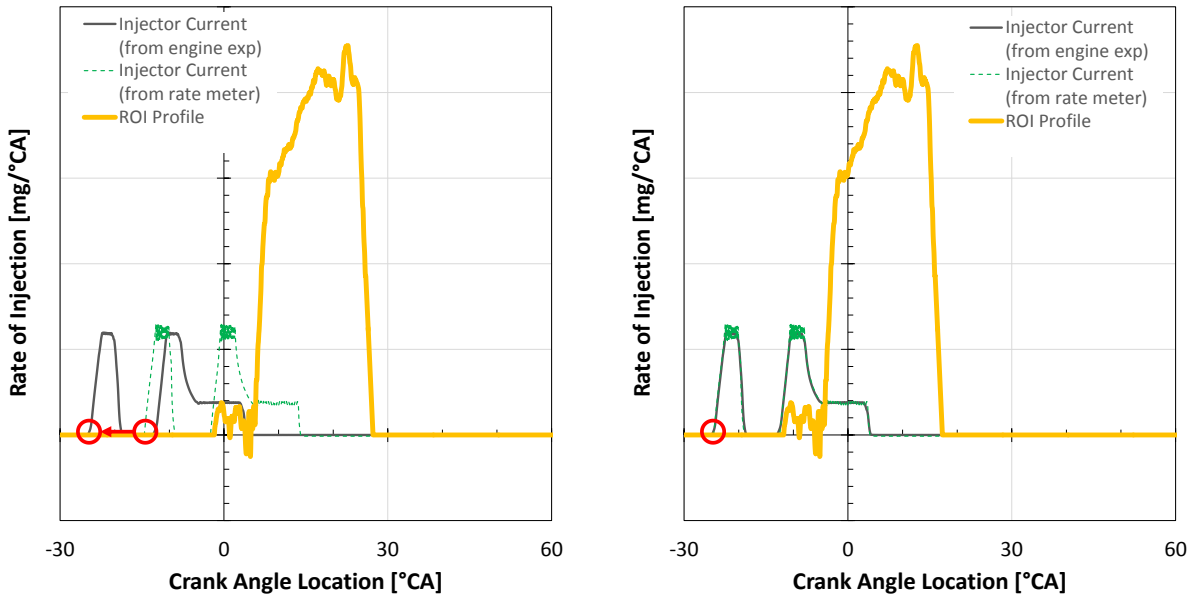

Figure 34. Reference image for aligning fuel injection rate profiles to engine experiments

Rate profiles for the injection condition of 21 MPa oil rail pressure, 100 mm^3/injection ECU command, -8° SOI are shown in Figure 35(a) for the three ERS profiles. It is noted that despite the command of constant delivery of 100 mm^3/injection, there is a variation in the total amount of fuel injected for the

three rate profiles as can be seen in Figure 35(b). There is a difference in total mass injected between the 100% (82 mg/inj) and 50% (76 mg/inj) ERS profiles, and an even larger 22% reduction in mass injected for the 0% (64 mg/inj) ERS case. The start of injection command is given at -8 degrees aTDC for all three cases and the injector solenoid current is aligned according to the procedure described above. The apparent start of fuel injection varies between the three rate profiles, with the 0% ERS trailing the other two rate shapes.

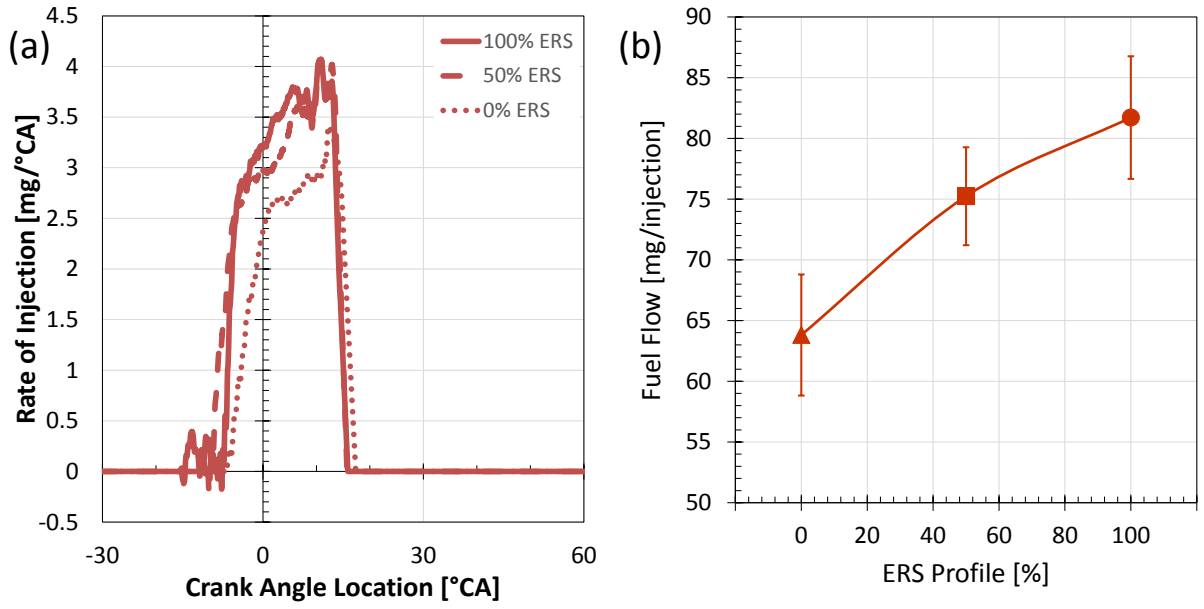

Figure 35. (a) Injection rate profiles and (b) Fuel delivery quantities for 100%, 50%, and 0% ERS for 21 MPa oil rail pressure, 100mm^3/inj command, and -8° SOI.

5.2.2 Combustion Behavior

Because of the difference in fuel injected, the following discussion will focus on the differences seen between the 100% and 50% ERS profiles. The 0% ERS information is included for reference. Cylinder pressure for the three rate profile cases is shown in Figure 36. Overall the 50% and 100% ERS profile show similar behavior in cylinder pressure while 0% ERS is lower throughout the cycle. Table III shows the peak cylinder pressure values and locations for the three rate profiles. The peak cylinder pressure is highest for the 100% ERS case, closely followed by the 50% ERS case, and then the 0% ERS case. This difference in peak cylinder pressure is likely an artifact of the lower amount of fuel injected for this condition. The locations of peak pressure however, do not follow such a pattern with the 50% ERS profile reaching a peak before the 100% ERS and 0% ERS profiles.

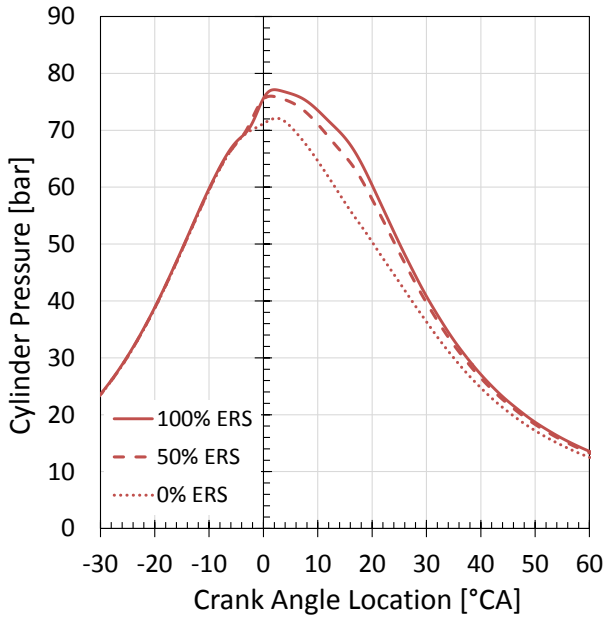

Figure 36. Cylinder pressure for the three ERS rate profiles at 21 MPa oil rail pressure, 100 mm^3/injection commanded fuel quantity, -8° aTDC SOI.

Table III. Peak pressure values and locations for three ERS rate profiles.

	100% ERS	**50% ERS**	**0% ERS**
Peak Pressure [bar]	77.1	76	72.1
Location of Peak Pressure [°CA aTDC]	2	1.4	2.4

Heat release rate along with super-imposed ROI profiles are shown for the three ERS conditions in Figure 37. The characteristic decrease in peak HRR in the premixed and diffusion regions that has been seen in other work [34,35,37,91] was observed here for the 50% ERS profile compared to 100% ERS profile. This decrease in HRR in the premixed region is attributed to the slower flow of fuel during the initial stages of injection with the intent of reducing NO_x emissions.

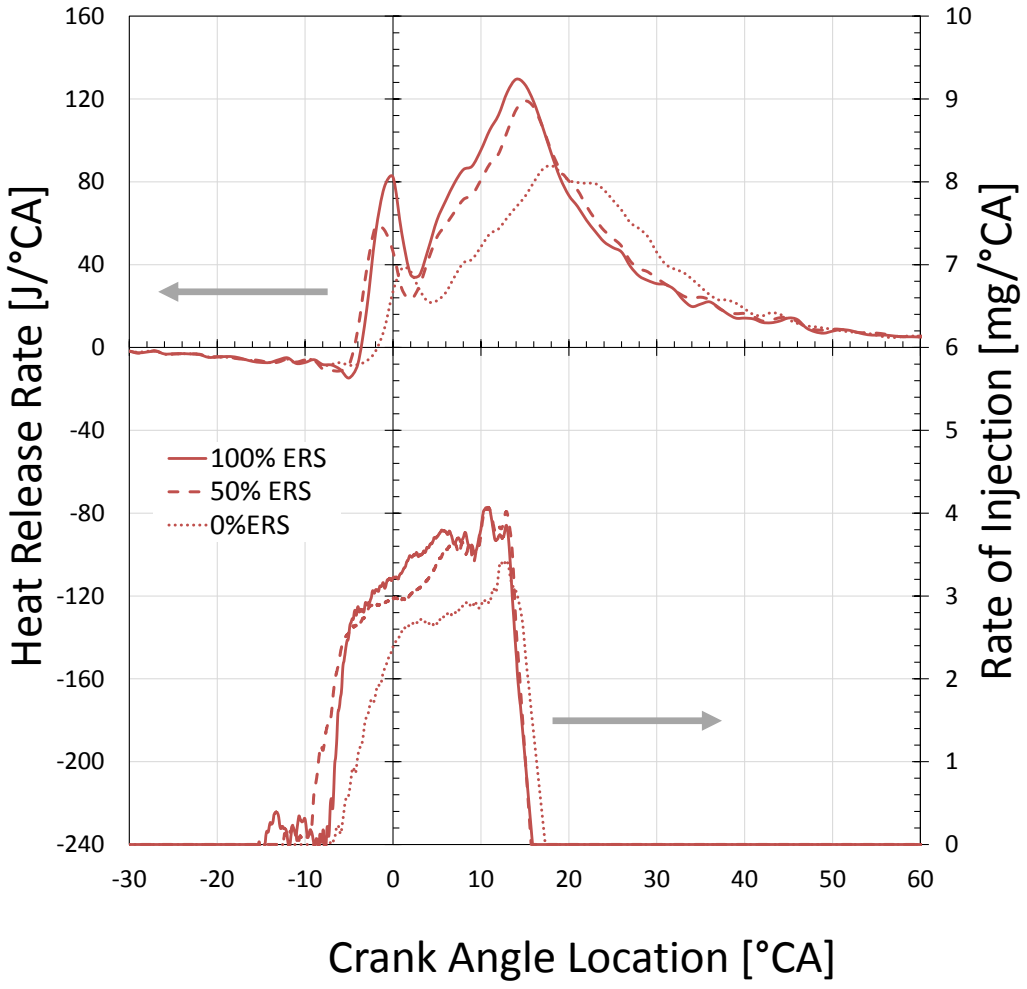

Figure 37. Heat release rate and rate of injection profiles for the three ERS conditions at 21 MPa oil rail pressure, 100 mm^3/injection commanded fuel quantity, -8° aTDC SOI.

Because of the differences in fuel injected and the resultant net heat release, it can be more useful to discuss the data in terms of percentages. Locations of mass fraction injected and burned are given in Table IV and shown graphically in Figure 38. A crank angle location is also provided for the apparent SOI, meaning the point at which the injection rate profile begins to continually rise from zero. The variation in apparent SOI is visible here with the 50% ERS profile starting nearly 2 crank angle degrees before the 100% ERS case, and 3 crank angle degrees before the 0% ERS case. The difference between a particular point and the apparent SOI is given in parenthesis to the right of the value. This gives a better understanding of

how long it takes to reach a certain point after the fuel begins injecting. Looking at these values in parenthesis (duration from apparent SOI), trends can be seen regarding the different rate profiles. As far as mass fraction injected, the time to reach these points is as expected – 100% ERS takes the shortest amount of time to reach 5% and 10% mass fraction injected, followed by 50% ERS, then 0% ERS. This is in agreement with the slower fuel flow in the initial portion of injection for the boot profiles. However, when looking at the 90% mass fraction injected, the gap decreases between the differences in duration for the boot profiles, more pronounced in the 0% ERS case. For instance, the differences between the locations of 5% mass fraction injected for 100% ERS and that of 50% ERS and 0% ERS is 1.1°CA and 2°CA, respectively. Yet for 90% mass fraction injected, the locations trail the 100% ERS case by 2.4°CA (50% ERS) and 1.1°CA (0% ERS). This shows the increase in rate of mass injected seen later in the event for the boot profiles.

While the 50% ERS had an apparent SOI and 5% mass injected that were the earliest in the cycle, 5% of the mass fraction burned is earlier for the 100% ERS case. This may indicate a slower burn due to the decrease in ROI of the fuel during the boot portion of the 50% ERS. Nonetheless, differences are not large in locations of 5% and 10% mass fraction burned for the 100% and 50% ERS cases. The 50% and 0%ERS profiles show that the duration of time between 90% mass fraction burned and apparent start of injection is nearly identical 68.0° CA and 68.2°CA, respectively.

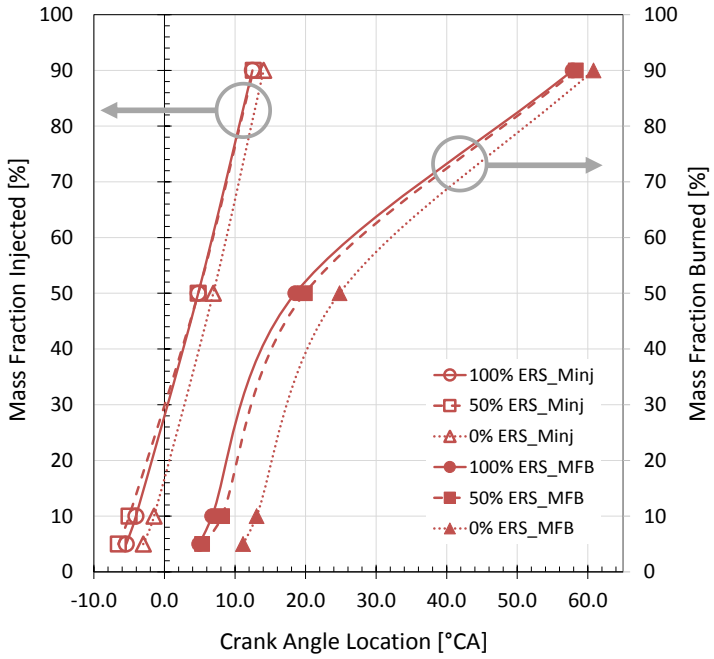

Figure 38. Locations of 5%, 10%, 50%, and 90% mass injected and mass fraction burned for all rate shapes at 21 MPa oil rail pressure, 100mm^3/inj commanded fuel quantity, -8° aTDC SOI.

Table IV. Locations of apparent SOI, mass fraction injected and burned for all rate shapes at 21 MPa oil rail pressure, 100mm^3/inj commanded fuel quantity, -8° aTDC SOI. Numbers in italics and parenthesis are the differences between that point and the apparent SOI for that condition.

Crank Angle [°CA aTDC]	**100% ERS**		**50% ERS**		**0% ERS**	
Apparent SOI	-7.6		-9.9		-7.2	
Mass Fraction Injected						
5%	-5.4	*(2.2)*	-6.5	*(3.3)*	-3.0	*(4.2)*
10%	-4.1	*(3.6)*	-5.0	*(4.9)*	-1.5	*(5.7)*
50%	4.8	*(12.4)*	4.8	*(14.6)*	6.9	*(14.1)*
90%	12.5	*(20.1)*	12.6	*(22.5)*	14.0	*(21.2)*
Mass Fraction Burned						
5%	4.9	*(12.5)*	5.3	*(15.2)*	11.1	*(18.3)*
10%	3.8	*(14.3)*	8.2	*(18.0)*	13.1	*(20.2)*
50%	18.5	*(26.1)*	19.9	*(29.7)*	24.8	*(32.0)*
90%	57.9	*(65.5)*	58.3	*(68.2)*	60.8	*(68.0)*

5.2.3 In-Cylinder Imaging

Endoscope images were taken of the combustion for the three rate shape cases. Figure 39 shows these images (top) along with calculated temperature (middle) and soot (bottom) distributions during different stages of combustion. In Figure 39(a), the 50% and 100% cases have finished the premix burn phase and are entering the diffusion burn while the 0% case is in the premix burn phase. Figure 39(b), is at 15 degrees after TDC where fuel injection is still occurring for all three cases and they are all in the diffusion burn stage. At 30 degrees after TDC (Figure 39(c)), fuel injection has ended and is after the diffusion peak of heat release for all cases. Figure 39(d) shows the combustion event at 50 degrees after TDC. Fuel injection has ended and diffusion burn is nearly complete at this crank angle location.

The temperature and soot values are calculated as described in the theory portion of the current work in section 3.6 and by Ciatti et al. [74,78]. Qualitatively it is difficult to extract significant information from the temperature distribution in the cylinder at these locations from the images. The temperature results near the start of combustion are reported quantitatively in Figure 40(a). Here it can be seen that the peak temperature is first achieved by the 100% ERS case followed by 50% and 0% ERS in succession. This agrees with the combustion traits shown through the locations of mass fraction burned in Table IV. The integral soot volume fraction is reported in Figure 40(b) towards the end of combustion. Looking at the overall combustion event, it is seen that the boot shaped ROI profiles show the penalty of increased soot emissions, with 0% ERS being the highest. This trend can clearly be seen towards the end combustion as is shown in the plot. It has been shown [12,35,37] that soot formation is primarily governed by the mixing process which is in agreement with the differences seen in the diffusion burn. Taking a look at the ROI profiles shown in Figure 37, it can be seen that the 0% ERS injection lasts longer in the cycle. This extra fuel introduced later would not have sufficient chance to oxidize and thus produces higher soot.

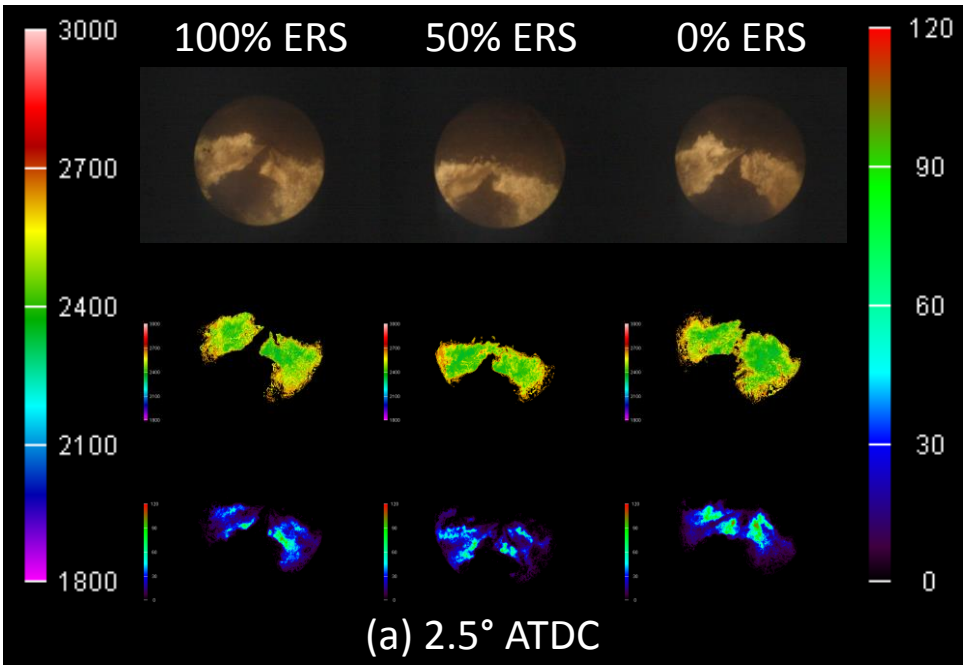

(a) 2.5° ATDC

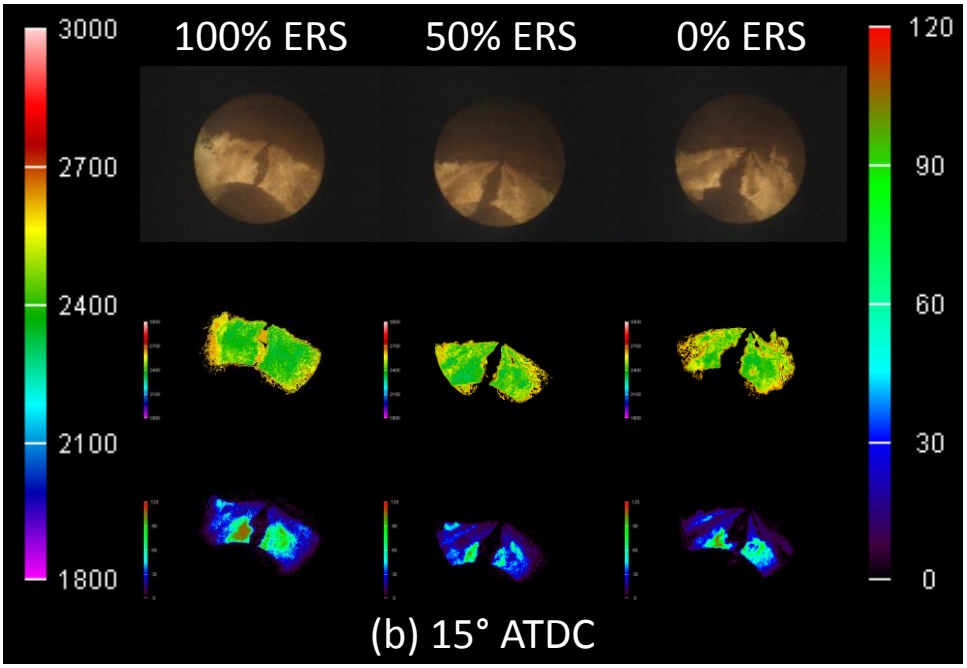

(b) 15° ATDC

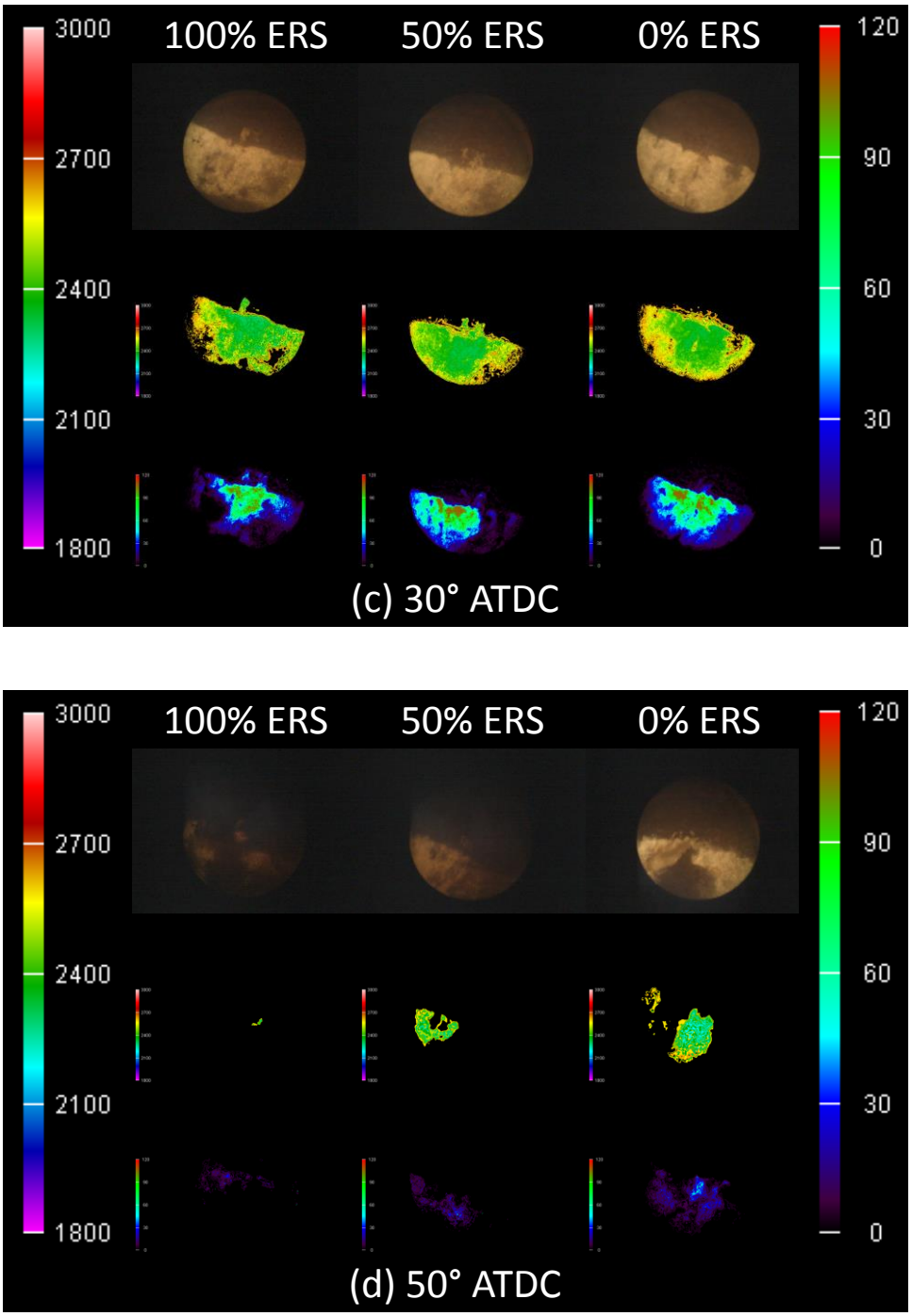

Figure 39 . Images (top), temperature contours (middle), and soot volume fraction contours (bottom) for 100%, 50%, and 0% ERS. Temperature scales is on the left in Kelvin. Soot Volume fraction scale is on the right. Images are shown at (a) 2.5°, (b) 15°, and (c) 30°, and (d) 50° after TDC.

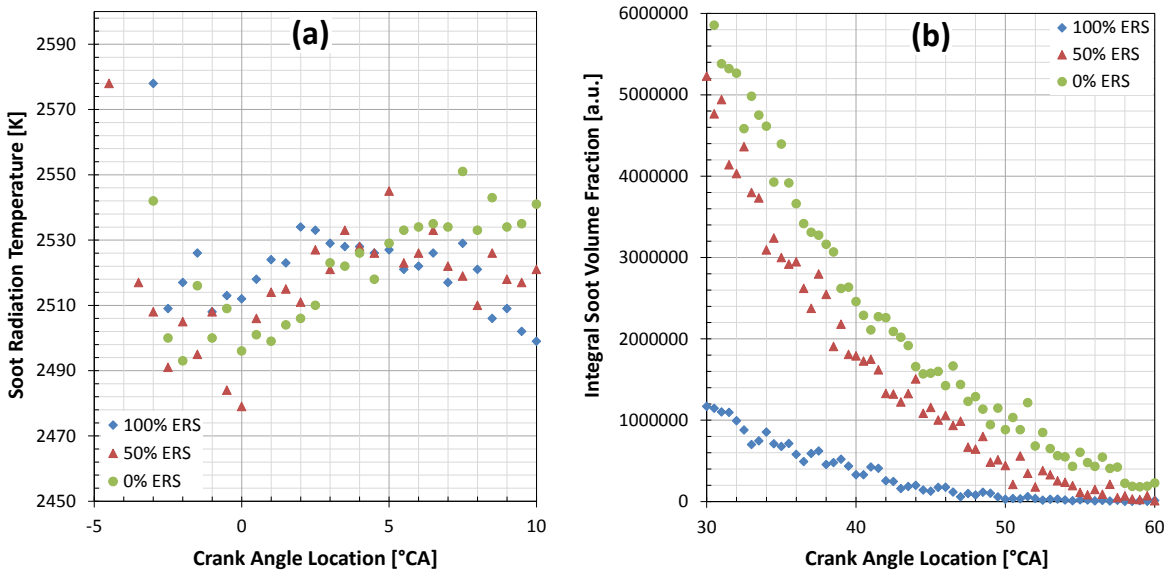

Figure 40. (a) Soot radiation temperature at the early stages of injection (b) Integral soot volume fraction towards the end of combustion.

5.3 Constant Fuel Delivery and Combustion Phasing

While the above exercise was insightful in understanding the differences between the boot shape profiles in comparison with the standard injection profile, the variation in the amount of fuel injected poses a problem for direct comparison. Therefore it was desirable to know the effect of rate profile should the fuel quantity be kept constant. The fuel quantity was kept constant by providing different fuel commands to the ECU and measuring the fuel output using the AVL fuel scale as described in section 2.4.5. Although there is some variation, the fuel quantity was kept as close as possible using this method. Subsequent study was performed by coordinating combustion phasing between the constant quantity injections while maintaining the location of 50% mass fraction burned constant by changing the injection

timing for the rate shaping conditions. For simplicity, the case of -8° CA aTDC SOI timing will be referred to as case A and plots will be shown on the left in purple. The case of constant CA50 will be referred to as case B and plots will be shown on the right in green.

5.3.1 Rate of Injection

Rate profiles were not measured for each specific command that was necessary to obtain constant fuel delivery. Therefore, ROI profiles were constructed by interpolation between measured quantities from ECU commands to correspond with the new ECU commands used. An illustration of a calculated ROI profile from two measured profile is shown in Figure 41. Injector solenoid current location was still used as a baseline for synchronizing the rate profile data with the high speed indicating data.

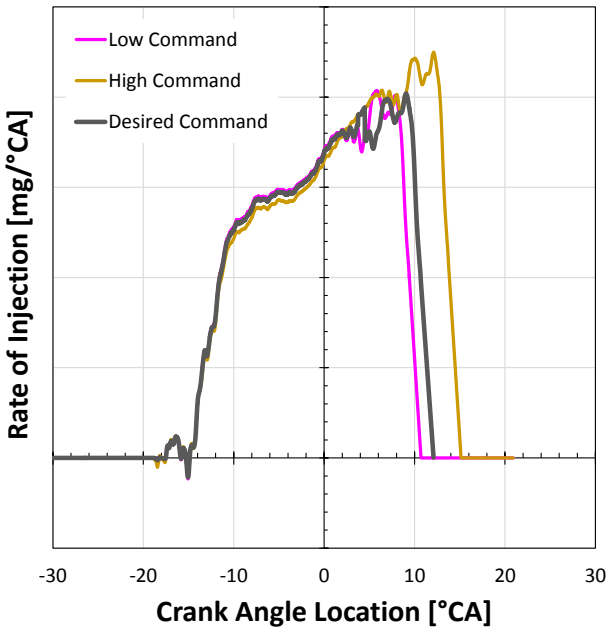

Figure 41. Sample interpolated injection rate profile.

Constructed rate profiles that are synchronized with the engine data for these studies are shown in Figure 42. There are significant differences in the shapes of the rate profiles throughout the injection. The initial portion of the 50% and 0% ERS profiles show a more gradual ascent. The 50% and 100% ERS profile reach the same rate of injection after the transitional period of injection, while the 0% ERS reaches a value approximately 14% lower. This trend is also seen with the peak rate of injection where the 100% and 50% ERS profiles match and the 0% ERS profile is lower. However, the difference here is not quite as drastic with a difference of 7% between the peak values. In order to obtain the same amount of fuel injected, the duration of injection varies between the three cases. Figure 42(c) shows the actual fuel delivery achieved in these cases and it can be seen that they are quite close.

It can be seen that there is variance in apparent SOI amongst the three rate profiles for both studies as is shown. For case A (Figure 42(a)), the 50% ERS injection begins first followed by the 100% ERS and finally the 0% ERS profile. Fuel injection for the 100% and 50% ERS injections ends near the same time, while the 0% ERS injection continues for an additional 8° CA in order to inject an equal amount of fuel. In Figure 42(b) the SOI timing is adjusted to align the location of CA50 for the three rate profile cases. This results in an earliest apparent SOI for the 0% ERS injection, followed by the 50%, and finally the 100% ERS injection. The end of injection for the three profiles is nearly aligned.

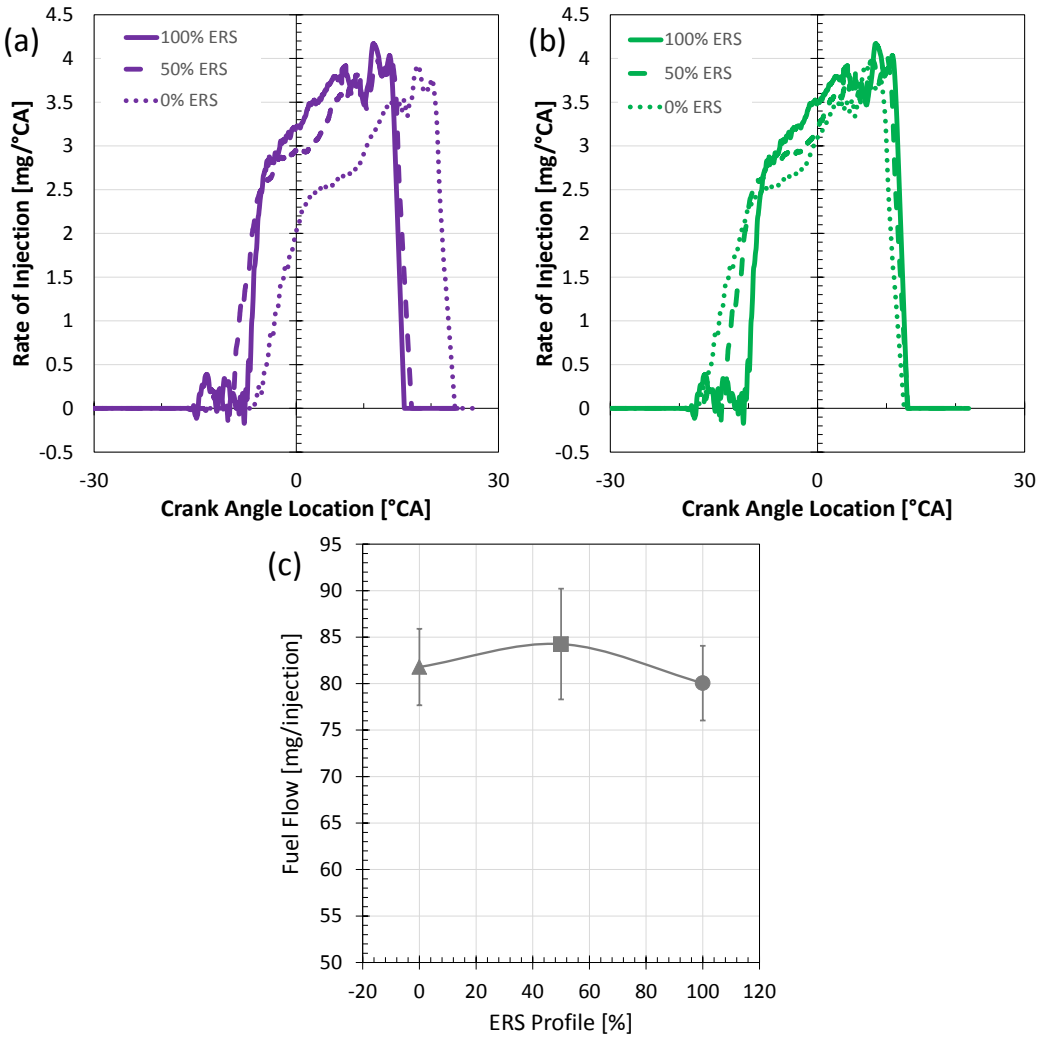

Figure 42. Fuel injection rate profiles for 21 MPa oil rail pressure, constant fuel delivery, at 100%, 50%, and 0% ERS (a) at -8°CA aTDC SOI and (b) constant CA50 (varied SOI). (c) Fuel delivery for all cases of rate shaping (error bars represent 1 standard deviation)

5.3.2 Combustion Analysis

Cylinder pressure is shown in Figure 43 and peak pressure information is shown in Table V. Overall peak cylinder pressures are higher for case B. The injection timing is earlier for these trials, thus giving more time for the fuel to mix and yielding a higher pressure peak. For both cases A and B the peak pressures for 100% and 50% ERS are close to each other with a peak pressure for 0% ERS that is lower in case A and higher in case B. It can be seen that there is more difference in the expansion stroke for case A amongst the injection rate cases than is seen in case B with 0% ERS injection being quite lower than the 50% and 100% ERS injections. In case B, the start of combustion for the 0% ERS leads, followed by the 50% and 100% ERS profiles while the pressure curve is coincident after 20° CA.

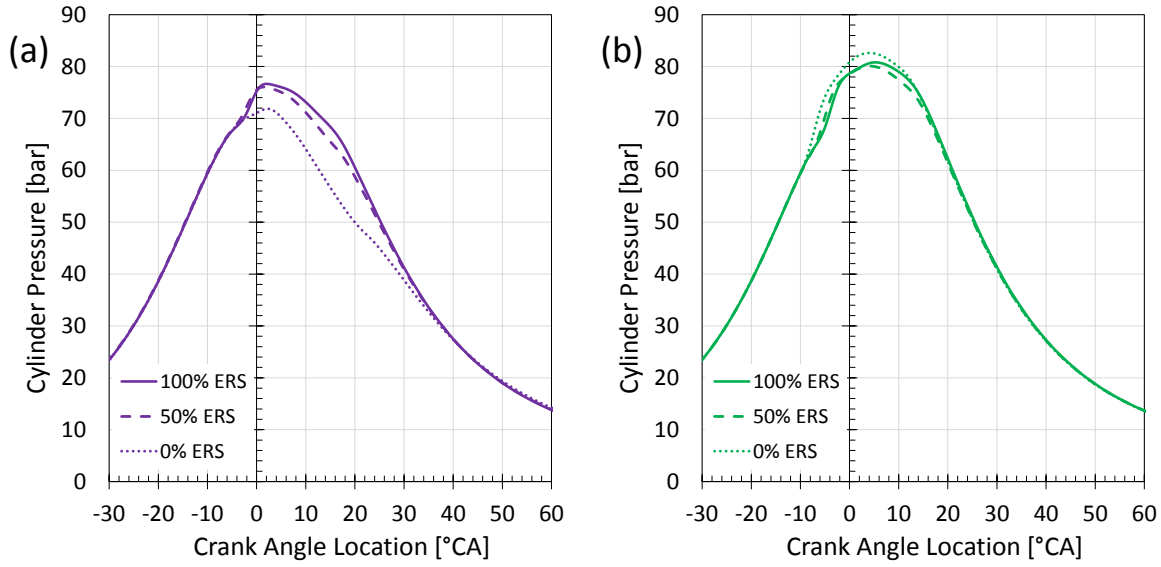

Figure 43. Cylinder pressure for the case of 21 MPa oil rail pressure, constant fuel delivery, and three rate profiles at (a) -8° CA aTDC SOI and (b) constant CA50.

Table V.Peak pressure values and locations for three ERS rate profiles at -8°CA aTDC SOI (Case A) and constant CA50 (case B).

CASE A: -8° CA aTDC SOI	100% ERS	50% ERS	0% ERS
Peak Pressure [bar]	76.7	76.0	71.8
Location of Peak Pressure [°CA aTDC]	2.0	1.4	2.3

CASE B: Constant CA 50	100% ERS	50% ERS	0% ERS
Peak Pressure [bar]	80.8	80.1	82.6
Location of Peak Pressure [°CA aTDC]	5.2	4.0	4.1

Heat Release Rate (HRR) along with ROI profile are shown in Figure 44. Integrating these curves and normalizing will yield the mass fraction burned and injected as shown in Figure 45. Overall larger differences are seen when the SOI command is constant (case A) than when CA50 is constant (case B).

For case A [-8° CA aTDC SOI - Figure 44(a) and Figure 45(a)], there is a large variation in the premix peak with 100% ERS having the highest value, followed by 50% ERS, then 0% ERS. Taking a look at the corresponding ROI curves, there is much less fuel injected during this early stage for the 0% ROI injection than for the other two profiles which could yield a lower premix peak. Although the amount of fuel injected is comparable at this stage for the 50% and 100% ERS injections, the 100% ERS gives a higher premix peak. There is higher rate of injection pressure change for the 100% ERS which could result in better mixing and thus higher heat release in the premix burn. There is good agreement in phasing and peak of the diffusion burn for 50% and 100% ERS injections while the 0% ERS injection is delayed. Overall the 0% ERS injection introduces fuel into the cylinder later in the cycle, resulting in the later diffusion burn.

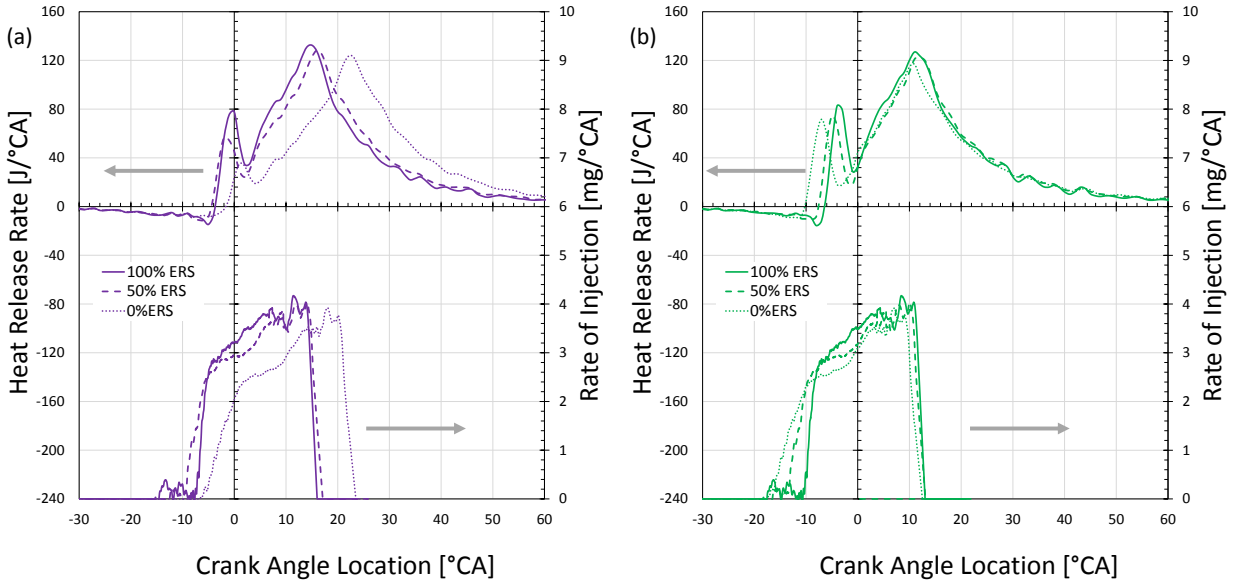

Figure 44. Heat release rate and rate of injection profiles for the three ERS conditions at 21 MPa oil rail pressure, constant fuel delivery, and three rate profiles at (a) -8° CA aTDC SOI and (b) constant CA50.

When maintaining constant CA50 [case B – Figure 44(b) and Figure 45(b)], the injection is advanced in the boot profiles. The premix burn peak decreases as the boot injection pressure decreases (100% ERS high, 50% ERS medium, 0% ERS low) but does not show the large differences seen in case A. The fuel has a longer time to mix in the cylinder before combustion begins which compensates for the lower rise in injection pressure. The peak in diffusion burn agrees well among the three injection rate conditions. The duration of the diffusion burn is longest for the 0% ERS injection and shortest for the 100% ERS injection.

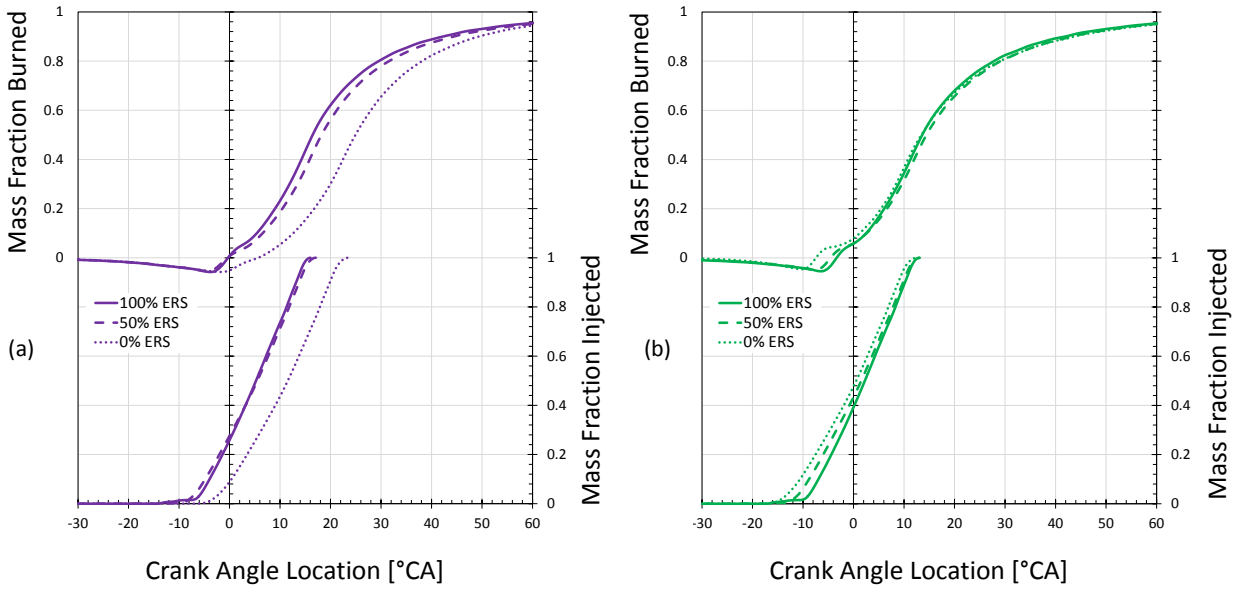

Figure 45. Mass fraction burned and Mass fraction injected for the three ERS conditions at 21 MPa oil rail pressure, constant fuel delivery, and three rate profiles at (a) -8° CA aTDC SOI and (b) constant CA50.

Locations of 5%, 10%, 50%, and 90% mass fraction burned and injected are shown graphically in Figure 46. Tables VI and VII show these values along with the location of apparent SOI. The numbers in italics and parenthesis show the value of that interval between that location and the apparent start of injection. Ignition delay (ID) as discussed here is defined as the time from apparent SOI to that of CA5.

For both studies, the trend in ignition delay is the same where 100% ERS has the shortest ID and 0% ERS has the longest ID. There are larger differences in these values for case A (12.7° - 19.3°) compared to case B (12.1° - 16.7°). Figure 45 shows that more mass is injected before the piston has reached TDC for case B than for case A. During this stage in the cycle, temperature and pressure are rising which is more conducive to ignition and a shorter delay.

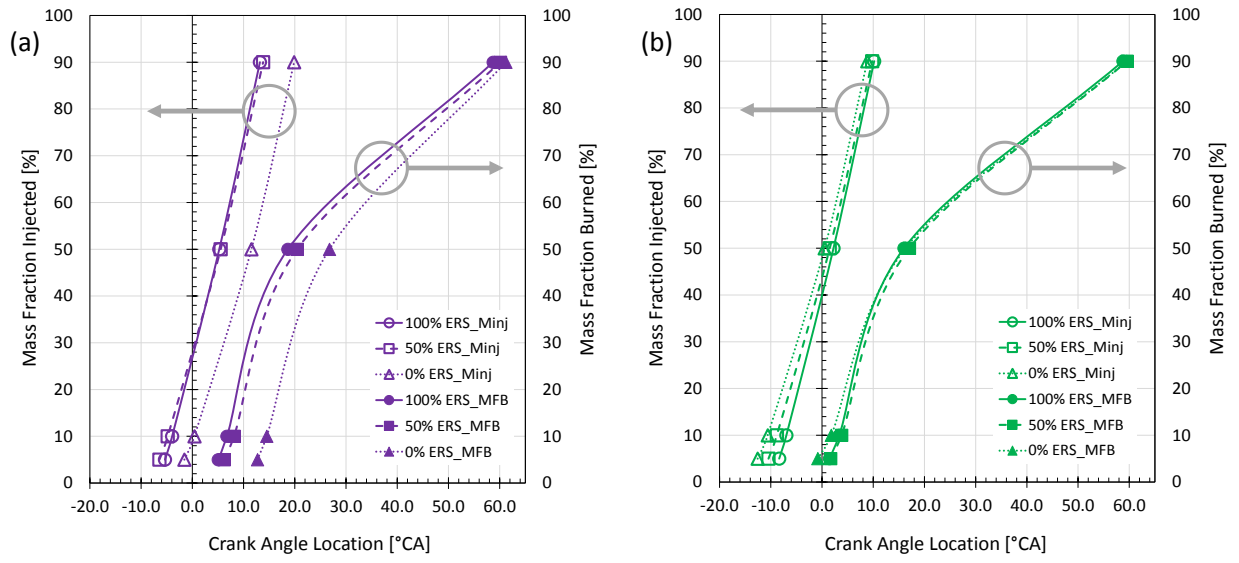

Figure 46. Locations of 5%, 10%, 50%, and 90% mass fraction burned and mass fraction injected burned for all rate shapes at 21 MPa oil rail pressure, constant fuel quantity at (a) -8° CA aTDC SOI and (b) constant CA50.

The mass fraction injected and mass fraction burned values reported in Table VI show similar trends to those reported in the original experiment (cf. Table IV). Although the fuel quantity between the two studies differs, the initial part of the combustion event should be similar. The soot radiation temperature shown in Figure 40 provide further evidence of combustion starting earliest for the 100% ERS condition, followed by the 50% ERS injection, and lastly the 0% ERS profile.

Table VI. Locations of apparent SOI, mass fraction injected and burned for all rate shapes at 21 MPa oil rail pressure, constant fuel quantity, and -8° CA aTDC SOI. Numbers in italics and parentheses are the differences between that point and the apparent SOI for that condition

Crank Angle [°CA aTDC]	**100% ERS**		**50% ERS**		**0% ERS**	
Apparent SOI	-7.6		-9.9		-6.6	
Mass Fraction Injected						
5%	-5.4	*(2.3)*	-6.4	*(3.4)*	-1.6	*(5.0)*
10%	-3.9	*(3.7)*	-4.8	*(5.1)*	0.4	*(7.0)*
50%	5.3	*(12.9)*	5.5	*(15.4)*	11.5	*(18.1)*
90%	13.2	*(20.8)*	13.8	*(23.7)*	19.9	*(26.4)*
Mass Fraction Burned						
5%	5.1	*(12.7)*	6.2	*(16.1)*	12.7	*(19.3)*
10%	6.8	*(14.4)*	8.1	*(18.0)*	14.5	*(21.1)*
50%	18.7	*(26.3)*	20.5	*(30.3)*	26.8	*(33.3)*
90%	58.7	*(66.3)*	60.1	*(70.0)*	61.2	*(67.8)*

Table VII. Locations of apparent SOI, mass fraction injected and burned for all rate shapes at 21 MPa oil rail pressure, constant fuel quantity, and constant CA50. Numbers in italics and parentheses are the differences between that point and the apparent SOI for that condition

Crank Angle [°CA aTDC]	**100% ERS**		**50% ERS**		**0% ERS**	
Apparent SOI	-10.6		-13.9		-17.6	
Mass Fraction Injected						
5%	-8.4	*(2.3)*	-10.4	*(3.4)*	-12.6	*(5.0)*
10%	-6.9	*(3.7)*	-8.8	*(5.1)*	-10.6	*(7.0)*
50%	2.3	*(12.9)*	1.5	*(15.4)*	0.5	*(18.1)*
90%	10.2	*(20.8)*	9.8	*(23.7)*	8.8	*(26.4)*
Mass Fraction Burned						
5%	1.5	*(12.1)*	1.7	*(15.6)*	-0.8	*(16.7)*
10%	3.4	*(14.0)*	3.8	*(17.7)*	1.8	*(19.4)*
50%	16.0	*(26.6)*	17.1	*(30.9)*	16.3	*(33.9)*
90%	58.8	*(69.4)*	59.6	*(73.4)*	59.5	*(77.1)*

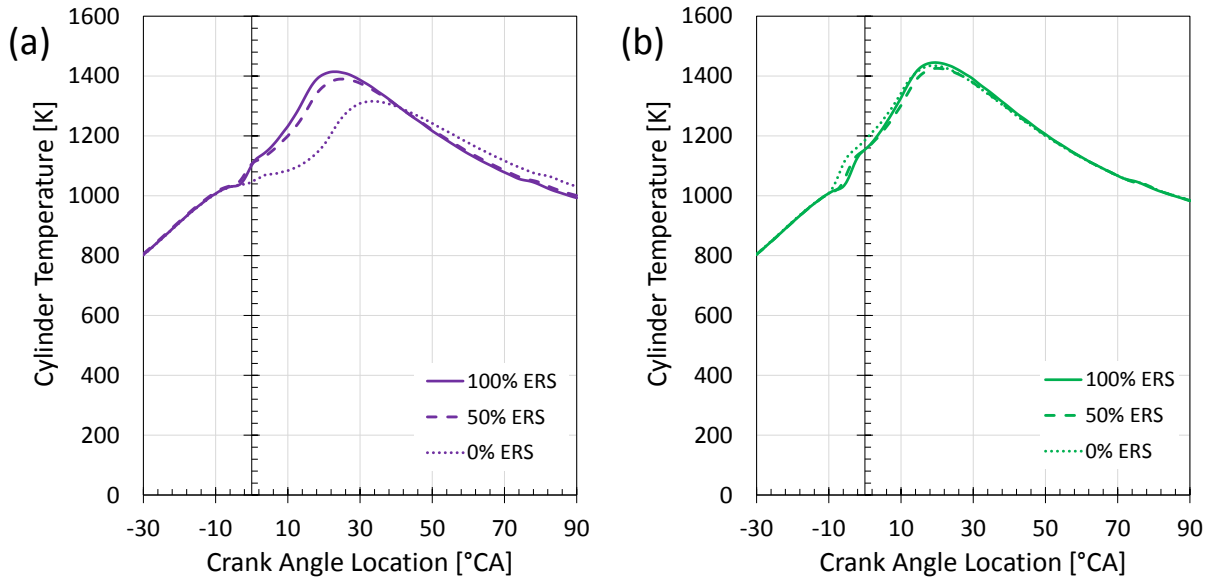

Figure 47. Mean gas temperature for all rate shapes at 21 MPa oil rail pressure, constant fuel quantity at (a) -8° CA aTDC SOI and (b) constant CA50.

Bulk gas temperature is calculated from the measured cylinder pressure and is shown in Figure 47. For case A, larger differences are seen between the lower boot pressure injection (0% ERS) and the medium and high boot pressure injections (50% ERS and 100% ERS). This reduction in burned products temperature correlates with the lower initial heat release rate and lower amount of fuel burned in the premixed combustion. However, this behavior is reversed when the CA50 is aligned between the rate profiles (case B). Temperature is slightly higher for the 0% and 50% ERS in the early part of combustion and nearly matches in the diffusion burn.

5.3.3 Engine Performance and Emissions

The effect of increased injection pressure rise rate (increasing % ERS) on brake mean effective pressure (BMEP) is shown in Figure 48 and on brake specific fuel consumption (BSFC) in Figure 49. For case A, the BMEP increases as the boot injection pressure increases while it remains fairly consistent for case B. The BSFC, representing the ratio of fuel flow to power generated, decreases with increase of injection pressure rise rate for both cases. This agrees with the behavior seen in the combustion analysis which showed higher peak cylinder pressures for case B for all injection profiles and lower peak cylinder pressures in case A for the 0% ERS injection. Advancing the SOI timing for case B allows for more fuel being burned early in the cycle and more power generated.

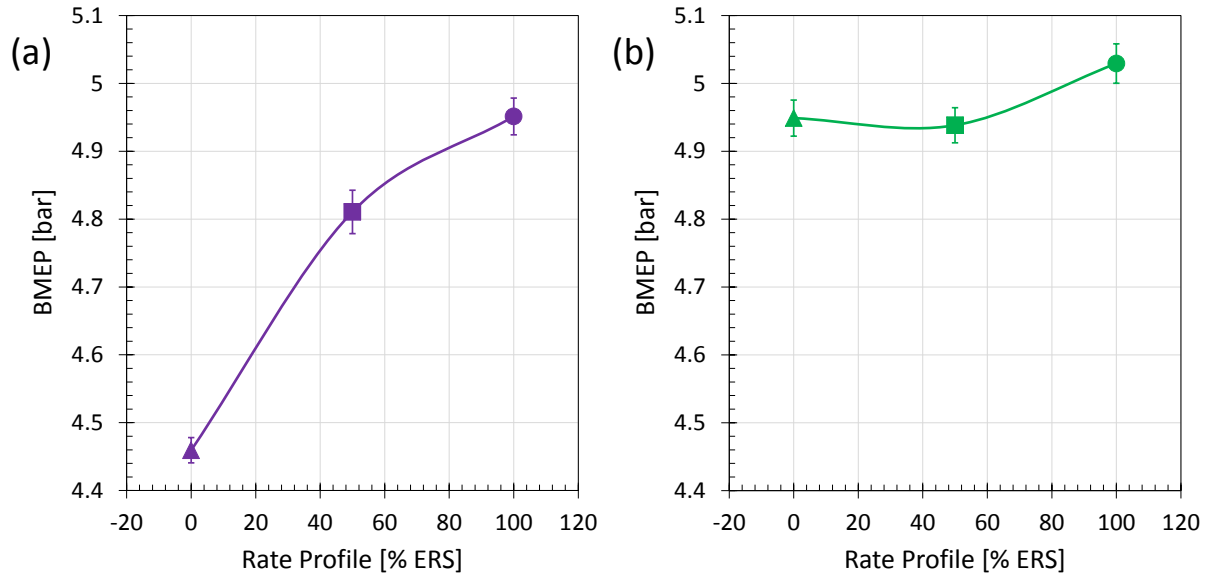

Figure 48. Brake Mean Effective Pressure for all rate shapes at 21 MPa oil rail pressure, constant fuel quantity at (a) -8° CA aTDC SOI and (b) constant CA50.

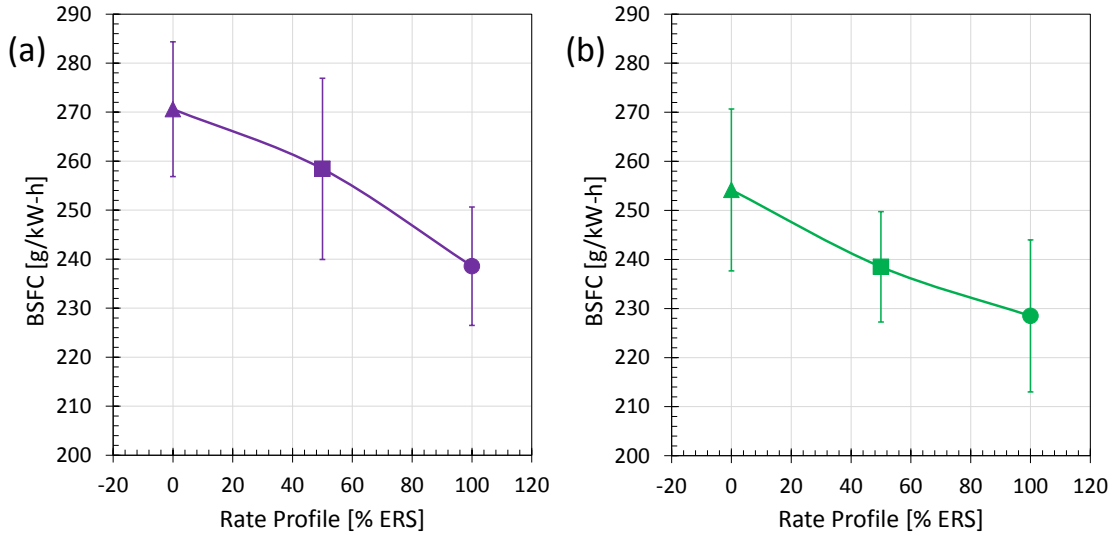

Figure 49. Brake specific fuel consumption for all rate shapes at 21 MPa oil rail pressure, constant fuel quantity at (a) -8° CA aTDC SOI and (b) constant CA50.

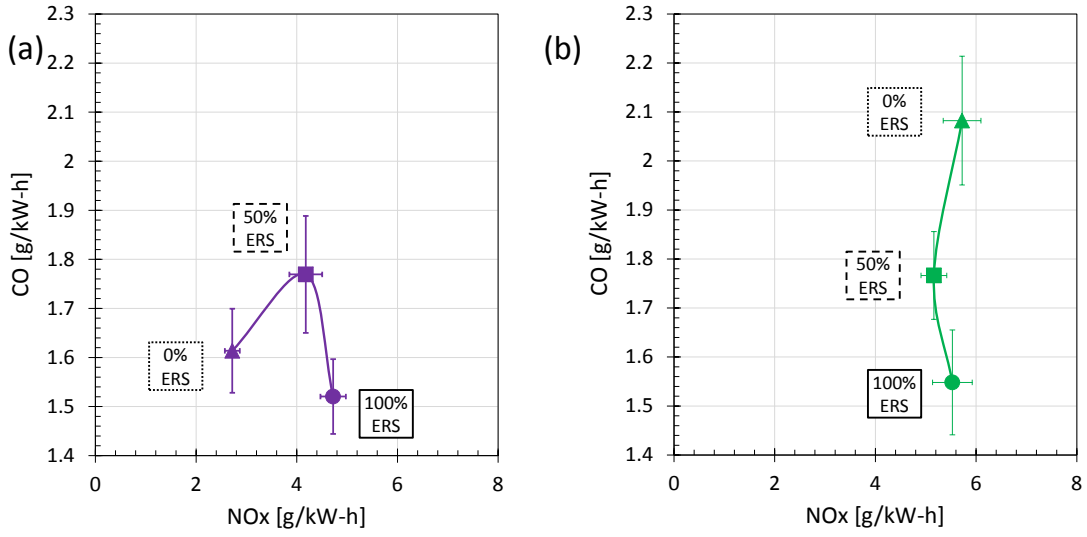

Figure50. Relationship between CO and NO_x emissions for all rate shapes at 21 MPa oil rail pressure, constant fuel quantity at (a) -8° CA aTDC SOI and (b) constant CA50.

The relationship between NO_x and CO emissions are shown in Figure 50. It is expected that lowering the combustion temperature would decrease the NO_x emissions. When looking at the case of common SOI timing (case A) a reduction in temperature (cf. Figure 47(a)) and resultant decrease in NO_x emissions is visible as the initial injection pressure rise rate decreases (100% to 0% ERS). However this comes with a penalty in power generation (cf. Figure 48(a)). Advancing the SOI timing to align the CA50 yields similar power across injection rate shapes (cf. Figure 48(b)) and causes the temperature of the 0% ERS injection to rise to values that were reached in the 100% and 50% ERS cases (cf. Figure 47(b)). This action removes the NO_x benefit and incurs a penalty in CO emissions as seen in Figure 50. The poorer mixing that results from the boot profiles can be attributed for this behavior as CO emissions correspond with less efficient combustion.

The CA50 for the 100% and 50% ERS are matched with each other in each study at ~19.5° for case A and ~16.5° for case B. Comparing only the 100% and 50% ERS injections between case A and case B it can be seen that there is a temperature increase when advancing the CA50 (cf. Figure 47) which results in an increase of NO_x emissions (CO emissions are comparable). Again this reduction in NO_x also involves a reduction in BMEP (cf. Figure 48). This suggests that the location of CA50 has a larger impact on the NO_x generation than the initial portion of the injection rate profile as there is a larger reduction in NO_x between the Case B_100% ERS condition and the Case A_100% ERS condition than there is between the Case B_100% ERS condition and the Case B_50% ERS case.

5.4 Summary

In this study, the effect of rate of injection profile on combustion and engine performance is investigated. Three injection rate shapes (100%, 50%, and 0% ERS) are studied with the largest variation in the initial transient portion of the injection event.

The first study kept the injection quantity and SOI timing commands to the ECU constant. It was found that the mass delivered between the three rate profiles differed as the boot pressure decreased and that the apparent SOI differed for each injection. In-cylinder imaging allowed for calculation of soot radiation temperature. These results, along with the heat release rate showed that the mass fraction burned are close for the 100% and 50% ERS injections where the 0% ERS condition trails on all accounts.

The next part of the study sought to correct some of the differences seen in the first exercise. In case A, the fuel injection quantity was kept constant across the three rate shapes by altering the command to the ECU. The SOI command was constant for all three rate shapes. For case B, the fuel injection quantity was kept the same as that in case A. The SOI command to the ECU was altered in order to align the location of 50% mass fraction burned. For case A, the 0% ERS case was delayed for all locations of mass fraction injected and mass fraction burned, while for case B, the 0% ERS case was advanced, followed by 50% ERS, and 100% ERS in order to align the location of 50% mass fraction burned.

Injection rate modulation is designed to decrease the fuel available for the premix burn and lower the temperature in order to decrease NO_x emissions. In Case A, it is found that slowing the initial injection rate does achieve a NO_x reduction with little effect on CO emissions, however it also decreases the BMEP, increases the BSFC. When the injections are advanced to align the location of 50% mass fraction burned, there is little difference in BMEP and BSFC across the injection rate shapes, however the NO_x benefit is no longer achieved with a slight penalty in CO emissions. Comparing the 100% and 50% ERS injections across the two cases (constant SOI and constant CA50) it can be seen that location of CA50 has a higher effect than slower initial injection rate on BMEP, BSFC, and NO_x emissions.

6 RESULTS – ALTERNATIVE FUEL STUDY

Parts of this chapter have been previously published as:

Ramírez, A.I., Som, S., LaRocco, L.A., Rutter, T.P., and Longman, D.E.: Investigating the use of Heavy Alcohols as a Fuel Blending Agent for Compression Ignition Engine Applications. *ASME 2012 Internal Combustion Engine Division Spring Technical Conference*, Paper Number ICES2012-81169, 2012.

Ramírez, A.I., Aggarwal, S.K., Som, S., Rutter, T.P., Longman, D.E.: Effects of Blending a Heavy Alcohol ($C_{20}H_{40}O$) with Diesel in a Heavy-Duty Compression-Ignition Engine. *Fuel*, 136:89-102, 2014.

The study of phytol was completed using a multi-step approach. The first step involved analysis of the chemical and physical properties of phytol and its blends with diesel. Next, robust in-nozzle flow simulations were performed to characterize the cavitation, turbulence, and flow characteristics of phytol and diesel [[92]93]. The final step of this work was to perform engine experiments with the blends of phytol and diesel and compare them to baseline diesel data.

6.1 Fuel Property Assessment

Samples of phytol, diesel, and their blends were sent to an external source for analysis of their physical and chemical properties [94,95] where all tests were performed in accordance to ASTM standards [96]. A distillation curve of phytol was produced using gas chromatography. Cetane number was tested by combustion in a constant volume chamber. Heat of combustion was determined in a bomb calorimeter. Note, because of instrumentation limits, it was not possible to accurately measure the vapor pressure of the blends. Hence, it was calculated using simple mixing rules. As indicated in Tables VIII and IX, several of the properties (relative hydrogen content, cetane number, heat of combustion, density, etc.) are not noticeably different for diesel, phytol, and their blends. However, there is significant difference with

respect to their viscosity and vapor pressure. Knowledge of these properties is important for both the inner-nozzle computational study, and also for the experimental investigation of the combustion and emission characteristics of the blends.

Table VIII. Comparison of physical and chemical properties of phytol and diesel fuels

Fuel Property	Diesel	Phytol
Carbon content [wt%]	86.64	80.62
Hydrogen content [wt%]	13.01	13.5
Oxygen content [wt%]	0	6.05
Molecular weight [g/mole]	~170	296.54
Sulphur content [ppm]	11.2	< 10
Heat of combustion [kJ/kg]	45,500	43,600
Heat of vaporization [kJ/kg]	361	130
Cetane number	47.7	45.9
Density @ 25°C [kg/m3]	849.2	850.9
Vapor pressure @ 25°C [Pa]	1000	< 1
Viscosity @ 25°C [cSt]	3.775	63.54
Boiling point [°C]	320	358

Table IX. Comparison of the physical and chemical properties of phytol, diesel, and three blends

Fuel Property	Diesel	P5	P10	P20	Phytol
Carbon content [wt%]	86.64	86.54	85.87	85.47	80.62
Hydrogen content [wt%]	13.01	13.14	13.11	13.19	13.5
Sulphur content [ppm]	11.2	10.3	10.5	< 10	< 10
Heat of combustion [kJ/kg]	45,500	45,400	45,400	45,100	43,600
Cetane number	47.7	47.0	46.1	45.9	45.9
Density @ 25°C [kg/m^3]	849.2	849	849	849.2	850.9
Vapor pressure @ 25°C [Pa]	1000	950	900	800	< 1
Viscosity @ 25°C [cSt]	3.775	4.115	4.69	6.142	63.54

6.2 Experimental Test Matrix

The engine was maintained at a constant speed of 1500 rpm. The engine specifications are provided in Table I of section 2.4. Since the HEUI injection system is used, the injection pressure is an artifact of oil rail pressure. In this work, the oil rail pressure was kept at 240 bar, which corresponds to a maximum injection pressure of 1584 bar according to the 6.6 ratio of the intensifier piston in the injector [61]. The quantity of fuel injected was maintained at a constant command of 100 mm^3/injection event. There was slight variation in actual delivery, which will be discussed later in the text. Intake and exhaust pressures were maintained at 1.54 and 1.39 bar, respectively. Blends of 5%, 10%, and 20% by volume of phytol (referred to as P5, P10, and P20, respectively) were compared to 100% diesel fuel. An injection timing sweep of three different locations of start of injection (SOI) was performed (8°, 4°, and 0° before top dead center [BTDC]). This results in a total of 12 different conditions, with 9 of them using phytol/diesel blends.

Table X. Experimental test matrix

Description	Value
Engine Speed	1500 rpm
Intake Pressure	1.54 bar
Exhaust Pressure	1.39 bar
Injection Quantity	100 mm^3/inj
Oil Rail Pressure	240 bar
(Injection Pressure)	*(1584 bar)*
Fuel	100% Diesel
	5% Phytol/95% Diesel (P5)
	10% Phytol/90% Diesel (P10)
	20% Phytol/80% Diesel (P20)
Injection Timing	8° BTDC
	4° BTDC
	0° BTDC

Table X gives more information on the test matrix. It is important to note how the SOI is controlled in the present set up. The software controlling the injection system allows for an input of SOI location (i.e., 8 degrees BTDC). The HEUI uses a double pulse solenoid current to give a single injection event. The internal map in the ECU governs the timing of the actual current executed in engine testing.

6.3 Results and Discussion

6.3.1 Properties of Fuel Blends

Distillation curves of phytol and diesel are shown in Figure 51, where it can be seen that the boiling point for pure phytol is higher than that of diesel. Properties of pure diesel and phytol can be seen in Table VIII. Most of the values are similar, with the larger differences in oxygen content, vapor pressure, and viscosity. On a long-term basis, higher viscosity fuel could cause problems such as engine deposits, injector coking, injector pump failure, and piston ring sticking [97]. The effects of fuel viscosity on engine performance have been widely studied with inconclusive findings. With regards to combustion, some have seen that higher viscosity could cause a longer physical delay for injection and poorer fuel atomization than the lower viscosity of pure diesel [98]. Others have reported that combined with a higher bulk modulus and sound speed, higher viscosity leads to an advanced start of injection, shifting combustion phasing [99,100]. In the aforementioned studies, the injection systems discussed are those with a positive displacement-type pump, thus the advanced SOI with higher viscosity fuel may come from less backflow and losses in the distributor pump. In the present work, a HEUI is used, and such effects are not expected. Lower vapor pressure of phytol would lead to less cavitation in comparison to diesel. This was confirmed by our computational results discussed in the next section. Fuels with higher oxygen content should lead to lower soot production in the combustion process [101]. In addition, Graboski et al. [102] performed studies using soybean oil and diesel blends and found good correlation between oxygen content in the fuel and loss of heating value.

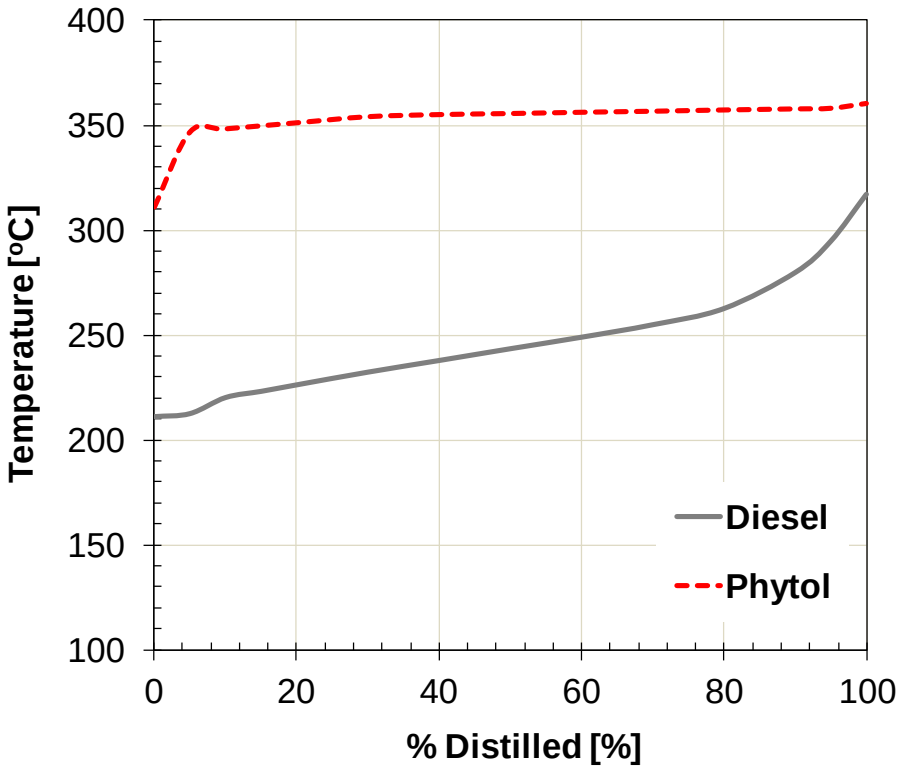

Figure 51. Distillation curves for Diesel and Phytol

Fuel properties of the blends are shown in Table IX. It can be seen that blending brings the blend properties closer to those of pure diesel, and thus more reasonable to run in the engine.

6.3.2 Experimental Investigation

Diesel and phytol/diesel blends were studied in the single-cylinder Caterpillar engine as described previously. Injection pressure (by means of oil rail pressure) and engine speed were held constant. The command for injection quantity was also held constant at 100 mm^3/inj; the actual flow amounts are shown in Figure 52.

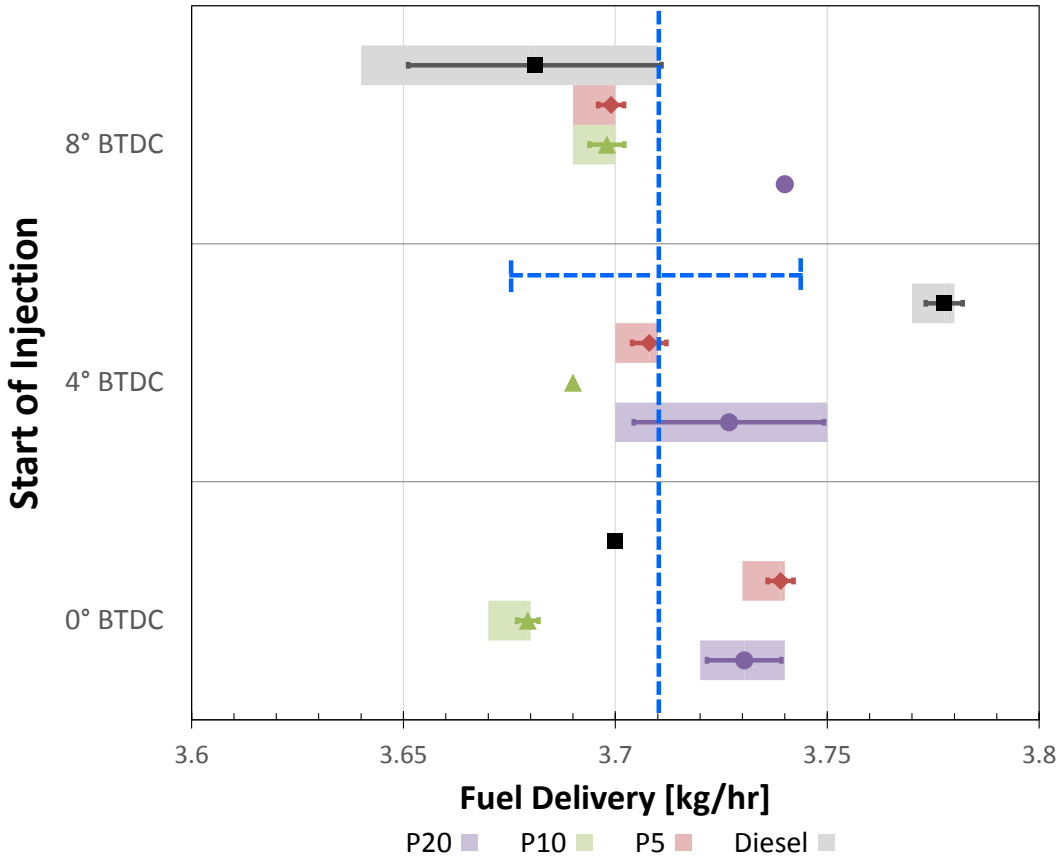

Figure 52. Actual amount of fuel injected per stroke when maintaining a constant injection quantity command. (Symbols represent the mean, error bars represent plus/minus one standard deviation, and the shaded regions show the range of maximum and minimum values. The dashed blue line represents the overall average with plus/minus one standard deviation indicated.)

Tat [99] and Usta [103] have observed higher volume of fuel injected in the case of biodiesel versus diesel and attributed this to the higher viscosity of the biodiesel decreasing backflow in the fuel injection pump. However as mentioned before, the use of a HEUI system would not have the same effects. In our study, it can be seen by the standard deviation and maximum/minimum flow rates of the different fuel

blends, that the actual fuel delivery is quite similar across fuel blends. The blending of the biodiesel with the diesel has decreased the disparity in viscosity that is seen with neat fuel.

Figure 53 compares diesel and the phytol blends in terms of cylinder pressure near the combustion event for the three injection timings of 8°, 4°, and 0° BTDC. For each condition, 100 pressure traces were acquired, and the average pressure trace is shown in the figure. It can be seen that the blended fuels yielded pressure traces similar to those of diesel, with only minor visible differences. Table XI shows peak pressure values and respective locations in terms of crank angle for each of the SOI cases and various fuel blends. The peak pressure values are close to each other in magnitude, with the largest difference in the 4° SOI case, even then only differing by 1.6 bar. The location of peak pressure is within 0.5 crank angle degrees for all of the cases. The peak pressure decreases as SOI timing retards for all of the fuels tested (cf. Figure 56). This can be expected as the time available for combustion is decreased as injection gets closer to TDC. This same behavior in which the phytol blends produced results comparable to those of diesel is seen for all injection timings performed.

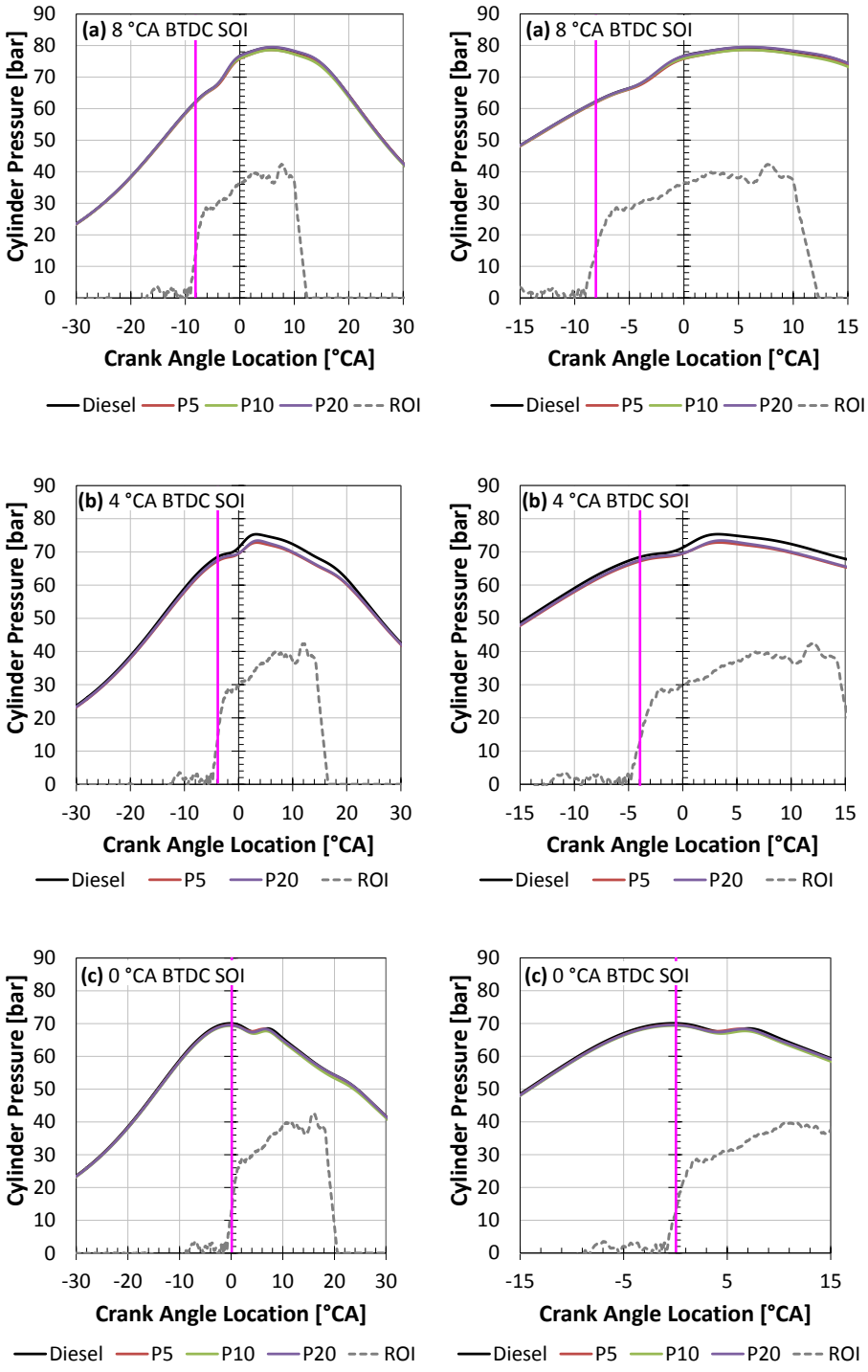

Figure 53. Cylinder pressure plot of diesel and phytol blends for a case with the injection timing at (a) 8° (b) 4°, and (c) 0° BTDC. (Zoomed image of each on right, SOI command indicated with pink line, ROI profile shown in dashed line)

Table XI. Peak cylinder pressure values and locations for each of the blends at various start of injection timings. NOTE: for 0 degree SOI timing case, peak cylinder pressure corresponds to compression pressure and not to combustion pressure. *indicates peak cylinder pressure from combustion.

Start of Injection Timing [°CA BTDC]	Fuel Type	Peak Cylinder Pressure [bar]	Coefficient of Variation (COV)	Location of Peak Cylinder Pressure [°CA BTDC]
8	Diesel	79.38	0.73	-5.86
	P5	78.78	0.80	-6.00
	P10	78.60	0.85	-5.84
	P20	79.51	0.77	-5.95
4	Diesel	74.41	0.45	-3.66
	P5	72.83	0.43	-3.34
	P10	--	--	--
	P20	73.43	0.40	-3.53
0	Diesel	70.05* 68.50†	0.12	-0.19* -7.00†
	P5	69.57* 68.37†	0.11	0.20* -6.20†
	P10	69.33* 67.71†	0.20	0.20* -6.70†
	P20	69.52* 68.32†	0.14	0.22* -6.60†

Figure 54 plots the heat release rate for the blends of phytol at different SOI timing. Overall there is good similarity between all the cases, although slightly more difference is seen in the premix burn phase compared to the diffusion burn phase of combustion. In the premix burn region the pure diesel shows slightly higher heat release rate than the phytol blends, with the curves collapsing on each other in the diffusion burn region. This is in agreement with the lower heat of combustion of the phytol/diesel blends versus the pure diesel. These differences are more pronounced as SOI timing approaches TDC. Phasing for the premix and diffusion burns displays good agreement between the blends at all injection timings.

Locations of 5, 10, 50, and 90% mass fraction burned are shown in Table XII. It is seen that the blends of phytol yield combustion phasing that is similar to the pure diesel. The combustion characteristics can be expected to be similar due to the similarities between the physical and chemical properties of diesel with the blends. It is likely that neat phytol would yield larger differences, however due to the high viscosity, this was not possible to test.

Table XII. Mass burn fraction (MBF) crank angle locations (shown in °BTDC) for each of the blends at the various start of injection timings.

8° CA BTDC SOI	**Diesel**	**P5**	**P10**	**P20**
5% MBF	0.30	0.22	0.05	0.40
10% MBF	-2.05	-2.33	-2.50	-2.10
50% MBF	-13.00	-13.12	-13.25	-12.90
90% MBF	-30.35	-31.27	-30.75	-30.65

4° CA BTDC SOI	**Diesel**	**P5**	**P10**	**P20**
5% MBF	-3.91	-4.20	--	-4.05
10% MBF	-6.34	-6.60	--	-6.48
50% MBF	-17.15	-17.25	--	-17.23
90% MBF	-34.39	-34.80	--	-34.23

0° CA BTDC SOI	**Diesel**	**P5**	**P10**	**P20**
5% MBF	-7.85	-7.85	-7.95	-7.78
10% MBF	-10.20	-10.50	-10.50	-10.35
50% MBF	-21.50	-21.60	-21.80	-21.43
90% MBF	-38.60	-39.35	-38.90	-38.58

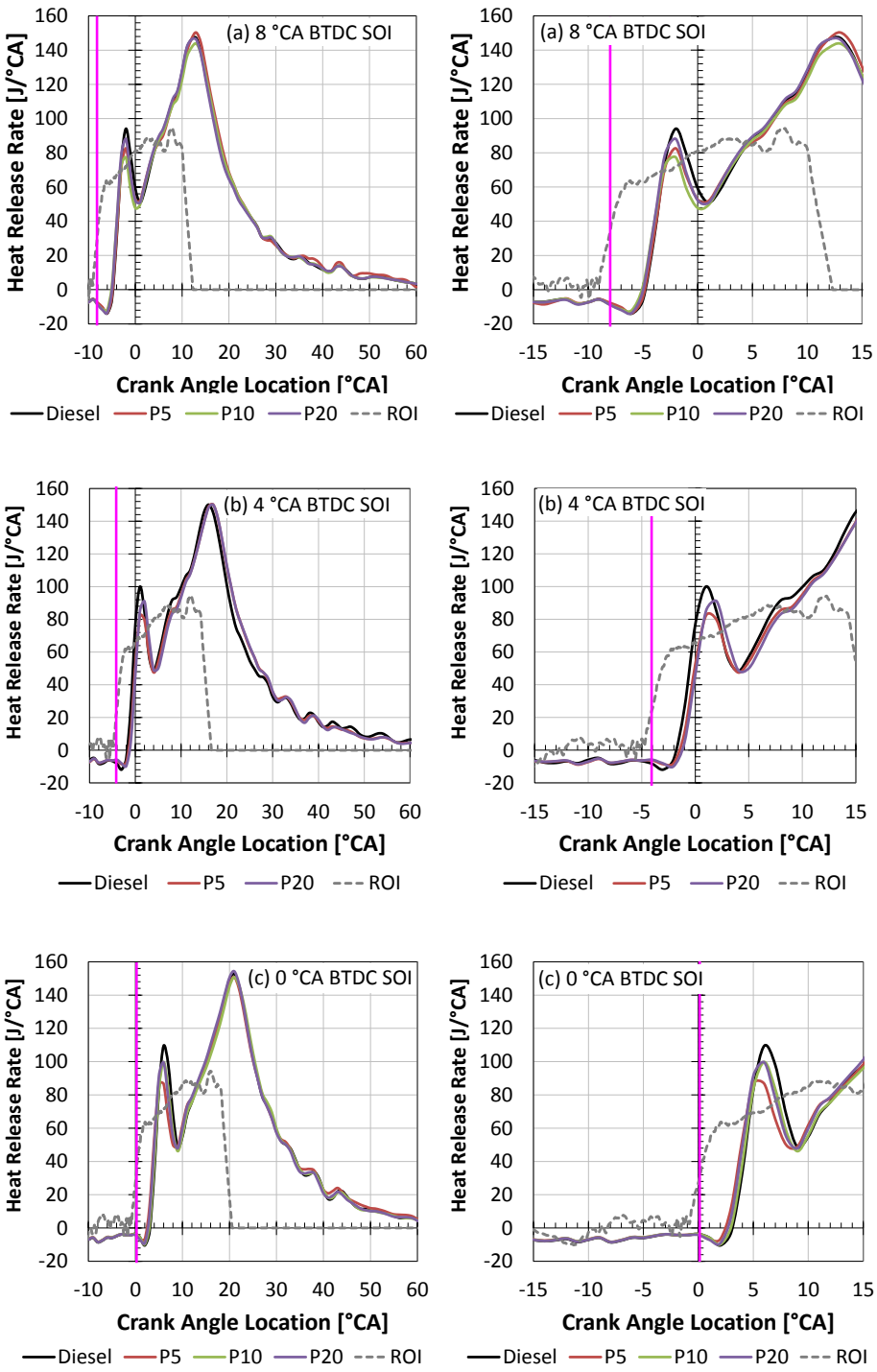

Figure 54. Heat Release Rate plot of diesel and phytol blends for a case with the injection timing at (a) 8°, (b) 4°, and (c) 0° BTDC. (Zoomed image of each on right, SOI command indicated with pink line, ROI profile shown in dashed line)

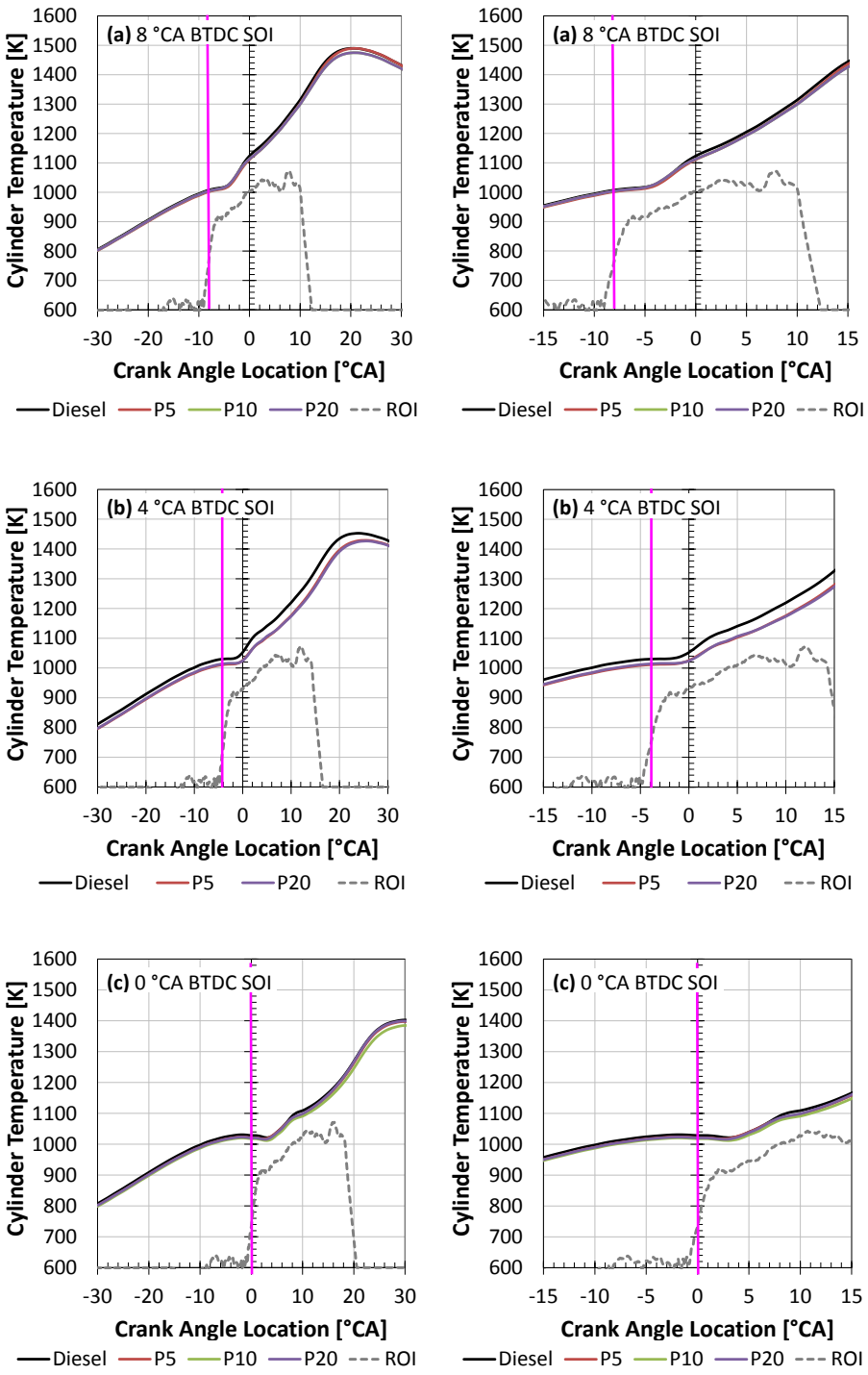

Figure 55. Cylinder temperature plot of diesel and phytol blends for a case with the injection timing at (a) 8°, (b) 4°, and (c) 0° BTDC. (Zoomed image of each on right, SOI command indicated with pink line, ROI profile shown in dashed line)

Cylinder temperature is shown in Figure 55 for each of the blends and injection timings. ROI profile is superimposed on the plots in Figures 53 - 55 to give some idea about the introduction of the fuel into the cylinder. This rate profile was measured using a Bosch-Type rate meter using a diesel surrogate at the same conditions used in the present work [67]. The solenoid current from engine testing and from these separate rate meter testing are aligned and the corresponding rate profile is shown. Due to the small amount of the fuel available, it was not feasible to obtain rate profiles for the blends. While the rate profiles for the blends may vary slightly from the diesel fuel itself, it can be used as a conception of injection. Taking a closer look at the SOI command and ROI profile with respect to cylinder temperature it can be seen that the 8, 4, and 0 °BTDC SOI timings inject at similar temperatures (~1000-1025 K). However, for the 8°BTDC SOI case the temperature is rising at this point while the temperature for 4°BTDC SOI case the temperature is starting to decline and the 0°BTDC case the temperature has been declining before injection commences. These differences in pressure and temperature in the cylinder will have an effect on combustion, specifically ignition delay. Ignition delay as computed from the difference in SOI command timing to the crank angle location where the heat release rate is 40 J/°CA is reported in Table XIII. For the case of 8° CA BTDC SOI, it is seen that as the percentage of phytol increases, the ignition delay decreases. However this pattern is not visible in the 4° and 0° CA BTDC SOI cases where there is not a clear pattern in ignition delay behavior as the amount of phytol changes.

Table XIII. Ignition delay (shown in °CA) as computed from SOI command to time taken to reach a heat release rate of 40 J/°CA for each of the SOI timings and fuel blends.

	Diesel	**P5**	**P10**	**P20**
8° CA BTDC SOI	4.23	4.22	4.05	4.04
4° CA BTDC SOI	3.27	3.70	--	3.85
0° CA BTDC SOI	4.13	3.67	4.03	3.78

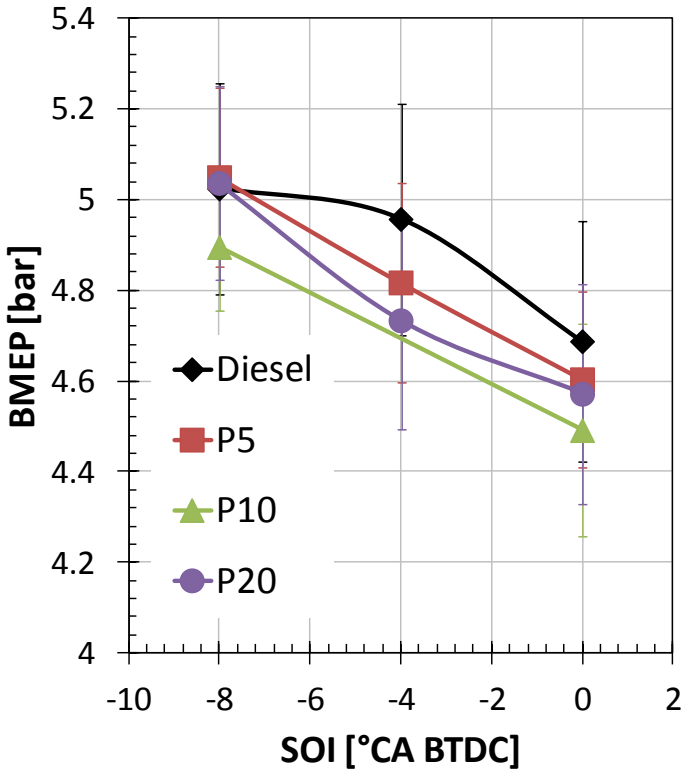

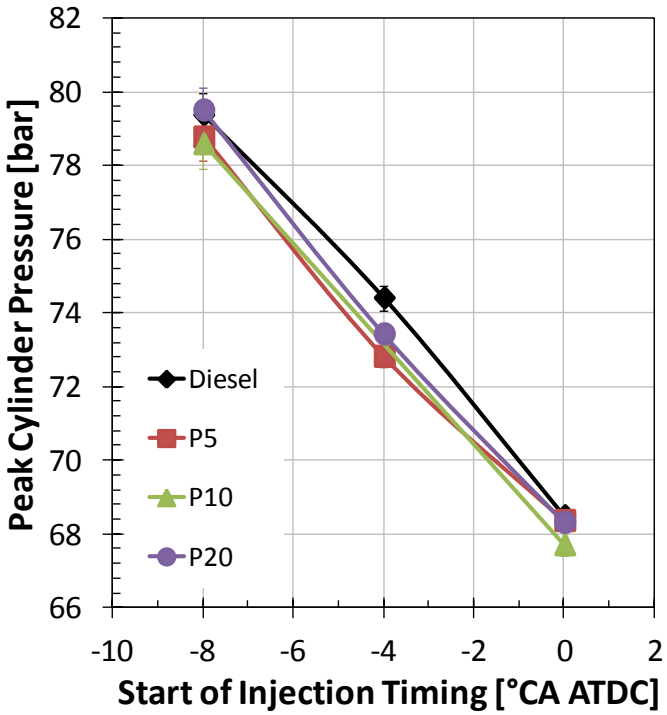

Figure 56. Peak cylinder pressure and brake mean effective pressure for diesel and phytol blends with respect to start of injection timing.

Lapuerta et al. describe a variety of studies with biodiesel from different feedstocks [104]. A reduced BMEP is seen in some cases corresponding to the decreased lower heating value of the biodiesel used versus diesel. However, some groups have observed very small loss or even an increase in power using biodiesel [103,105,106]. This power recovery was explained by the increased density and viscosity which could lead to advanced start of injection and fewer injection pump losses, in addition to an improved combustion efficiency of the biodiesel since it is an oxygenated fuel. A shift of the combustion phasing would also result from advanced SOI timing. Figure 56 shows variations in peak cylinder pressure (PCYLMAX) and brake mean effective pressure (BMEP) with respect to the SOI timing using the diesel and phytol blends from the present work. Bars representing one standard deviation are shown on the plot, indicating repeatability.

For both BMEP and peak pressure, diesel is slightly higher than the phytol/diesel blends. Although all of the values are close, the greatest variability is seen at an SOI timing of 4 degrees before TDC (4% and 2% difference between the maximum and minimum values in BMEP and peak pressure respectively). It may be anticipated that phytol/diesel blends would yield a lower power as a result of the lower heat of combustion of the fuel. Also, the reduced cetane number of the blends suggests a lower attainable peak pressure. Although we do not have information on differences of SOI of the blends with respect to the pure diesel, no significant differences in combustion phasing are apparent (cf. Figure 54, Table XII). As is suggested by the inner-nozzle simulations performed, cavitation is lower for the blended fuels (primarily P10 and P20) due to the difference in viscosity. This reduced cavitation and higher viscosity may lead to poorer atomization of the fuel. These effects combined with the lower cetane number for the blends may be responsible for the lower BMEP and peak pressures compared to pure diesel fuel. This is more apparent at later SOI timing i.e., 4° and 0° BTDC. It seems that combustion is not fully developed resulting in marginally lower peak pressure and less power for the blends. Still, the values yielded for BMEP and peak pressure are quite close to each other, reflective of a interplay between the various properties of pure

diesel and the blends that are expected to lower power output (lower heat of combustion, lower vapor pressure, higher viscosity, and lower cetane number) and those that could contribute to power recovery (higher oxygen content).

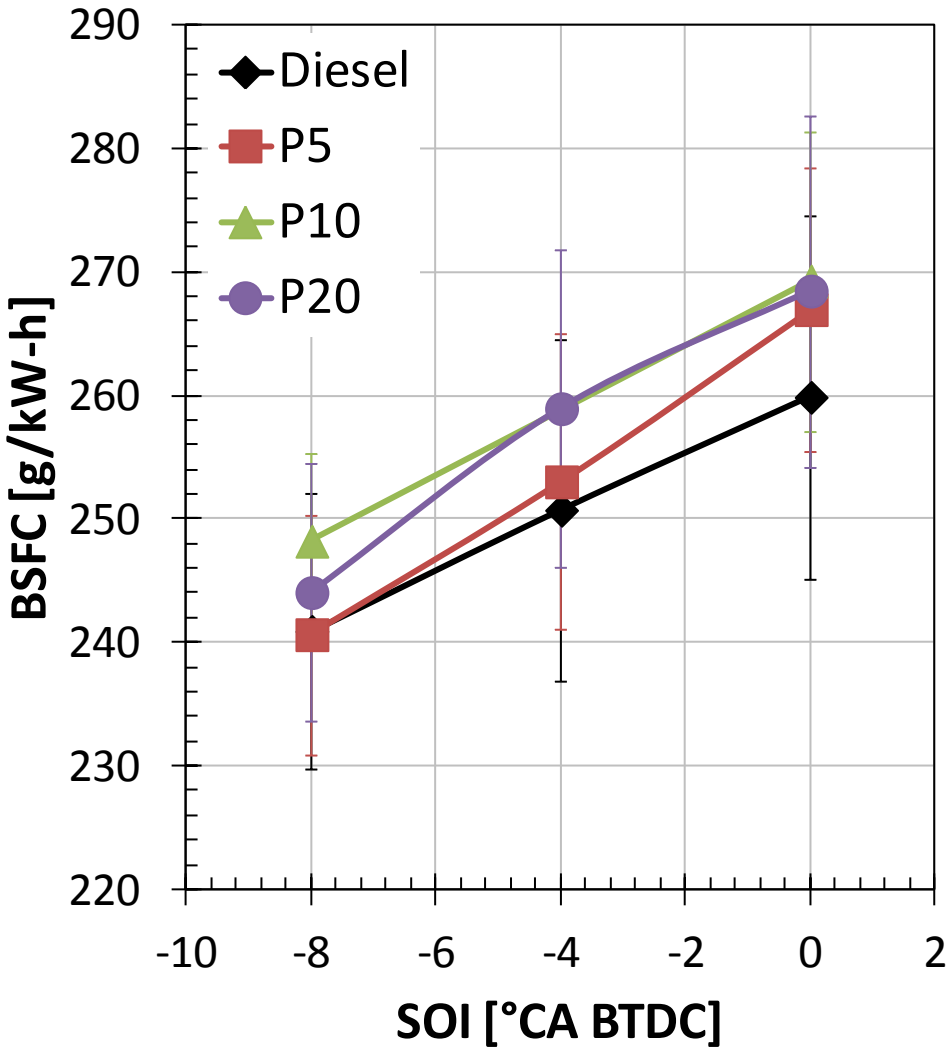

Figure 57. Brake Specific Fuel Consumption of Diesel and the Phytol/Diesel blends at various SOI timings

Brake Specific Fuel Consumption (BSFC), the ratio of fuel flow rate to power, is shown in Figure 57 for all the phytol/diesel blends and injection timings. It can be seen that BSFC is higher for the phytol/diesel blends than it is for pure diesel at the varied SOI timings. Fuel flow rates for all of the fuels used were comparable (cf. Figure 52), while power generated was lower for the blends. This can be attributed to the lower heat of combustion of the phytol blends versus that of diesel. Phytol has a higher oxygen content, which is an indicator of loss of heating value of the fuel, and thus an expected increase in fuel consumption. Rakopoulos et al. showed that there was increase in BSFC only when the oxygen increase is from the fuel and not from the intake air [107]. It is well know that not the volume of the fuel, rather its energy that yields power. Thus, the reduction in heat of combustion in the blends can contribute to the lower power and therefore the higher BSFC is observed with the blends.

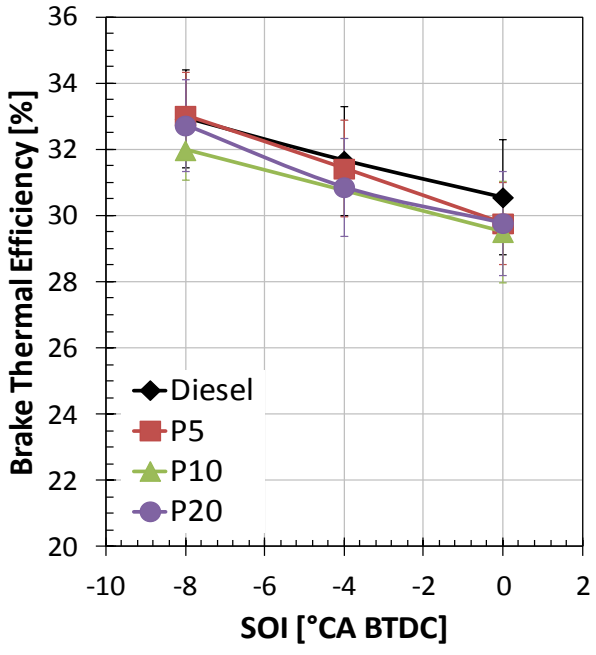

Figure 58. Brake Thermal Efficiency of Diesel and the Phytol/Diesel blends at various SOI timings.

Brake Thermal Efficiency (BTE) may be a more suitable measure for performance of the fuels since it takes into account the differences in heat of combustion of the fuel. This quantity represents the ratio of the engine's power output to the energy input (product of fuel mass flow rate and lower heating value). BTE for the diesel and phytol/diesel blends at each SOI timing is shown in Figure 58. BTE values are close to each other for diesel and blends at all SOI timings, with diesel showing higher efficiency than the blends. Largest differences are seen at an SOI timing of 0 degrees before TDC with a 3.4% loss of efficiency comparing blends versus diesel. Since BTE takes into account the difference in heating value of the fuel, it seems that lower cetane number and vapor pressure are showing effect here by having a lower power output at similar fuel delivery.

Combustion imaging was performed for each of the blends for all injection timing conditions. Figure 59 shows sample images for the 8° SOI case at a location 4° after top dead center (ATDC). The endoscope must be removed when switching fuel sources in order to clean the window. Its removal and reinsertion can lead to variability in the image perspective, which can be seen in the figure. The endoscope enters the combustion chamber just between two of the six plumes on the nozzle tip. In each of the images, the top of the piston crown is indicated by the dashed line. With the injector nozzle located at the center of the image, two spray plumes are clearly visible in the front of the image. Adjacent sprays can be seen in the background too. An inspection of the combustion images (left side of Figure 59) reveals no discernible differences. The images can be used to perform two-color optical pyrometry to calculate the soot radiation temperature, as described in other studies. [33,76,77,78]. The right side of Figure 59 shows the temperature distributions as calculated from the combustion images on the left. Qualitatively it can be seen in all cases that the higher temperatures are found around the periphery of the spray. This finding is consistent with the conceptual combustion model described by Dec [15]. At this point, it is difficult to make any generalizations about the in-cylinder combustion from the images obtained. Improvements to the camera repositioning after cleaning are needed to better quantify the combustion image variations

observed. This is illustrated specifically in the P5 case where it appears that the combustion cloud is actually smaller, when in actuality the image perspective is altered by camera positioning.

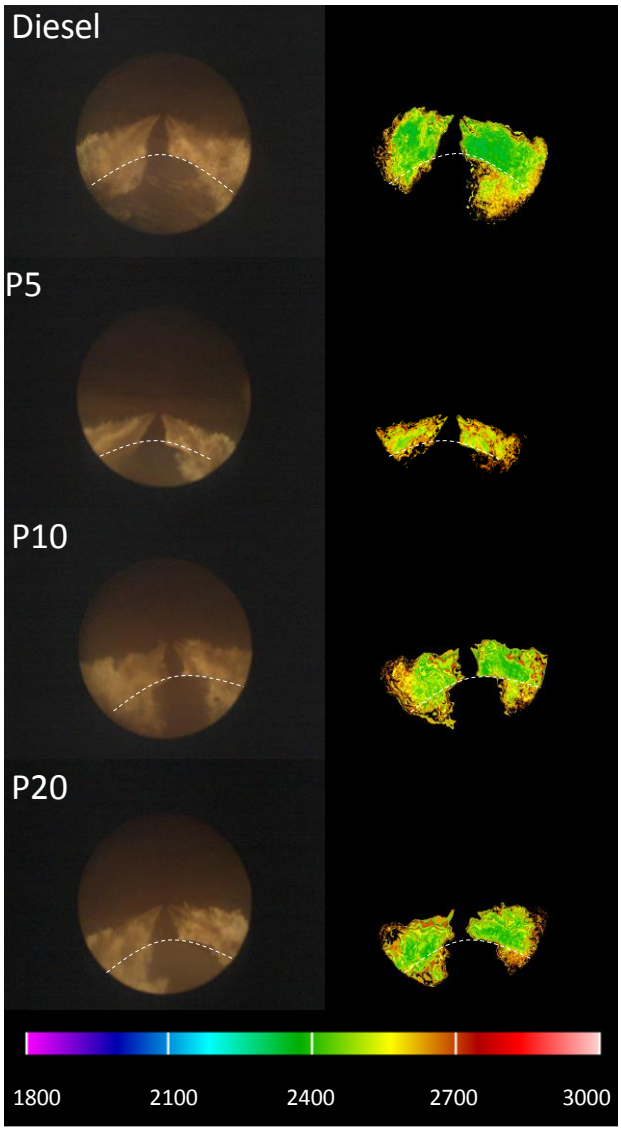

Figure 59. (left) Combustion imaging and (right) temperature distribution of the 8° BTDC injection timing case for diesel and phytol blends shown at 4° ATDC; piston crown is indicated by dashed white line.

Each condition was tested twice with 4 repetitions each, resulting in 8 distinct measurements taken for each data point. Quantitative temperature results are shown in Figure 60 for the SOI timing of 8° BTDC. The data represented here shows the average of these 8 points with error bars representing the standard deviation at each location. This plot verifies that the average temperatures of diesel and the blends are close, although the values are slightly higher for diesel. This was consistent with the marginally higher thermal NO_x emissions obtained with diesel, as indicated in Figure 61(a).

There is a high level of scatter seen for the P20 case towards the start of the cycle. This may be indicative of some instability caused by some differences in the fuel properties for this blend. Note that the temperature becomes much more stable towards 8 degrees after TDC. At this point, the injection event has ended, and there is no longer any fuel entering the cylinder. Further studies on repeatability during the time of injection would be valuable to understand this behavior.

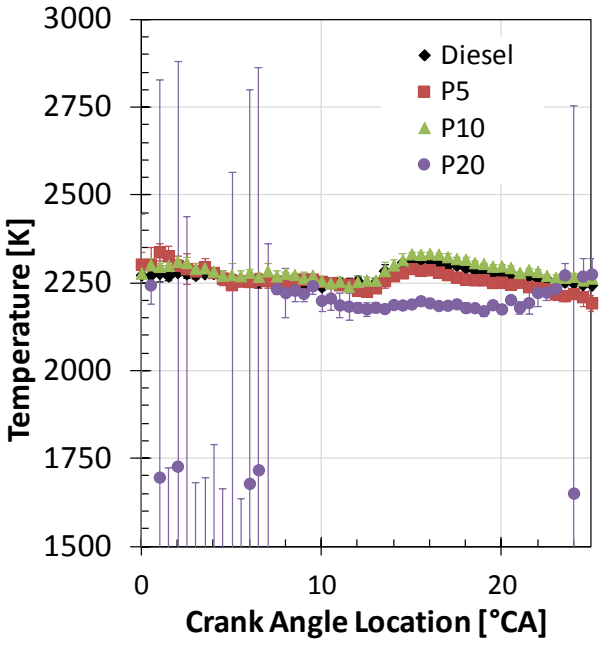

Figure 60. Average soot radiation temperature for diesel and phytol blends for the 8° BTDC SOI condition.

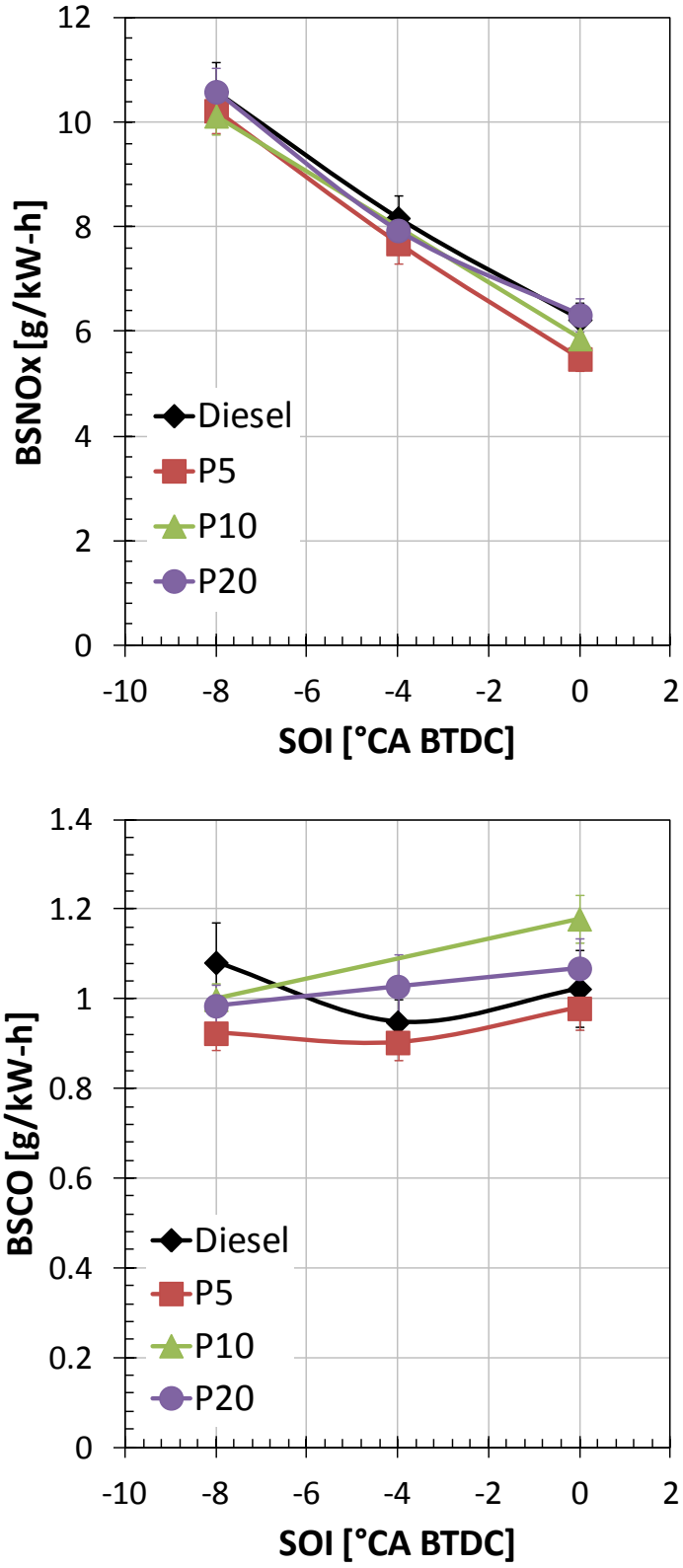

Figure 61. NO_x and CO as a function of injection timing

With regards to NO_x emissions with biodiesel and its blends with diesel, typically NO_x emissions increase with the percentage of biodiesel in the blend [108]. This has been explained by the advanced combustion phasing resulting from the physical properties of biodiesel that might yield an earlier SOI, which would produce higher temperatures in the engine cylinder. Other researchers have seen a decrease in NO_x emissions when using biodiesel [109,110]. However, as discussed previously, SOI variation due to different fuels are not expected with the HEUI system. In the present work, lower temperature is observed for the diesel/phytol blends, which supports the lower NO_x emissions compared to diesel, as shown in Figure 61(a). This lower temperature is a result to differences in mixing and combustion with the blends.

Generally, it is perceived that the increased oxygen content in biofuel would lead to more complete combustion and thus reduce CO emissions [40,104]. Ullman et al. showed that as cetane number and fuel oxygen content increase, CO emissions decrease [111]. In the present study, as the amount of phytol in the blend increases, oxygen content increases while cetane number decreases. Figure 61(b) plots CO versus SOI timing for diesel and phytol blends. At advanced SOI command timing (8 degrees before TDC), diesel has higher CO emissions. This trend shifts as injection timing is brought closer to TDC, with respect to CO emissions from pure diesel. Higher CO emissions from the P20 blend is seen at 4° BTDC, and from both P20 and P10 blends at 0° BTDC. It appears in the present study that there is an interplay between the oxygen content and the cetane number of the blends which is affected by combustion phasing (as a result of injection timing) as is seen in Figure 61(b).

6.4 Summary

In this study a heavy alcohol, phytol, is blended with diesel in different percentages and is run in a single-cylinder engine. Blending the phytol with the diesel yields physical characteristics that are close to pure diesel and thus conducive for engine testing. Cylinder pressure, performance, and emissions data are collected in addition to in-cylinder soot radiation images.

Engine performance quantities such as BMEP, BSFC, and BTE are in good agreement between pure diesel and phytol/diesel blends. NO_x emissions values are close for pure diesel and phytol/diesel blends with the blends showing slightly lower values. No consistent trend in CO emissions is visible. These behaviors suggest that phytol may be a suitable blending agent with diesel for use in internal combustion engines.

A comparison of combustion characteristics as shown through the cylinder pressure and resulting heat release rate and cylinder temperature show very little differences between the phytol blends and pure diesel. Heat release rate for the blends is slightly lower than that of pure diesel with more differences noted in the premix burn phase. This can be attributed to the lower energy of the phytol in comparison to diesel. One effect of higher viscosity in the blends may be an altered start of fuel injection. Since the injection rate was not measured, this could not be quantified. However, since no significant combustion phasing differences are present, it appears that either there are not much variations in SOI, or the effects of other phytol/diesel properties counteract the effects of altered SOI timing.

7 CONCLUSIONS

Parts of this chapter have been previously published as:

Ramírez, A.I., Som, S., Aggarwal, S.K., Kastengren, A.L., El-Hannouny, E.M., Longman, D.E., Powell, C.F.: Quantitative X-Ray Measurements of High-Pressure Fuel Sprays from a Production Heavy Duty Diesel Injector. *Experiments in Fluids*, 47(1):119-134, 2009.

Ramírez, A.I., Som, S., LaRocco, L.A., Rutter, T.P., and Longman, D.E.: Investigating the use of Heavy Alcohols as a Fuel Blending Agent for Compression Ignition Engine Applications. *ASME 2012 Internal Combustion Engine Division Spring Technical Conference*, Paper Number ICES2012-81169, 2012.

Ramírez, A.I., Aggarwal, S.K., Som, S., Rutter, T.P., Longman, D.E.: Effects of Blending a Heavy Alcohol ($C_{20}H_{40}O$) with Diesel in a Heavy-Duty Compression-Ignition Engine. *Fuel*, 136:89-102, 2014.

7.1 Synopsis

The work presented here is composed of three parts with a common objective of examining the characteristics of fuel injection and its effect on engine performance and emissions. The first part explored the fuel injection and atomization behavior in the very near-nozzle region using x-ray diagnostics. The second part investigated the impact of the fuel injection rate profile on engine combustion, performance, and emissions. In the last part, blends of diesel and an alternate fuel with different physical and chemical properties than those of diesel were studied. These seemingly different studies had a common thread focusing on the impact of injection conditions on fuel spray, combustion, and emissions in a one-cylinder diesel engine.

7.2 Concluding remarks

7.2.1 X-Ray Study

Sprays from an unaltered tip of a production HEUI were investigated at engine-like ambient density using x-ray radiography for two oil rail pressures. Spray characteristics in terms of the fuel penetration, spray mass distribution, mass-averaged axial spray velocity, and cone angle were reported.

Rate of injection (ROI) testing was also performed to supplement the x-ray experiments. The ROI profile from the rate meter exhibited a slow initial rise compared to that from x-ray measurements during the transient stages of injection. Using ROI profile from the rate meter yielded gross underprediction in the simulations. Consequently, the x-ray radiography data is judged to be a more accurate measure of ROI when fed as input to the simulations during the initial transients.

Although a direct comparison cannot be made between the performance of the HEUI dual-fluid multi-hole injection system and common rail single-fluid, single-hole injection system; on a bulk level they show several dissimilarities. Naturally, the differences in fluid dynamics of a single and multi-hole injector contribute to these differences. In addition, some of these could be attributed to dissimilarities in the initial transient rise in ROI between the two systems.

Measurements were initially used for the validation of spray atomization and dispersion models in STAR-CD and later in CONVERGE software. Simulations indicated good agreement with experiments in terms of the fuel penetration. While the trends in mass distribution were captured, simulations noticeably underpredict the transverse mass density profiles, demonstrating the need for improved spray models in the near nozzle region. The unique data-set also resulted in the development of a new primary spray breakup model called Kelvin Helmholtz Aerodynamic Cavitation Turbulence (KH-ACT), which has become part of the commercial CFD code CONVERGE [13].

Some anomalous behavior was observed regarding spray penetration in that the lower oil rail pressure case exhibited faster penetration than the higher rail pressure case. Detailed analysis based on the mass distribution measurements in the region close to nozzle exit indicated some spray broadening for the higher rail pressure case, implying some interference of neighboring sprays. While optical images of the spray indicated that the shield performed effectively, improvements will be made for subsequent measurements.

To the best of our knowledge, this was the first time that quantitative measurements of sprays using x-ray radiography have been obtained from a single plume of a 6-hole, full production nozzle at realistic engine-like densities.

7.2.2 Rate of Injection Study

In this work the rate of injection profile was varied by altering the rate of pressure rise during the initial part of injection. It has been proposed that reducing the initial pressure rise rate will introduce less fuel during the early part of combustion, reducing the premix burn, lowering the NO_x emissions. In the later part of injection, the pressure rise rate increases to improve mixing during the diffusion part of the burn. Three rate profiles were studied at a constant start of injection and then again by adjusting the SOI timing to align CA50 between the three cases.

A comparison is made between two rate profile cases (100% and 50% ERS), corresponding to high and medium initial pressure rise rate respectively, with CA50 aligned at two different crank angle locations – 16.5° and 19.5° CA aTDC. It is seen that advancing the CA50 increases peak pressure, BMEP, burned products temperature and thus NO_x emissions. The effect of the initial pressure rise rate is not prominent in neither the NO_x nor the CO emissions.

It was found that when SOI was maintained constant, the decrease in initial mass injected yields lower peak cylinder pressures, and gives lower BMEP. There is a reduction in burned products temperature which comes with a reduction in NO_x as the injection pressure rise rate is decreased. There is no visible trend in CO emissions.

When CA50 is aligned between the cases of varying rate profiles, there are less differences in peak cylinder pressures, BMEP, burned products temperatures, and thus NO_x emissions. As the initial pressure rise rate is decreased, a CO penalty is observed that is likely a result of the poorer mixing in the boot profiles.

7.2.3 Alternative Fuel Study

This work focused on the use of a biologically-derived heavy alcohol called phytol ($C_{20}H_{40}O$) and its potential for displacement of petrodiesel. First the properties of diesel, pure phytol, and 5%, 10%, and 20% phytol/diesel blends were analyzed. The assessment of phytol's physical and chemical properties revealed that it may be a suitable agent for blending with diesel fuel for CI engine applications. CFD modeling was performed by Dr. Sibendu Som to study the effects of the phytol on the inner-nozzle flow characteristics. With this knowledge, an experimental study was conducted to analyze the performance and emissions of various blends in a single-cylinder compression ignition engine. Important observations are as follows:

There are relatively small differences in the performance and emissions between diesel and phytol/diesel blends, indicating that phytol may be suitable as a blending agent with diesel. Simulations suggested that neat phytol fuel is not suitable for engine studies; thus, engine testing with this fuel was not attempted.

No significant differences in combustion phasing are visible in the range of blends used. This suggests that either there is not much difference in SOI, or the effects of the phytol/diesel properties counteract any of the effects of altered SOI timing.

NO_x and CO emissions resulting from the phytol/diesel blends are similar to those exhibited by the pure diesel. NO_x emissions of the blends are nearly identical with slightly lower values for the phytol/diesel blends. A consistent trend in CO emissions is not apparent.

In the case of advanced injection timing (8 deg BTDC) there are relatively more pronounced differences between the blends and the diesel, while the retarded injection timing case (0 deg BTDC) shows only minor differences.

Some instability is observed near the start of the combustion event for the P20 blend. However, the amplitude of this instability decreases once the injection event is over. Further studies on repeatability during the injection event for this blend would be valuable in the future.

7.3 Future Work

The motley assembly of studies presented in this thesis has led to an understanding of the importance of inner and near-nozzle characteristics – in particular the impact of rate of injection and physical properties on fuel spray, combustion, and resulting engine performance and emissions. The following recommendations are made for increased knowledge in these areas:

- In the rate of injection studies it was learned that modified initial injection rate impacts the combustion behavior in the engine. X-ray radiography studies of modified injection rate profiles will allow the visualization of the effect of the ROI on mass distribution in the spray.

These differences can then be correlated to combustion and heat release behavior observed in the engine. Coupling these sets of knowledge will additionally increase the capability of numerical simulation as differences in ROI profile and resultant mass distributions will be available.

- Alternative fuels are typically selected based on their similarities to existing fuels in use. However, depending on the feedstocks, large differences can be seen in physical properties such as viscosity and vapor pressure. While being tested in an engine, both physical and chemical properties are influencing the behavior. X-ray radiography investigations of alternative fuels with a wide range of different physical properties would bring about knowledge of the impact of certain physical properties without chemical reactions having effect. Along with rate meter measurements this information will help to characterize the impact of physical properties such as viscosity and vapor pressure on fuel spray.
- Differences in the heat release rate during the premix and diffusion burn stages were seen for the three rate profiles studied both for the constant SOI and constant CA50 studies. Each of these test conditions led to differences in emissions and performance characteristics. In-cylinder endoscopy testing at the different rate profiles would show differences in the combustion for these cases. Temperature and soot distributions could be calculated from these measurements which would then be possible. This would provide more information on the combustion cycle. This knowledge would allow for optimization of the use of these profiles in order to achieve desired conditions. In addition, soot data collection would be an ideal addition for these studies. It was seen that there was slightly elevated CO emissions for the boot injection profiles. Since CO typically trends with soot, this knowledge would show these effects in complement to the endoscopy measurements.

- Perform altered ROI studies using biofuels. Although it was not the case that the phytol/diesel blends produced higher NO_x emissions, for many biofuels this behavior is seen. Injection rate modulation was effective in reducing the NO_x emissions for some of the studies presented. This avenue could be explored and the behavior better understood with alternate fuels.
- Investigate the optimum location of CA50 while varying the rate of injection. This can be done for diesel in addition to alternative fuel blends.

CITED LITERATURE

1. Saroglia, G., Basso, G., Presti, M., Reizig, M. et al.: Application of New Diesel Aftertreatment Strategies on a Production 1.9 L Common-Rail Turbocharged Engine. *SAE World Congress* Paper 2002-01-1313, 2002.

2. Pierpont, D.A., Reitz, R.D.: Effects of Injection Pressure and Nozzle Geometry on D.I. Diesel Emissions and Performance. *SAE World Congress* Paper 950604, 1995.

3. Montgomery, D.R., Chan, M., Chang, C.T., Farrell, P.V., Reitz, R.D.: Effect of Injector Nozzle Hole Size and Number Spray Characteristics and the Performance of a Heavy Duty D.I. Diesel Engine. *SAE World Congress* Paper 962002, 1996.

4. Han, J-S., Lu, P-H., Zie, X-B. Lai, M-C., Nenein, N.: Investigation of Diesel Spray Primary Break-up and Development for Different Nozzle Geometries. *SAE World Congress* Paper 2002-01-2775, 2002.

5. Wang, T-C., Han, J-S., Xie, X-B., Lai, M-C., Henein, N.A., Schwarz, E., Bryzik, W.: Parametric Characterization of High-Pressure Diesel Fuel Injection Systems. Journal of Engineering for Gas Turbines and Power. Volume 125, pages 412-426, 2003.

6. Gavaises, M., Tonini, S., Arcoumanis, C.: Prediction of Liquid and Vapor Penetration of High Pressure Diesel Sprays. *SAE World Congress* Paper 2006-01-0242, 2006.

7. Giannadakis, E., Gavaises, M., Arcoumanis, C.: Modeling of Cavitation in Diesel Injector Nozzles. Journal of Fluid Mechanics. Volume 616, pages 153-193, 2008.

8. Desantes, J.M., Arrègle, J., Fenollosa, C., Salvador, F.J.: Analysis of the Influence of Injection Rate and Running Conditions on the Heat Release Rate in a D.I. Diesel Engine. *SAE World Congress*. Paper 2001-01-3185, 2001.

9. Agarwal, A.K., Srvastava, D.K., Dhar, A., Maurya, R.K., Shukla, P.C., Singh, A.P.: Effect of Fuel Injection Timing and Pressure on Combustion Emissions and Performance Characteristics of a Single Cylinder Diesel Engine. Fuel. Volume 111, pages 374-383, 2013.

10. Thurnheer, T., Edenhauser, D., Soltic, P., Schreiber, D., Kirchen, P., Sankowski, A.: Experimental investigation on Different Injection Strategies in a Heavy-Duty Diesel Engine: Emissions and Loss Analysis. Energy Conversion and Management. Volume 52, pages 457-467, 2011.

11. Powell, C.F., Yue, Y., Poola, R., Wang, J.: Time-Resolved Measurements of Supersonic Fuel Sprays using Synchrotron X-Rays. Journal of Synchrotron Radiation. Volume 7, pages 356-360, 2000.

12. Heywood, J.B.: *Internal Combustion Engine Fundamentals*. McGraw-Hill Book Company, 1988.

CITED LITERATURE (continued)

13. Som, S.: Development and Validation of Spray Models for Investigating Diesel Engine Combustion and Emissions. Ph.D. Dissertation, University of Illinois at Chicago, ProQuest/UMI, 2009.(Publication No. 3394243)

14. Battistoni, M., Grimaldi, C.N.: Numerical Analysis of Injector Flow and Spray Characteristics from Diesel Injectors using Fossil and Biodiesel Fuels. Applied Energy. Volume 97, pages 656-666, 2012.

15. Dec, J.E.: A Conceptual Model of DI Diesel Combustion Based on Laser-Sheet Imaging. *SAE World Congress* Paper 970873, 1997.

16. Siebers, D.L., Higgins, B.: Flame Lift-Off on Direct Injection Diesel Sprays Under Quiescent Conditions. *SAE World Congress* Paper 2001-01-0530, 2001.

17. Siebers, D.: Liquid-Phase Fuel Penetration in Diesel Sprays. *SAE World Congress* Paper 980809, 1998.

18. Arcoumanis, C., Cossali, E., Paal, G., and Whitelaw, J.: Transient Characteristics of Multi-Hole Diesel Sprays. *SAE World Congress* Paper 900480, 1990.

19. Kastengren, A.L., Powell, C.F., Wang, Y., Im, K-S., Wang, J.: X-Ray Radiography Measurements of Diesel Spray Structure at Engine-Like Ambient Density. *Proceedings of the 21st Annual Conference on Liquid Atomization and Spray Systems (ILASS)*, 2008.

20. Yue, Y., Powell, C.F., Poola, R., Wang, J., Schaller, J.K.: Quantitative Measurements of Diesel Fuel Spray Characteristics in the Near-Nozzle Region Using X-Ray Absorption. Atomization and Sprays. Volume 4, Issue 4, pages 471-490, 2001.

21. Cheong, S-K., Liu, J., Shu, D., Wang, J., Powell, C.F.: Effects of Ambient Pressure on Dynamics of Near-Nozzle Diesel Sprays Studied by Ultrafast X-Radiography. *SAE World Congress* Paper 2004-01-2026, 2004.

22. Powell, C.F., Yue, Y., Cheong, S-K., Cuenca, R., Ciatti, S., Shu, D., Wang, J.: Effects of Ambient Pressure on Fuel Sprays as Measured Using X-Ray Absorption. *Proceedings of the 16th Annual Conference on Liquid Atomization and Spray Systems (ILASS)*, 2003.

23. Ciatti, S.A., Powell, C.F., Cheong, S-K., Liu, J.Y., Wang, J., Tanner, F.X.: Comparison of X-Ray Based Fuel Spray Measurements with Computer Simulation Using the CAB Model. *CIMAC/ASME Congress* 2004.

24. Soteriou, C., Andrews, R., Smith, M.: Direct Injection Diesel Sprays and the Effect of Cavitation and Hydraulic Flip on Atomization. *SAE World Congress* Paper 950080, 1995.

25. Chaves, H., Knapp, M., Kubitzek, A., Obermeier, F., Schneider, T.: Experimental Study of Cavitation in the Nozzle Hole of Diesel Injectors Using Transparent Nozzles. *SAE World Congress* Paper 950290, 1995.

26. Payri, R., Salvador, F.J., Gimeno, J., de la Morena, J.: Macroscopic Behavior of Diesel Sprays in the Near-Nozzle Field. *SAE World Congress* Paper 2008-01-0929, 2008.

CITED LITERATURE (continued)

27. Leick, P., Riedel, T., Bittlinger, G., Powell, C.F., Kastengren, A.L., Wang, J.: X-Ray Measurements of the Mass Distribution in the Dense Primary Break-Up Region of the Spray from a Standard Multi-Hole Common-Rail Diesel Injection System. *Proceedings of the 21st Annual Conference on Liquid Atomization and Spray Systems (ILASS-Europe)*, 2007.

28. Tanner, F.X., Feigl, K.A., Ciatti, S.A., Powell, C.F., Cheong, S-K., Liu, J., Wang, J.: Analysis of X-Ray-Based Computer Simulations of Diesel Fuel Sprays. *Proceedings of the 17th Annual Conference on Liquid Atomization and Spray Systems (ILASS)*, 2004.

29. Tanner, F.X., Feigl, K.A., Ciatti, S.A., Powell, C.F., Cheong, S-K., Liu, J., Wang, J.: The structure of High-Velocity Dense Sprays in the Near-Nozzle Region. Atomization and Sprays, 16:579-597, 2006.

30. Nehmer, D.A., Reitz, R.D.: Measurement of the Effect of Injection Rate and Split Injections on Diesel Engine Soot and NO_x Emissions. *SAE World Congress* Paper 940668, 1994.

31. Ghaffarpour, M., Baranescu, R.: NO_x Reduction Using Injection Rate Shaping and Intercooling in Diesel Engines. *SAE World Congress* Paper 960845, 1996.

32. Tanabe, K., Kohketsu, S., Mori, K., Kawai, K.:Innovative Injection Rate Control with Next Generation Common Rail Fuel Injection System. *Proceedings of Seoul FISITA World Automotive Congress*, 2000.

33. Ikegami, M., Koichiro, N., Tanaka, S., Yamane, K.: Fuel Injection Rate Shaping and Its Effect on Exhaust Emissions in a Direct-Injection Diesel Engine Using a Spool Acceleration Type Injection System. *SAE World Congress* Paper 970347, 1997.

34. Benajes, J., Payri, R., Molina, S., Soare, V.: Investigation of the Influence of Injection Rate Shaping on the Spray Characteristics in a Diesel Common Rail System Equipped with a Piston Amplifier. *Transactions of the ASME*, 2005.

35. Desantes, J.M., Benajes, J., Molina, S., González, C.A.: The Modification of Fuel Injection Rate in Heavy-Duty Diesel Engines. Part 1: Effects on Engine Performance and Emissions. Applied Thermal Engineering. Volume 24, pages 2701-2714, 2004.

36. Fisher, B., Mueller, C.: Effects of Injection Pressure, Injection-Rate Shape, and Heat Release on Liquid Length *SAE World Congress* Paper 2012-01-0463, 2012.

37. Desantes, J.M., Benajes, J., Molina, S., González, C.A.: The Modification of the Fuel Injection Rate in Heavy-Duty Diesel Engines. Part 2: Effects on Combustion. *Journal of Applied Thermal Engineering* 24, 2715-2726, 2004.

38. Beck, N.J., Chen, S.K.: Injection Rate Shaping and High Speed Combustion Analysis – New Tools for Diesel Engine Combustion Development. SAE World Congress Paper 900639, 1990.

39. Herzog, P.L., Bürgler, L., Winklhofer, E., Zelenka, P., Cartellieri, W.: NO_x reduction strategies for DI diesel engines. *SAE World Congress* Paper 920470, 1992.

CITED LITERATURE (continued)

40. Agarwal, A.: Biofuels (Alcohols and Biodiesel) Applications as Fuels for Internal Combustion Engines. *Progress in Energy and Combustion Science*, 33:233-271, 2007.

41. Edwards, R., Larive, J.F., Rouveirolles, P.: Well-to-Wheels Analysis of Future Automotive Fuels and Power-Trains in the European Context. Well-to-Wheels report, European Commission Joint Research Center, page 1-60, January 2001.

42. Graboski, M.S., McCormick, R.L.: Combustion of Fat and Vegetable Oil Derived Fuels in Diesel Engines. Progress in Energy and Combustion Science. Volume 24, pages 125-164, 1998.

43. Armas, O., Hernandez, J., Cardenas, M.: Reduction of Diesel Smoke Opacity from Vegetable Oil Methyl Esters during Transient Operation. Fuel. Volume 85, pages 2427-2438, 2006.

44. Grimaldi, C.N., Postrioti, L., Battistoni, M., Millo, F.: Common rail HSDI diesel engine combustion and emissions with fossil/bio-derived fuel blends. *SAE World Congress*. Paper 2002-01-0865, 2002.

45. Hashimoto, M., Dan, T., Asano, I., Arakawa, T.: Combustion of the Rape-Seed Oil in a Diesel Engine. *SAE World Congress*. Paper 2002-01-0865, 2002.

46. Agarwal, A.K.: Performance Evaluation and Tribological Studies on a Biodiesel Fuelled Compression Ignition Engine. Ph.D. thesis, Indian Institute of Technology, Delhi, 1999.

47. Higgins, B.S., Mueller, C.J., Siebers, D.L.: Measurements of Fuel Effects on Liquid-Phase Penetration in DI Sprays. *SAE World Congress* Paper 1999-01-0519, 1999.

48. Knothe, G., Cermak, S.C., Evangelista, R.L.: Cuphea Oil as source of Biodiesel with Improved Fuel Properties Caused by High Content of Methyl Decanoate. Energy and Fuels, Volume 23, pages 1743-1747, 2009.

49. Fisher, B.T., Knothe, G.., Mueller, C.J.: Liquid Phase Penetration under Unsteady In-Cylinder Conditions: Soy- and Cuphea-Derived Biodiesel Fuels Versus Conventional Diesel. Energy and Fuel. Volume 24, pages 5163-5180, 2010.

50. Aatola, H., Larmi, M., Sarjovaara, T., Mikkonen, S.: Hydrotreated Vegetable Oil (HVO) as a Renewable Diesel Fuel: Trade-Off between NO_x, Particulate Emission, and Fuel Consumption of a Heavy Duty Engine. *SAE World Congress* Paper 2008-01-2500, 2008.

51. Gong, Y., Kaario, O., Tilli, A., Larmi, M., Tanner, F.X.: A Computational Investigation of Hydrotreated Vegetable Oil Sprays Using RANS and a Modified Version of the RNG k-ε Model in OpenFOAM. *SAE World Congress* Paper 2010-01-0739, 2010.

52. Hansen, A.C., Zhang, Q., Lyne, P.W.L.: Ethanol-Diesel Fuel Blends – A Review. Bioresource Technology. Volume 96, pages 277-285, 2005.

53. Rakopoulos, D.C., Rakopoulos, C.D., Papagiannakis, R.G., Kyritsis, D.C.: Combustion Heat Release Analysis of Ethanol or n-Butanol Diesel Fuel Blends in Heavy-Duty DI Diesel Engine. Fuel. Volume 90, pages 1855-1867, 2011.

CITED LITERATURE (continued)

54. Rakopoulos, D.C., Rakopoulos, C.D., Hountalas, D.T., Kararas, E.C., Giakoumis, E.G., Papagiannakis, R.G.: Investigation of the Performance and Emissions of Bus Engine Operating on Butanol/Diesel Fuel Blends. Fuel. Volume 89, pages 2781-2790, 2010.

55. Yang, Y., Dec, J., Dronniou, N., Simmons, B.: Characteristics of Isopentanol as a Fuel for HCCI Engines. *SAE World Congress* Paper 2010-01-2164, 2010.

56. www.sigmaaldrich.com/united-states.html

57. Lapuerta, M., Armas, O., Ballesteros, R.: Diesel Particulate Emissions from Biofuels Derived from Spanish Vegetable Oils. *SAE World Congress* Paper 2002-01-1657, 2002.

58. Som, S., Longman, D.E., Ramírez, A.I., Aggarwal, S.K.: A Comparison of Injector Flow and Spray Characteristics of Biodiesel with Petrodiesel. Fuel. Volume 89, pages 4014-4024, 2010.

59. Som, S., Aggarwal, S.K.: Effects of Primary Breakup Modeling on Spray and Combustion Characteristics of Compression Ignition Engines. Combustion and Flame. Volume 157, pages 1179-1193, 2010.

60. Som, S., Ramírez, A.I., Longman, D.E., Aggarwal, S.K.: Effect of Nozzle Orifice Geometry on Spray, Combustion, and Emission Characteristics under Diesel Engine Conditions. Fuel. Volume 90, pages 1267-1276, 2010.

61. Yudanov, S.V.: Development of the Hydraulically Actuated Electronically Controlled Unit Injector for Diesel Engines. *SAE World Congress* Paper 952057, 1995.

62. Mulemane, A., Han, J-S., Lu, P-H., Yoon, S-J., Lai, M-C.: Modeling Dynamic Behavior of Diesel Fuel Injection Systems. *SAE World Congress* Paper 2004-01-0536, 2004.

63. Stockner, A.R., Flinn, M.A., Glassey, S.F.: HEUI – A New Direction for Diesel Engine Fuel Systems. *SAE World Congress* Paper 930270, 1993.

64. Stockner, A.R., Flinn, M., Camplin, F.: Development of the HEUI Fuel System-Integration of Design, Simulation, Test, and Manufacturing. *SAE World Congress* Paper 930271, 1993.

65. Kastengren A.L., Powell C.F., Riedel, T., Cheong S.K., Wang Y., Im K.S., Liu Xin, Wang J.: Determination of Diesel Spray Axial Velocity using X-ray Radiography. *SAE World Congress* Paper 2007-01-0666, 2007.

66. Powell CF, Yue Y, Poola R, Wang J, Lai MC, Schaller J: X-ray Measurements of High Pressure Diesel Sprays. *SAE World Congress* Paper 2001-01-0531, 2001.

67. Bosch, W.: The Fuel Rate Indicator: A New Measuring Instrument for Display of the Characteristics of Individual Injection. *SAE World Congress* Paper 660749, 1966.

68. AVL: Operating Manual: Fuel Balance 733S. Graz, Austria, 2005.

CITED LITERATURE (continued)

69. Sierra Instruments: FlatTrak™ 780S Series Mass Flow Meter. Monterey, CA, 2000.

70. Rosemount Analytical's system: Chemiluminescence Detector Analyzer Module. Anaheim, CA, 1999.

71. http://www.cambustion.com/products/hfr500/fast-fid-principles

72. Rosemount Analytical: Series 1000 Gas Analyzers. Hasselroth, Germany, 2004.

73. AVL ThermoVision™ Manual, AVL, Austria, March 2004

74. Ciatti, S.A., Miers, S.A., Ng, H.K.: Influence of EGR on soot/NO_x production in a light-duty diesel engine. *American Society of Mechanical Engineers – Internal Combustion Engine Fall Technical Conference.* 2005-1327, 2005.

75. https://www.avl.com/its

76. Zhao, H., Ladommatos, P.: Optical Diagnostics for Soot and Temperature Measurement in Diesel Engines. *Progress in Energy and Combustion Science*, 4(3):221-256, 1998.

77. Shiozaki T., Nakajima, H., Yojota, H., Miyashita, A.: The Visualization and its Analysis of Combustion Flame in DI Diesel Engine. *SAE World Congress* Paper 980141, 1998.

78. Ciatti, S.A., Blobaum, E.L., Foster, D.E.: Determination of Diesel Injector Nozzle Characteristics Using Two-Color Optical Pyrometry. *SAE World Congress* Paper 2002-01-0746, 2002.

79. Bower, G.R., Foster, D.E.: A Comparison of the Bosch and Zuech Rate of Injection Meters. SAE World Congress Paper 910724, 1991.

80. AVL Concerto 2010 Release Notes, AVL, Austria, February 2010.

81. Society of Automotive Engineers Standard, SAE J1349, "Engine Power Test Code – Spark Ignition and Diesel," June 1985.

82. CFR Title 40, Chapter 1, Part 86, Subpart D, "Emissions Regulations for New Gasoline-Fueled and Diesel-Fueled Heavy-Duty Engines; Gaseous Exhaust Test Procedures."

83. Bakenhus, M., Reitz, R.D.: Two-Color Combustion Visualization of Single and Split Injections in a Single-Cylinder Heavy-Duty D.I. Diesel Engine Using an Endoscope-Based Imaging System. *SAE World Congress* Paper 1999-01-1112, 1999.

84. Hottel, H.C., Broughton, F.P.: Determination of True Temperature and Total Radiation from Luminous Gas Flames. *Industrial and Engineering Chemistry, Analytical Edition*, Volume 4, 1932.

CITED LITERATURE (continued)

85. Matsui, Y., Kamimoto, T., Matsuoka, S.: A Study on the Time and Space Resolved Measurement of Flame Temperature and Soot Concentration in a D.I. Diesel Engine by the Two-Color Method. *SAE World Congress* Paper 790491, 1979.

86. Tree, D.R.: Soot Particulate Size and Number Density Measurements in a Direct Injection Diesel Engine Using Light Scattering, Radiation, and Extinction. Ph.D. Thesis, Department of Mechanical Engineering, University of Wisconsin – Madison, 1992.

87. Flynn, P., Mizusawa, M., Uyehara, O.A., Myers, P.S.: An Experimental Determination of the Instantaneous Potential Radiant Heat Transfer within an Operating Diesel Engine. *SAE World Congress* Paper 720022, 1972.

88. Ramírez, A.I., Som, S., Aggarwal, S.K., Kastengren, A.L., El-Hannouny, E.M., Longman, D.E., Powell, C.F.: Quantitative X-Ray Measurements of High-Pressure Fuel Sprays from a Production Heavy Duty Diesel Injector. *Experiments in Fluids*, 47(1):119-134, 2009.

89. Naber, J., Siebers, D.L.: Effects of Gas Density and Vaporization on Penetration and Dispersion of Diesel Sprays. *SAE World Congress* Paper 960034, 1996.

90. Payri, R., Salvador, F., Gimeno, J., de la Morena, J.: Macroscopic Behavior of Diesel Sprays in the Near-Nozzle Field. *SAE International Journal of Engines* 1(1): 528-536, 2009.

91. Erlach, H., Chmela, F., Cartellieri, W., Herzog, P.: Pressure Modulated Injection and Its Effect on Combustion and Emissions of a HD Diesel Engine. *SAE World Congress*. Paper 952059, 1995.

92. Ramírez, A.I., Som, S., LaRocco, L.A., Rutter, T.P., and Longman, D.E.: Investigating the use of Heavy Alcohols as a Fuel Blending Agent for Compression Ignition Engine Applications. ASME 2012 Internal Combustion Engine Division Spring Technical Conference, Paper Number ICES2012-81169, 2012.

93. Ramírez, A.I., Aggarwal, S.K., Som, S., Rutter, T.P., Longman, D.E.: Effects of Blending a Heavy Alcohol ($C_{20}H_{40}O$) with Diesel in a Heavy-Duty Compression-Ignition Engine. *Fuel*, 136:89-102, 2014.

94. http://www.swri.org/4org/d08/petprod/fuelana/home.htm

95. http://www.astm.org/LABS/filtrexx40.cgi?+-P+ACCTNO+82650+template.frm

96. http://www.astm.org/

97. Kegl, B.: Effects of Biodiesel on Emissions of a Bus Diesel Engine. *Bioresource Technology*, 99(4):863-873, 2000.

98. Machacon, H.T.C., Shiga, S., Karasawa, T., Nakamura, H.: Performance and Emission Characteristics of a Diesel Engine Fueled with Coconut Oil-Diesel Fuel Blend. *Biomass & Bioenergy*, 20:63-69, 2000.

99. Tat, M.E.: Investigation of Oxides of Nitrogen Emissions from Biodiesel-Fueled Engines. Ph.D. thesis, Iowa State University, 2003.

CITED LITERATURE (continued)

100. Monyem, A., Van Gerpen, J.H., Canakci, M.: The Effect of Timing and Oxidation on Emissions from Biodiesel-fueled Engines. *Transactions of the ASAE 2001*. 44 (1): 35-42, 2001.

101. Schmidt, K., Van Gerpen, J.H.: The effect of biodiesel fuel composition on diesel combustion and emissions. *SAE World Congress* Paper 961086, 1996.

102. Graboski, M.S., Ross, J.D., McCormick, R.L.: Transient emissions from no. 2 Diesel and Biodiesel Blends in a DDC Series 60 Engine. *SAE World Congress* Paper 961166, 1996.

103. Usta, N.: An Experimental Study on Performance and Exhaust Emissions of a Diesel Engine Fuelled with Tobacco Seed Oil Methyl Ester. *Energy Convers Manage* 46:2373-86, 2005.

104. Lapuerta, M., Armas, O., Rodriguez-Fernandez, J.: Effect of Biodiesel Fuels on Diesel engine Emissions. *Progress in Energy and Combustion Science*, 34:198-223, 2008.

105. Carrareto, C., Macor, A., Mirandola, A., Stoppato, A., Tonon, S.: Biodiesel as Alternative Fuel: Experimental Analysis and Energetic Evaluations. *Energy*, 29:241-246, 2004.

106. Silva, F.N., Prata, A.S., Teixeira, J.R.: Technical Feasibility Assessment of Oleic Sunflower Methyl Ester Utilization in Diesel Bus Engines. *Energy Convers Manage*, 44:2857-2878, 2003.

107. Rakopoulos, C.D., Hountalas, D.T., Zannis, T.C., Levendis, Y.A.: Operational and Environmental Evaluation of Diesel Engines Burning Oxygen-enriched Fuels: A Review. *SAE World Congress* Paper 2004-01-2924, 2004.

108. Assessment and Standards Division (Office of Transportation and Air Quality of the US Environmental Protection Agency): A Comprehensive Analysis of Biodiesel Impacts on Exhaust Emissions. EPA 420-P02-001, 2002.

109. Peterson, C.L., Reece, D.L.: Emissions testing with Blends of Esters of Rapeseed Oil Fuel With and Without a Catalytic Converter. *SAE World Congress* Paper 961114, 1996.

110. Lapuerta, M., Armas, O., Ballesteros, R., Fernandez, J.: Diesel Emissions from Biofuels Derived from Spanish Potential Vegetable Oils. *Fuel*, 84:773-780, 2005.

111. Ullman, T.L., Spreen, K.B., Mason, R.L.: Effects of Cetane Number, Cetane Improver, Aromatics, and Oxygenates on 1994 Heavy-duty Diesel Engine Emissions. *SAE World Congress* Paper 941020, 1994.

APPENDIX

Portions of several of my own publications have been used in composing this thesis. Rights for reproduction have been acquired. Please find the statements below. Details about my contribution to each publication has been outlined in the "CONTRIBUTION OF AUTHOR" section of this thesis. Permissions are attached in the following order:

1. Ramírez, A.I., Som, S., Aggarwal, S.K., Kastengren, A.L., El-Hannouny, E.M., Longman, D.E., Powell, C.F.: Quantitative X-Ray Measurements of High-Pressure Fuel Sprays from a Production Heavy Duty Diesel Injector. *Experiments in Fluids*, 47(1):119-134, 2009.
2. Ramírez, A.I., Som, S., LaRocco, L.A., Rutter, T.P., and Longman, D.E.: Investigating the use of Heavy Alcohols as a Fuel Blending Agent for Compression Ignition Engine Applications. *ASME 2012 Internal Combustion Engine Division Spring Technical Conference*, Paper Number ICES2012-81169, 2012.
3. Ramírez, A.I., Aggarwal, S.K., Som, S., Rutter, T.P., Longman, D.E.: Effects of Blending a Heavy Alcohol ($C_{20}H_{40}O$) with Diesel in a Heavy-Duty Compression-Ignition Engine. *Fuel*, 136:89-102, 2014.

APPENDIX (continued)

SPRINGER LICENSE
TERMS AND CONDITIONS

May 05, 2015

This is a License Agreement between Anita I Ramirez ("You") and Springer ("Springer") provided by Copyright Clearance Center ("CCC"). The license consists of your order details, the terms and conditions provided by Springer, and the payment terms and conditions.

All payments must be made in full to CCC. For payment instructions, please see information listed at the bottom of this form.

License Number	3622730235294
License date	May 05, 2015
Licensed content publisher	Springer
Licensed content publication	Experiments in Fluids
Licensed content title	Quantitative X-ray measurements of high-pressure fuel sprays from a production heavy duty diesel injector
Licensed content author	A. I. Ramírez
Licensed content date	Jan 1, 2009
Volume number	47
Issue number	1
Type of Use	Thesis/Dissertation
Portion	Full text
Number of copies	1
Author of this Springer article	Yes and you are the sole author of the new work
Order reference number	None
Title of your thesis / dissertation	Quantified Analysis of a Production Diesel Injector Using X-Ray Radiography and Engine Diagnostics
Expected completion date	May 2015
Estimated size(pages)	175
Total	0.00 USD
Terms and Conditions	

Introduction
The publisher for this copyrighted material is Springer Science + Business Media. By clicking "accept" in connection with completing this licensing transaction, you agree that the following terms and conditions apply to this transaction (along with the Billing and Payment terms and conditions established by Copyright Clearance Center, Inc. ("CCC"), at the time that you opened your Rightslink account and that are available at any time at http://myaccount.copyright.com).

Limited License
With reference to your request to reprint in your thesis material on which Springer Science

APPENDIX (continued)

and Business Media control the copyright, permission is granted, free of charge, for the use indicated in your enquiry.

Licenses are for one-time use only with a maximum distribution equal to the number that you identified in the licensing process.

This License includes use in an electronic form, provided its password protected or on the university's intranet or repository, including UMI (according to the definition at the Sherpa website: http://www.sherpa.ac.uk/romeo/). For any other electronic use, please contact Springer at (permissions.dordrecht@springer.com or permissions.heidelberg@springer.com).

The material can only be used for the purpose of defending your thesis limited to university-use only. If the thesis is going to be published, permission needs to be re-obtained (selecting "book/textbook" as the type of use).

Although Springer holds copyright to the material and is entitled to negotiate on rights, this license is only valid, subject to a courtesy information to the author (address is given with the article/chapter) and provided it concerns original material which does not carry references to other sources (if material in question appears with credit to another source, authorization from that source is required as well).

Permission free of charge on this occasion does not prejudice any rights we might have to charge for reproduction of our copyrighted material in the future.

Altering/Modifying Material: Not Permitted
You may not alter or modify the material in any manner. Abbreviations, additions, deletions and/or any other alterations shall be made only with prior written authorization of the author(s) and/or Springer Science + Business Media. (Please contact Springer at (permissions.dordrecht@springer.com or permissions.heidelberg@springer.com)

Reservation of Rights
Springer Science + Business Media reserves all rights not specifically granted in the combination of (i) the license details provided by you and accepted in the course of this licensing transaction, (ii) these terms and conditions and (iii) CCC's Billing and Payment terms and conditions.

Copyright Notice:Disclaimer
You must include the following copyright and permission notice in connection with any reproduction of the licensed material: "Springer and the original publisher /journal title, volume, year of publication, page, chapter/article title, name(s) of author(s), figure number(s), original copyright notice) is given to the publication in which the material was originally published, by adding; with kind permission from Springer Science and Business Media"

Warranties: None

Example 1: Springer Science + Business Media makes no representations or warranties with respect to the licensed material.

Example 2: Springer Science + Business Media makes no representations or warranties with respect to the licensed material and adopts on its own behalf the limitations and disclaimers

APPENDIX (continued)

established by CCC on its behalf in its Billing and Payment terms and conditions for this licensing transaction.

Indemnity
You hereby indemnify and agree to hold harmless Springer Science + Business Media and CCC, and their respective officers, directors, employees and agents, from and against any and all claims arising out of your use of the licensed material other than as specifically authorized pursuant to this license.

No Transfer of License
This license is personal to you and may not be sublicensed, assigned, or transferred by you to any other person without Springer Science + Business Media's written permission.

No Amendment Except in Writing
This license may not be amended except in a writing signed by both parties (or, in the case of Springer Science + Business Media, by CCC on Springer Science + Business Media's behalf).

Objection to Contrary Terms
Springer Science + Business Media hereby objects to any terms contained in any purchase order, acknowledgment, check endorsement or other writing prepared by you, which terms are inconsistent with these terms and conditions or CCC's Billing and Payment terms and conditions. These terms and conditions, together with CCC's Billing and Payment terms and conditions (which are incorporated herein), comprise the entire agreement between you and Springer Science + Business Media (and CCC) concerning this licensing transaction. In the event of any conflict between your obligations established by these terms and conditions and those established by CCC's Billing and Payment terms and conditions, these terms and conditions shall control.

Jurisdiction
All disputes that may arise in connection with this present License, or the breach thereof, shall be settled exclusively by arbitration, to be held in The Netherlands, in accordance with Dutch law, and to be conducted under the Rules of the 'Netherlands Arbitrage Instituut' (Netherlands Institute of Arbitration).***OR:***

All disputes that may arise in connection with this present License, or the breach thereof, shall be settled exclusively by arbitration, to be held in the Federal Republic of Germany, in accordance with German law.

Other terms and conditions:

v1.3

Questions? customercare@copyright.com or +1-855-239-3415 (toll free in the US) or +1-978-646-2777.

Gratis licenses (referencing $0 in the Total field) are free. Please retain this printable license for your reference. No payment is required.

APPENDIX (continued)

UIC

Anita Ramirez <aramir12@uic.edu>

Permission to reprint content from conference paper in Ph.D. thesis

Beth Darchi <DarchiB@asme.org> Fri, May 8, 2015 at 10:23 AM
To: Anita Ramirez <aramir12@uic.edu>

Dear Prof. Ramírez,

It is our pleasure to grant you permission to publish any part or all of the ASME paper "Investigating the Use of Heavy Alcohols as a Fuel Blending Agent for Compression Ignition Engine Applications," by Anita I. Ramírez, Sibendu Som, Lisa A. LaRocco, Timothy P. Rutter and Douglas E. Longman, Paper No. ICES2012-81169, as cited in your letter in a doctoral dissertation entitled Quantified Analysis of a Production Diesel Injector Using X-Ray Radiography and Engine Diagnostics to be published by University of Illinois at Chicago.

Permission is granted for the specific use as stated herein and does not permit further use of the materials without proper authorization. Proper attribution must be made to the author(s) of the materials. **Please note:** if any or all of the figures and/or Tables are of another source, permission should be granted from that outside source or include the reference of the original source. ASME does not grant permission for outside source material that may be referenced in the ASME works.

As is customary, we request that you ensure proper acknowledgment of the exact sources of this material, the authors, and ASME as original publisher. Acknowledgment must be retained on all pages printed and distributed.

Many thanks for your interest in ASME publications.

Sincerely,

ASME
SETTING THE STANDARD

Beth Darchi
Publishing Administrator
ASME
2 Park Avenue, 6th Floor
New York, NY 10016-5990
Tel 1.212.591.7700
darchib@asme.org

APPENDIX (continued)

ELSEVIER LICENSE
TERMS AND CONDITIONS

May 05, 2015

This is a License Agreement between Anita I Ramirez ("You") and Elsevier ("Elsevier") provided by Copyright Clearance Center ("CCC"). The license consists of your order details, the terms and conditions provided by Elsevier, and the payment terms and conditions.

All payments must be made in full to CCC. For payment instructions, please see information listed at the bottom of this form.

Supplier	Elsevier Limited The Boulevard,Langford Lane Kidlington,Oxford,OX5 1GB,UK
Registered Company Number	1982084
Customer name	Anita I Ramirez
Customer address	2125 N. Kilpatrick, Apt B CHICAGO, IL 60639
License number	3622721248501
License date	May 05, 2015
Licensed content publisher	Elsevier
Licensed content publication	Fuel
Licensed content title	Effects of blending a heavy alcohol (C20H40O with diesel in a heavy-duty compression-ignition engine
Licensed content author	None
Licensed content date	15 November 2014
Licensed content volume number	136
Licensed content issue number	n/a
Number of pages	14
Start Page	89
End Page	102
Type of Use	reuse in a thesis/dissertation
Portion	full article
Format	both print and electronic
Are you the author of this Elsevier article?	Yes
Will you be translating?	No
Title of your thesis/dissertation	Quantified Analysis of a Production Diesel Injector Using X-Ray Radiography and Engine Diagnostics

APPENDIX (continued)

Expected completion date	May 2015
Estimated size (number of pages)	175
Elsevier VAT number	GB 494 6272 12
Permissions price	0.00 USD
VAT/Local Sales Tax	0.00 USD / 0.00 GBP
Total	0.00 USD
Terms and Conditions	

INTRODUCTION

1. The publisher for this copyrighted material is Elsevier. By clicking "accept" in connection with completing this licensing transaction, you agree that the following terms and conditions apply to this transaction (along with the Billing and Payment terms and conditions established by Copyright Clearance Center, Inc. ("CCC"), at the time that you opened your Rightslink account and that are available at any time at http://myaccount.copyright.com).

GENERAL TERMS

2. Elsevier hereby grants you permission to reproduce the aforementioned material subject to the terms and conditions indicated.

3. Acknowledgement: If any part of the material to be used (for example, figures) has appeared in our publication with credit or acknowledgement to another source, permission must also be sought from that source. If such permission is not obtained then that material may not be included in your publication/copies. Suitable acknowledgement to the source must be made, either as a footnote or in a reference list at the end of your publication, as follows:

"Reprinted from Publication title, Vol /edition number, Author(s), Title of article / title of chapter, Pages No., Copyright (Year), with permission from Elsevier [OR APPLICABLE SOCIETY COPYRIGHT OWNER]." Also Lancet special credit - "Reprinted from The Lancet, Vol. number, Author(s), Title of article, Pages No., Copyright (Year), with permission from Elsevier."

4. Reproduction of this material is confined to the purpose and/or media for which permission is hereby given.

5. Altering/Modifying Material: Not Permitted. However figures and illustrations may be altered/adapted minimally to serve your work. Any other abbreviations, additions, deletions and/or any other alterations shall be made only with prior written authorization of Elsevier Ltd. (Please contact Elsevier at permissions@elsevier.com)

6. If the permission fee for the requested use of our material is waived in this instance, please be advised that your future requests for Elsevier materials may attract a fee.

7. Reservation of Rights: Publisher reserves all rights not specifically granted in the combination of (i) the license details provided by you and accepted in the course of this licensing transaction, (ii) these terms and conditions and (iii) CCC's Billing and Payment

APPENDIX (continued)

terms and conditions.

8. License Contingent Upon Payment: While you may exercise the rights licensed immediately upon issuance of the license at the end of the licensing process for the transaction, provided that you have disclosed complete and accurate details of your proposed use, no license is finally effective unless and until full payment is received from you (either by publisher or by CCC) as provided in CCC's Billing and Payment terms and conditions. If full payment is not received on a timely basis, then any license preliminarily granted shall be deemed automatically revoked and shall be void as if never granted. Further, in the event that you breach any of these terms and conditions or any of CCC's Billing and Payment terms and conditions, the license is automatically revoked and shall be void as if never granted. Use of materials as described in a revoked license, as well as any use of the materials beyond the scope of an unrevoked license, may constitute copyright infringement and publisher reserves the right to take any and all action to protect its copyright in the materials.

9. Warranties: Publisher makes no representations or warranties with respect to the licensed material.

10. Indemnity: You hereby indemnify and agree to hold harmless publisher and CCC, and their respective officers, directors, employees and agents, from and against any and all claims arising out of your use of the licensed material other than as specifically authorized pursuant to this license.

11. No Transfer of License: This license is personal to you and may not be sublicensed, assigned, or transferred by you to any other person without publisher's written permission.

12. No Amendment Except in Writing: This license may not be amended except in a writing signed by both parties (or, in the case of publisher, by CCC on publisher's behalf).

13. Objection to Contrary Terms: Publisher hereby objects to any terms contained in any purchase order, acknowledgment, check endorsement or other writing prepared by you, which terms are inconsistent with these terms and conditions or CCC's Billing and Payment terms and conditions. These terms and conditions, together with CCC's Billing and Payment terms and conditions (which are incorporated herein), comprise the entire agreement between you and publisher (and CCC) concerning this licensing transaction. In the event of any conflict between your obligations established by these terms and conditions and those established by CCC's Billing and Payment terms and conditions, these terms and conditions shall control.

14. Revocation: Elsevier or Copyright Clearance Center may deny the permissions described in this License at their sole discretion, for any reason or no reason, with a full refund payable to you. Notice of such denial will be made using the contact information provided by you. Failure to receive such notice will not alter or invalidate the denial. In no event will Elsevier or Copyright Clearance Center be responsible or liable for any costs, expenses or damage incurred by you as a result of a denial of your permission request, other than a refund of the amount(s) paid by you to Elsevier and/or Copyright Clearance Center for denied permissions.

LIMITED LICENSE

VITA

NAME: Anita I. Ramírez

EDUCATION: B.S., Mechanical Engineering, University of Illinois at Chicago (UIC), Chicago, Illinois, USA, 2004

Ph.D., Mechanical Engineering, University of Illinois at Chicago (UIC), Chicago, Illinois, USA, 2015

TEACHING EXPERIENCE: Developmental Education Department, City Colleges of Chicago – Richard J. Daley College, 2014-2015

Kaplan, Inc., 2013-2014

Minority Engineering Recruitment & Retention Program, University of Illinois at Chicago (UIC), 2001-2012, 2014

Upward Bound, Purdue University – Calumet, 2002-2004

Louis Stokes Alliance for Minority Participation, University of Illinois at Chicago (UIC), 2001-2002.

PROFESSIONAL EXPERIENCE: Mechanical Engineer Associate, Special Term Appointee. Argonne National Laboratory, 2012-2015

Research Student, Argonne National Laboratory, 2005-2012

Corporate Intern, Caterpillar, Inc., Summers 2002, 2003, 2004

HONORS AND AWARDS: University of Illinois at Chicago (UIC) Research Forum 2nd Place Poster Presentation in Physical Science and Engineering Category, 2010

Diversifying Higher Education Faculty in Illinois (DFI) Fellow, 2008-2011

Harold C. Simmons Best Student Paper Presentation in Basic or Applied Liquid Atomization and Sprays Research Applicable to Combustion Systems category, 2008

PUBLICATIONS: JOURNAL

Ramírez, A.I., Aggarwal, S.K., Som, S., Rutter, T.P., Longman, D.E.: Effects of Blending a Heavy Alcohol ($C_{20}H_{40}O$) with Diesel in a Heavy-Duty Compression-Ignition Engine. *Fuel*, 136:89-102, 2014.

VITA (continued)

Som, S., Ramírez, A.I., Longman, D.E., Aggarwal, S.K.: Effect of nozzle orifice geometry on spray, combustion, and emission characteristics under diesel engine conditions. *Fuel,* 90(3):1267-1276, 2011.

Som, S., Longman, D.E., Ramírez, A.I., Aggarwal, S.K: A Comparison of Injector Flow and Spray Characteristics of Biodiesel with Petrodiesel. *Fuel*, Vol 89(12):4014-4024, 2010.

Ramírez, A.I., Som, S., Aggarwal, S.K., Kastengren, A.L., El-Hannouny, E.M., Longman, D.E., Powell, C.F.: Quantitative x-ray measurements of high-pressure fuel sprays from a production heavy duty diesel injector. *Experiments in Fluids*, 47(1):119-134, 2009.

CONFERENCE PROCEEDINGS

Ramírez, A.I., Som, S., LaRocco, L.A., Rutter, T.P., Longman, D.E.: Investigating the use of heavy alcohols as a fuel blending agent for compression ignition engine applications. *ASME Internal Combustion Engine Division Spring Technical Conference*, Torino, Italy, ICES2012-81169, 2012.

Ramírez, A.I., Som, S., Rutter, T.P., Longman, D.E., Aggarwal, S.K..: Investigation of the effects of rate of injection on combustion phasing and emission characteristics: experimental and numerical study. *Spring Technical Meeting of the Central States Section of the Combustion Institute*, Dayton, Ohio, 2012.

Som, S., Longman, D.E., Ramírez, A.I., Aggarwal, S.K.: Comparing inner nozzle flow and spray characteristics of biodiesel with petrodiesel. *SAE World Congress* (Presentation Only), Detroit, Michigan, 2010.

Ramírez, A.I., Som, S., Aggarwal, S.K., Kastengren, A.L., El-Hannouny, E.M., Longman, D.E., Powell, C.F.: Characterizing Spray Behavior of Diesel injection Systems Using X-Ray Radiography. *SAE World Congress*, Detroit, Michigan, Paper 2009-01-0846, 2009.

Som, S., Ramírez, A.I., Aggarwal, S.K., Kastengren, A.L., El-Hannouny, E.M., Longman, D.E., Powell, C.F., Senecal, P.K.: Development and Validation of a Primary Breakup Model for Diesel Engine Applications. *SAE World Congress*, Detroit, Michigan, Paper 2009-01-0838, 2009.

Ramírez, A.I., Som, S., Aggarwal, S.K., Kastengren, A.L., El-Hannouny, E.M., Longman, D.E., Powell, C.F.: Quantitative Measurement of Diesel Fuel Spray Characteristics in the Near-Nozzle Region of a Heavy Duty Multi-Hole Injector. *ILASS Americas, 21st Annual Conference on Liquid Atomization and Spray Systems*, Orlando, FL, 2008.

BOOK CHAPTER

Som, S., Longman, D.E., Ramírez, A.I., Aggarwal, S.K.: Influence of nozzle orifice

VITA (continued)

geometry and fuel geometry and fuel properties on flow and cavitation characteristics of a diesel injector. Book chapter in *Fuel Injetion in Automotive Engineering.* INTECH Open Access Publisher, 2012. ISBN: 979-953-307-771-9.

POSTER PRESENTATIONS

Ramírez, A.I., Som, S., Longman, D.E.: Heavy alcohols as a fuel blending agent for compression ignition engine applications. *18th Directions in Energy-Efficiency Emissions Research (DEER) Conference*, Detroit, Michigan, 2012.

Ramírez, A.I., Som, S., Aggarwal, S.K., Kastengren, A.L., El-Hannouny, E.M., Longman, D.E., Powell, C.F.: Quantitative analysis of a heavy-duty diesel fuel injector. *UIC Student Research Forum*, Chicago, IL, 2010. (Won 2nd prize in Physical Science and Engineering Category)